Computational and experimental studies of exotic magnets and superconductors

Franziska Kirschner

Lincoln College

University of Oxford

A thesis submitted for the degree of

Doctor of Philosophy

Trinity 2018

Computational and experimental studies of exotic magnets and superconductors

Franziska Kirschner, Lincoln College, University of Oxford, Trinity 2018

Abstract of thesis submitted for the degree of Doctor of Philosophy

---

The advent of metalworking during the bronze age marked a transition in humankind's relationship with materials: instead of materials existing only as they were found in nature, one could now manipulate their physical properties to make them fit for purpose. With the discovery of quantum mechanics, the new opportunities to manipulate materials were manifold. The collective behaviour of electrons inside a solid is much more than the sum of its parts; as such, in some bulk materials, new quantum mechanical behaviour can emerge. We can use our knowledge of quantum mechanics to manipulate these *quantum materials*, and thus we find ourselves not in the bronze or the iron age, but in the quantum age.

This thesis is a series of four studies on a range of quantum materials.

I begin with emergent magnetic monopoles in spin ice. While there have been many bulk studies of monopoles, there is yet to be a microscopic measurement of small ensembles of these emergent quasiparticles. I use Monte Carlo methods to simulate the expected magnetic field fluctuations arising from small numbers of monopoles passing close to a probe near the surface of a spin ice, and show that the presence of monopole excitations produces unique features in the magnetic noise spectrum. I also propose several experiments which may be able to detect these features.

I then move onto $CoTi_2O_5$. Using μSR and neutron powder diffraction, as well as theoretical calculations, I find that this material undergoes a transition to an antiferromagnetic state, which is coupled to a spontaneous breaking of structural symmetry. This makes $CoTi_2O_5$ the lowest-known-symmetry crystal to undergo the spin Jahn-Teller effect. I then present a possible magnetostructural coupling regime.

The remaining studies examine the importance of topology in the successful understanding of quantum material systems. I use μSR to investigate both the $A Ca_2Fe_4As_4F_2$ (A = K, Rb, or Cs) and $Lu_xZr_{1-x}B_{12}$ families of superconductors. It is possible to alter the topological character of the superconducting gap in these families, either by manipulating the chemical spacer layers in the crystal structure of $A Ca_2Fe_4As_4F_2$ or by changing x in $Lu_xZr_{1-x}B_{12}$. Along with the gap topologies, both the penetration depths and critical temperatures of these compounds appear to be sensitive to these chemical manipulations. I investigate how these topological crossovers are linked to the other superconducting properties of these materials, and discuss the consequences for our wider understanding of superconductivity.

"It is a mistake to think you can solve any major problems with just potatoes."

– Douglas Adams

Acknowledgements

More is different. The whole is greater than the sum of its parts. This is a thesis on quantum materials; if you've come this far, you know the drill. I entered this degree as a bleary-eyed, overgrown teenager: well-versed in street slang and Matlab. I leave (hopefully) as Dr Kirschner: aware of English grammar, and a Python convert. I can barely tie my own shoelaces. So I could never have done this DPhil on my own.

First and foremost, I thank my supervisor Stephen Blundell for being a mentor and a friend, and for keeping me motivated, entertained, and sane throughout my DPhil. During the last three years I learned great lessons in science, literacy, diplomacy, politics, and cooking from Steve, making it the most intellectually rich and stimulating period of my life so far. Steve has provided masses of proofreading, problem solving, and coding to improve this thesis enormously, and I am greatly indebted to him.

I also thank the rest of my research group. I thank Franz for experimental help and DFT calculations, as well as many interesting beamtime conversations. I thank Craig for teaching me how to use the SQUID and for being a great colleague overall. I thank Matt for help with the VSM and for many fruitful discussions on superconductors, but not for jumping out at me and reducing my lifespan by several years.

I give very many thanks to the beamline scientists during my DPhil for their valuable expertise and for keeping the experiments under control, in particular Peter Baker, Francis Pratt, Robert Scheuermann, and Tatsuo Goko. I thank Prabhakaran, Simon Clarke, Nikolay Sluchanko, and Guang-Han Cao for the high quality samples. I thank Felix Flicker, Norm Yao, and Amir Yacoby for their theoretical and practical expertise (as well as access to the Harvard supercomputer). I thank Adroja and Michael Smidman for a very interesting and fruitful experimental collaboration. I thank Roger Johnson for his group theoretical wizardry.

I thank Lincoln College for funding my DPhil, as well as two conferences and numerous dinners.

I thank the members of Quantum Materials for the teatime entertainment. I thank Sam for the cake (and for agreeing to watch the football in Eurobar). I thank Dave and Rowan for not burning the house down. I thank Kathryn and Ben for their active engagement with feminism. I thank Tom for the cultural experiences. I thank Lothar for the postcards. I thank The Blokes for their unwavering support. I thank my family for forming me into the person I am today. I thank various dogs for their wise counsel and fluffy, fluffy cuddles. Finally, I thank my sanity (and my laptop) for just about holding out 'til the end.

Contents

List of publications

Filled circles indicate the work which has contributed to this thesis.

- *Spin Jahn-Teller antiferromagnetism in $CoTi_2O_5$.*
  F. K. K. Kirschner, R. D. Johnson, F. Lang, D. D. Khalyavin, P. Manuel, T. Lancaster, D. Prabhakaran, and S. J. Blundell, arXiv 1808.01387 (2018).
- ○ *Evidence for $J_{\text{eff}} = 0$ ground state and defect-induced spin glass behaviour in the pyrochlore osmate $Y_2Os_2O_7$.*
  N. R. Davies, C. V. Topping, H. Jacobsen, A. J. Princep, F. K. K. Kirschner, M. C. Rahn, M. Bristow, J. G. Vale, I. da Silva, P. J. Baker, Ch. J. Sahle, Y.-F. Guo, D.-Y. Yan, Y.-G. Shi, S. J. Blundell, D. F. McMorrow, and A. T. Boothroyd, arXiv 1808.01530 (2018).
- *Observation of a crossover from nodal to gapped superconductivity in $Lu_xZr_{1-x}B_{12}$.*
  F. K. K. Kirschner, N. E. Sluchanko, V. B. Filipov, F. L. Pratt, C. Baines, N. Y. Shitsevalova, and S. J. Blundell, Physical Review B **98**, 094505 (2018).
- *Multigap superconductivity in $RbCa_2Fe_4As_4F_2$ investigated using μSR measurements.*
  D. T. Adroja, F. K. K. Kirschner, F. Lang, M. Smidman, A. D. Hillier, Z. C. Wang, G. H. Cao, G. B. G. Stenning, and S. J. Blundell, arXiv 1802.07334 [Journal of the Physical Society of Japan in press] (2018).
- *Nodal multigap superconductivity in $KCa_2Fe_4As_4F_2$.*
  M. Smidman, F. K. K. Kirschner, D. T. Adroja, A. D. Hillier, F. Lang, Z. C. Wang, G. H. Cao, and S. J. Blundell, Physical Review B **97**, 060509(R) (2018).
- *Two-gap superconductivity with line nodes in $CsCa_2Fe_4As_4F_2$.*
  F. K. K. Kirschner, D. T. Adroja, Z. C. Wang, F. Lang, M. Smidman, P. J. Baker, G. H. Cao, and S. J. Blundell, Physical Review B **97**, 060506(R) (2018).
- ○ *Static and fluctuating magnetic moments in the ferroelectric metal $LiOsO_3$.*
  F. K. K. Kirschner, F. Lang, F. L. Pratt, T. Lancaster, Y. Shi, Y. Guo, A. T. Boothroyd, and S. J. Blundell, Proceedings of the 14th International Conference on Muon Spin Rotation, Relaxation and Resonance (μSR2017), JPS Conference Proceedings **21**, 011013 (2018).
- ○ *$LaSr_3NiRuO_4H_4$: a 4d transition-metal oxide-hydride containing metal hydride sheets.*
  L. Jin, M. Lane, D. Zheng, F. K. K. Kirschner, F. Lang, P. Manuel, S. J. Blundell, J. E. McGrady, M. A. Hayward, Angewandte Chemie **57**, 5025 (2018).

- *Proposal for the detection of magnetic monopoles in spin ice via nanoscale magnetometry.*
  F. K. K. Kirschner, F. Flicker, A. Yacoby, N. Y. Yao, and S. J. Blundell, Physical Review B **97**, 140402(R) (2017).
- *Coexistence of magnetism and superconductivity in separate layers of iron-based superconductor* $Li_{1-x}Fe_x(OH)Fe_{1-y}Se$.
  C. V. Topping, F. K. K. Kirschner, S. J. Blundell, P. J. Baker, D. N. Woodruff, F. Schild, H. Sun, and S. J. Clarke, Physical Review B **95**, 134419 (2017).
- *Robustness of superconductivity to competing magnetic phases in tetragonal FeS.*
  F. K. K. Kirschner, F. Lang, C. V. Topping, P. J. Baker, F. L. Pratt, S. E. Wright, D. N. Woodruff, S. J. Clarke, and S. J. Blundell, Physical Review B **94**, 134509 (2016).

Abbreviations and constants

Several common abbreviations and constants are used in this thesis and are listed here.

AFM	Atomic force microscopy
AIAO	All-in-all-out model
ARPES	Angle-resolved photoemission spectroscopy
BCS	Bardeen-Cooper-Schrieffer
CW	Continuous wave
DFCs	Dipolar field calculations
DFT	Density functional theory
DSIM	Dipolar spin ice model
DTO	$Dy_2Ti_2O_7$
FC	Field-cooled
FLL	Flux line lattice
GL	Ginzburg-Landau
HTO	$Ho_2Ti_2O_7$
LF	Longitudinal field
MC	Monte Carlo
μSR	Muon spin rotation/relaxation/resonance
NMR	Nuclear magnetic resonance
NNSIM	Nearest neighbour spin ice model
NPD	Neutron powder diffraction
NV	Nitrogen–vacancy
SC	Superconductor
SQUID	Superconducting quantum interference device
TF	Transverse field
TRSB	Time reversal symmetry breaking
ZF	Zero field
ZFC	Zero-field-cooled

$\mu_B = 9.274 \times 10^{-24}\,JT^{-1}$	Bohr magneton
$k_B = 1.381 \times 10^{-23}\,kgm^2s^{-2}K^{-1}$	Boltzmann constant
$e = 1.602 \times 10^{-19}\,C$	Electron charge
$m_e = 9.109 \times 10^{-31}\,kg$	Electron mass
$\phi_0 = 2.068 \times 10^{-15}\,Wb$	Flux quantum
$\gamma_\mu = 2\pi \times 135.5\,MHzT^{-1}$	Gyromagnetic ratio of the muon
$m_p = 1.673 \times 10^{-27}\,kg$	Proton mass
$\hbar = 1.055 \times 10^{-34}\,Js$	Reduced Planck's constant
$c = 2.997 \times 10^{8}\,ms^{-1}$	Speed of light in vacuum
$\mu_0 = 4\pi \times 10^{-7}\,Hm^{-1}$	Vacuum permeability

List of Figures

1

Introduction

Give a physicist an electron, and she'll study for a day; teach a physicist about 10^{23} electrons, and she'll have enough to study for a lifetime (and several lifetimes afterwards, too). While the fundamental physics of individual electrons is well-known, what happens when they are thrust together with protons and neutrons to form atoms, and then solid matter, is rather more mysterious. In the words of P. W. Anderson: *more is different* [1].

A large number of electrons at close quarters with one another leads to cooperative and correlated behaviour, and as a result novel quantum mechanical phenomena emerge from the bulk. Materials exhibiting such behaviours are quantum materials, and include magnets, superconductors, and even biological systems. We are living in a quantum material world.[1]

This thesis is a series of experimental and theoretical studies on a selection of quantum materials.

[1] And I am a quantum material girl.

The experimental and theoretical techniques I use are outlined in Chapters 2 and 3 respectively. Chapter 2 contains an introduction to μSR and SQUID magnetometry. Chapter 3 introduces two techniques specific to the interpretation of μSR data: density functional theory and dipole field calculations, as well as the Monte Carlo method applied to modelling spin systems.

Moving to the theme of emergence, I present a theoretical (albeit experimentally-motivated) study of emergent magnetic monopole behaviour in the spin ice materials in Chapter 4. I begin with an exploration of the current experimental possibilities in this field, and then propose several new experiments to detect the dynamical magnetic fields arising from single and small ensembles of magnetic monopoles.

I then move onto a different correlated system: the spin Jahn-Teller-mediated antiferromagnet $CoTi_2O_5$ in Chapter 5. This chapter is an in-depth, multi-experiment study of $CoTi_2O_5$, in which I explore its antiferromagnetic order, and the magnetostructural coupling that is required in order to relieve the frustrated magnetism.

Electrons are fermions. But when is a fermion not a fermion? When there are two of them coupled in a Cooper pair. Chapter 6 introduces superconductors, and the experimentally measurable properties associated with their Cooper pairs.

Accompanying emergence, topology is another key property of quantum materials. By manipulating the topology and symmetry of the microscopic electronic structure of a material, it is possible to significantly alter its properties at the macroscopic scale. Chapter 7 contains a study of the $A Ca_2Fe_4As_4F_2$ family of superconductors, which, despite being crystallographically similar to other iron-based superconductors, have a vastly different superconducting gap topology. I study their physical properties using μSR and discuss their relevance in the search for an underlying theory of iron-based superconductivity.

Another family of superconductors in which the gap topology is chemically alterable is the $Lu_xZr_{1-x}B_{12}$ compounds. I present a μSR study of this family in Chapter

8 and evaluate the relationship between the gap and the x-dependence of the other superconducting parameters.

Finally, I bring together the main conclusions of the individual chapters and discuss them in the broader context of quantum materials in Chapter 9.

2

Experimental techniques

A few notable left-handers include Barack Obama, Marie Curie, Neil Armstrong, the author, and the neutrino. Arguably the most important member of this list is the neutrino (in the context of this thesis, anyway); if it were ambidextrous, the μSR technique would simply not exist.

Following the success of Wu *et al.*'s experiment using ^{60}C nuclei to test parity violation [2], Garwin *et al.* attempted a similar experiment, this time using the decay of the positive pion [3]. The pion decays to a positive muon, which then decays to a positron and two neutrinos. If parity were violated (resulting in neutrinos of only a single chirality), the spatial distribution of the positron would be asymmetric with respect to the muon's initial polarisation. It was; μSR was born.

The bulk of the work in this thesis is based on experiments using the μSR technique to investigate the magnetic and superconducting properties of materials. The technique utilises positively-charged antimuons (hereafter simply called muons) to de-

tect the internal magnetic fields of a sample. In short: muons enter the sample, and settle in an interstitial site in the unit cell. The muons' spins precess in the local magnetic field, and then the muons decay and produce positrons. The positrons can be detected and thus the muon precession, and therefore the internal field distribution, can be inferred.

This section will start with an introduction to the μSR technique and its applications in condensed matter systems. A further experimental probe, SQUID magnetometry, will then be introduced in the second section, and a discussion of its use in complementing the μSR technique follows.

2.1 The μSR technique

Muon spin rotation/relaxation/resonance (μSR) is a technique in condensed matter physics which measures the time evolution of the spin of the muon in a sample. The wide scope of applications of this technique is manifest in the ambiguity of the 'R' in μSR. This thesis focuses primarily on the rotation and relaxation applications. A comprehensive introduction to all three 'R's is given in Ref. 4.

Positive muons are most often used in condensed matter physics experiments as they preferentially implant close to areas of high electron density or near electronegative atoms (and, unlike negative muons, cannot be captured by nuclei). Muons can be thought of as heavy electrons, or in the case of positive muons, light protons. The properties of these particles are summarised in Table 2.1.

2.1.1 Muon production, propagation, and decay

In muon sources, high-energy protons p (with energies between 600 and 800 MeV) are fired into a graphite target to produce pions π^+:

$$p + p \rightarrow \pi^+ + p + n, \tag{2.1}$$

	e^-	μ^+	p
Charge	$-e$	$+e$	$+e$
Mass	m_e	$207m_e$	$1863m_e$
	$0.0054m_p$	$0.11m_p$	m_p
Spin	1/2	1/2	1/2
Gyromagnetic ratio $\gamma/2\pi$ (MHzT^{-1})	28025	135.5	42.58
Lifetime	$> 4.6 \times 10^{26}$ yr	2.197μs	$> 2.1 \times 10^{29}$ yr

Table 2.1: Some properties of the electron, positive muon, and proton.

which then decay to muons μ^+ and muon neutrinos ν_μ:

$$\pi^+ \rightarrow \mu^+ + \nu_\mu. \tag{2.2}$$

By only using muons produced by pions stopping in the target ('surface muons'), the muons are 100% spin-polarised as the neutrino's negative helicity and pion's zero spin constrain the muon's spin to point antiparallel to its momentum. It is also possible to use muons produced by pions in-flight ('decay muons'), which have a higher momentum than those produced from pions at rest and may be useful in experiments where the muon must, for example, penetrate a pressure chamber. Only surface muons will be discussed in this thesis. As the pion decay involves only two products, the muon's energy and momentum in the pion rest frame can be exactly calculated to be 4.1 MeV and 29.8 MeV/c respectively.

Once the surface muons have been produced, it is paramount that any other contaminant particles in the muon beam are filtered out. The muon beam is focussed using quadrupolar magnets and its direction altered using dipolar magnets, which both filter the beam to some extent (as particles with different momenta p and charge q have their paths bent to differing degrees in a magnetic field B; the bending radius is given by $r = p/qB$). Further filtering is achieved with a Wien filter, which consists of a perpendicular electric E_W and magnetic field B_W, and selects a set of particles with a specific matched velocity $v = E_\mathrm{W}/B_\mathrm{W}$ (this can be derived by examining the

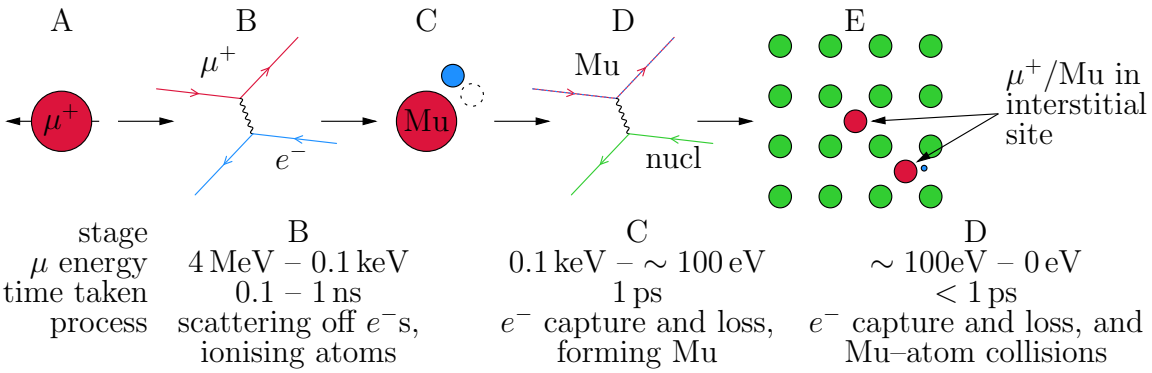

Figure 2.1: A schematic showing the stopping processes of a muon entering a sample. *A:* A spin-polarised muon; *B:* muon–electron scattering; *C:* muonium (Mu) formation; *D:* Mu–nucleus scattering; *E:* diamagnetic muon or paramagnetic Mu at rest in an interstitial site. The bottom panel shows the processes and relevant time and energy scales for stages B, C, and D.

Lorentz force on charged particles in the filter). At this stage, a Wien filter may also be used to rotate the muons' spins; this point will be further discussed in Section 2.1.3.

Once inside the sample, muons lose their energy through a series of Coulombic events, thus leaving the spin polarisation unchanged. A schematic of the stopping processes and their timescales is given in Fig. 2.1. The stopping depth of a muon is dependent on the density of the sample, and one should aim for a density of $\approx 110\,\mathrm{mg\,cm^{-2}}$ [for small quantities of sample, placing a thin sheet of silver degrader in front of the sample slows down the muons slightly such that they come to rest in the sample itself]. Muons have a lifetime of approximately 2.2 μs and decay via

$$\mu^+ \rightarrow e^+ + \nu_e + \bar{\nu}_\mu. \tag{2.3}$$

From this decay, the positron's energy is measured. As this is a three-body decay, the positron's energy and momentum are not defined, and the number of positrons emitted at a given angle θ follows the distribution

$$N = N_0\,(1 + a\cos\theta)\,; \tag{2.4}$$

this function is visualised in Figure 2.2. The factor a is dependent on the positron energy, taking the value 1 for the maximum possible energy (52.8 MeV/c) and averaging

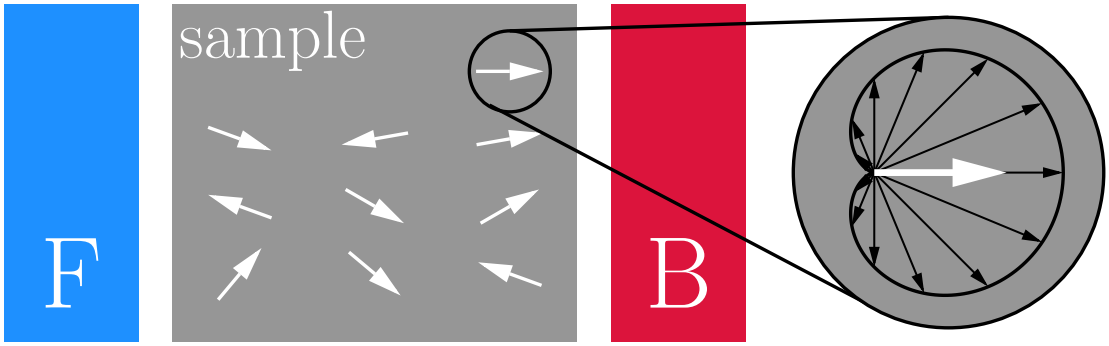

Figure 2.2: A schematic of a μSR experiment, with forward (F) and backward (B) detectors on either side of the sample. Note that the spins of the different implanted muons (white arrows) point in different directions due to their different interactions with their different local environments. The inset show the probability distribution of the e^+ emission direction from a μ^+ with its spin along the white arrow, calculated from Equation 2.4. The length of the arrow is proportional to the probability that the e^+ is emitted along its direction.

at 1/3. The positron may be detected either using a scintillator and photomultiplier tube, or more recently, using avalanche photodiodes.

The precession of the muons' spins in the local magnetic fields can be measured by using a large sample ($\sim 10^7$) of incoming muons, and placing an array of detectors around the sample space.

2.1.2 Rotation, relaxation, and the internal field distribution

If the muon stops in a site with a magnetic field of magnitude B, it will Larmor precess with frequency $\omega = \gamma_\mu B$, where $\gamma_\mu = 2\pi \times 135.5\,\mathrm{MHzT}^{-1}$ is the gyromagnetic ratio of the muon. Muons that decay at different stages in their precession will preferentially emit positrons in different directions, which can be detected in either the backward or forward detectors which lie behind and in front of the sample respectively; this geometry is visualised in Figure 2.2. The number of positrons detected in the forward $[N_\mathrm{F}(t)]$ and backward $[N_\mathrm{B}(t)]$ detectors is shown in the central column of Figure 2.3, and the normalised difference of these two counts gives the asymmetry function, which

describes the time evolution of the muon's polarisation:

$$A(t) = \frac{N_{\mathrm{B}}(t) - \alpha N_{\mathrm{F}}(t)}{N_{\mathrm{B}}(t) + \alpha N_{\mathrm{F}}(t)}, \tag{2.5}$$

where α is an experimentally-determined calibration constant which takes into account asymmetries in detector efficiency. The spins of muons in a constant field precess coherently, and the asymmetry function for a set of muons experiencing such a field is given in the right column of Figure 2.3 and in Figure 2.4(a). From this it is also clear that the asymmetry is proportional to the polarisation of the muons.

However, if the sample contains a range of fields, muons landing in different parts of the sample will Larmor precess with slightly different frequencies, meaning their precession dephases over time. This manifests itself in the asymmetry spectrum through a decay (relaxation) in the asymmetry amplitude, which is related to the Fourier transform of the field distribution. If the fields sampled by the muons are randomly distributed or follow a very broad distribution, it is possible that no oscillations are observed at all and only the relaxation is measured. An example of an inhomogeneous field distribution in a superconductor and its related muon asymmetry is shown in Fig. 2.4(b).

Aside from an externally applied field, there are a variety of sources of field that a muon at position $\mathbf{r}_\mu$ may experience. Common contributions include the dipolar fields from localised moments and demagnetising fields; their determination and calculation will be discussed in Sec. 3.1. There exist a range of other fields and magnetic couplings a muon may experience, for example a hyperfine contact coupling due to a polarised electron density at the muon site, however for the systems investigated in this thesis these interactions are negligible and will not be discussed.

2.1.3 Detector geometry

Experiments can either be carried out in an external magnetic field applied along (longitudinal-field μSR, LF-μSR) or perpendicular to (transverse-field μSR, TF-μSR)

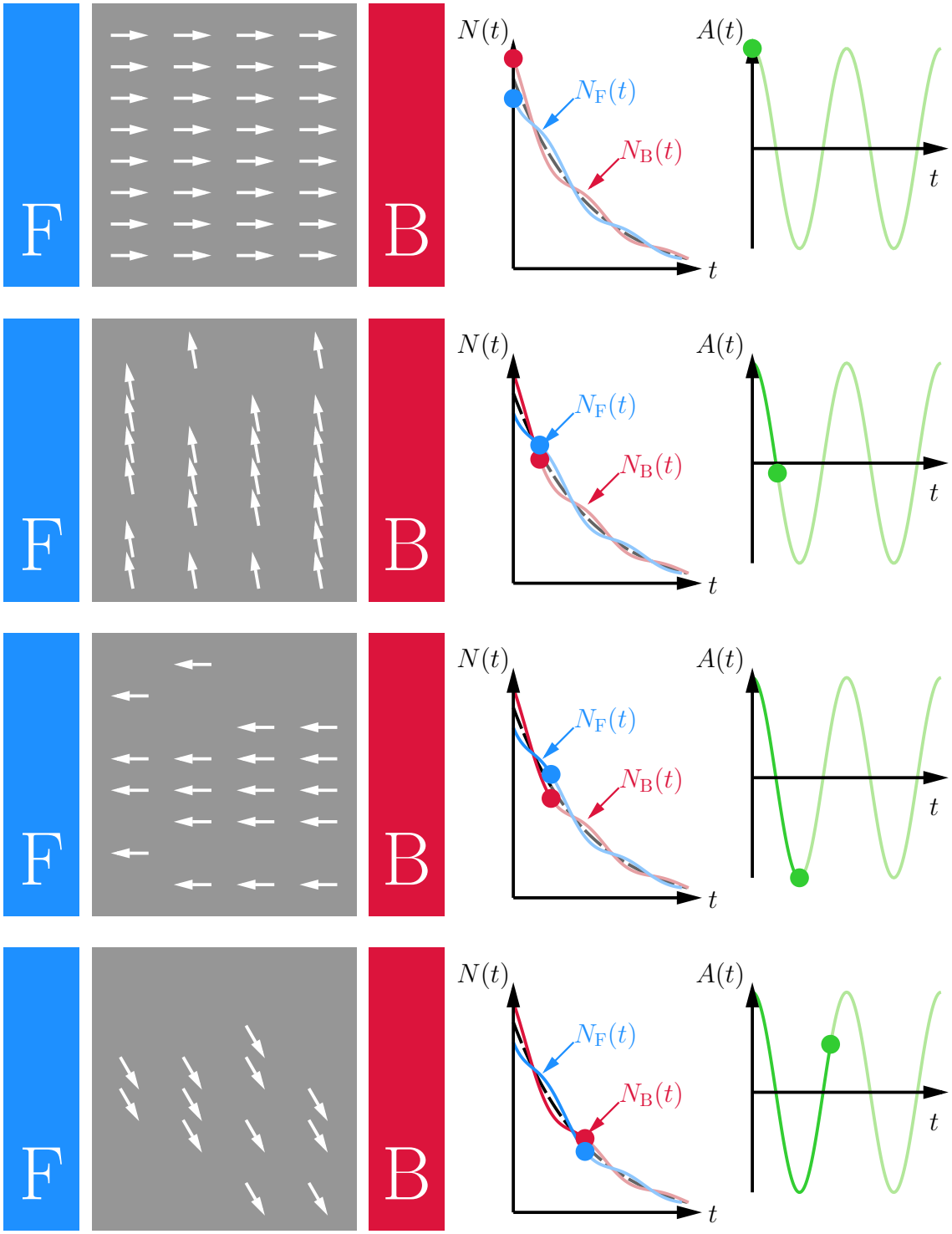

Figure 2.3: *Left:* Snapshots of muons in a sample precessing in a uniform magnetic field. *Centre:* e^+ counts detected in the forward $[N_F(t)]$ and backward $[N_B(t)]$ detectors as a function of time, where the dashed line shows the exponential decay of the signal. *Right:* normalised asymmetry, calculated using Equation 2.5.

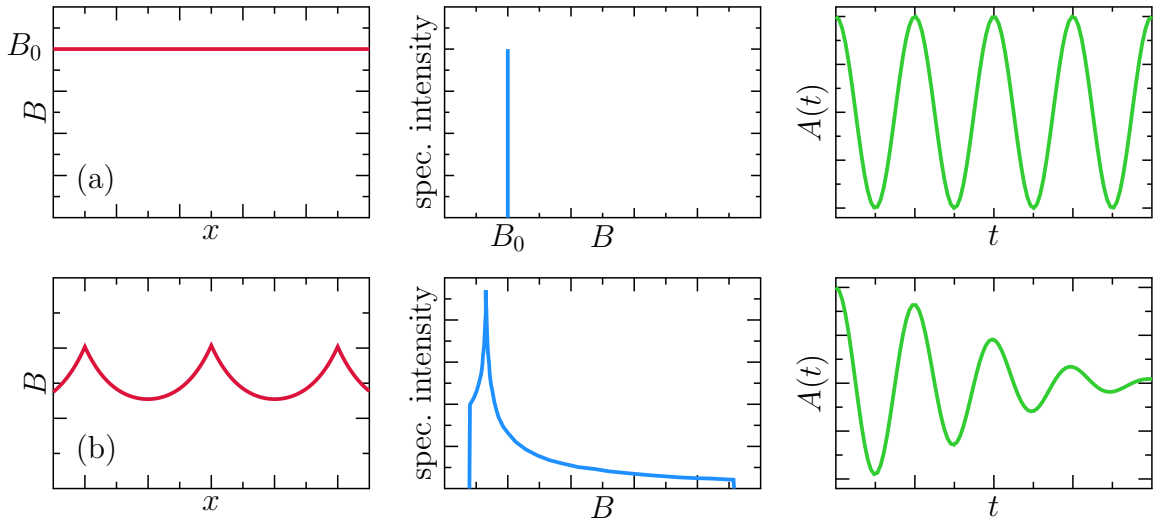

Figure 2.4: The spatial field distribution (*left*), field spectrum (*centre*) and corresponding muon asymmetry function $A(t)$ (*right*) for (a) a uniform magnetic field, and (b) a superconducting vortex lattice.

the initial muon spin polarisation, or in zero field (zero-field μSR, ZF-μSR), although in ZF-μSR, a small field is often applied to cancel out the Earth's magnetic field.

As the field in LF-μSR is applied along the initial direction of the muon's spin, the muon precesses only in the internal magnetic fields of the sample. LF-μSR is particularly useful when determining the size of the internal field inside a sample; when the applied field becomes of comparable magnitude to the internal field, the muons' spins will no longer precess.

The internal field distribution inside a magnetic sample can be measured with ZF-μSR as muons will only precess in this internal field. By using a combination of LF- and ZF-μSR, it is possible to infer the magnitude and width of a sample's internal field, and to deduce whether it exhibits a dynamic character or not: muons experiencing a static or slowly fluctuating field B_{internal} are particularly susceptible to becoming decoupled from such a field by a longitudinal field $B_{\text{LF}} > 10B_{\text{internal}}$, whereas muons experiencing fast dynamics are not [5].

In TF-μSR, the muon's spin precesses in both the externally applied field and internal magnetic fields of a sample. This geometry is particularly useful in the study

of type II superconductors, where a flux line lattice is induced along the direction of the field [6, 7].

The parameter α in Eq. 2.5 is measured using a weak transverse field of 2–5 mT, and experiments in the longitudinal geometry have small transverse Helmholtz coils to allow this measurement to be taken.

There are several options if one wishes to carry out experiments in both the longitudinal and transverse geometry (ZF-μSR experiments can be done in either). Some μSR instruments are limited to a single geometry, dictated by the angle between the incoming muons' spins and the externally applied magnetic field, however some are designed such that the orientation can be changed by physically moving the magnet or by rotating the muons' spins using a Wien filter.

2.1.4 Relaxation functions

Depending on the detector geometry and the nature of the internal field of the sample, muon asymmetry spectra can take on a wide variety of different functional forms. A discussion of some of the general forms is presented in Sec. 3.1 and further information on asymmetry functions can be found in Refs. 4, 5, and 8.

2.1.5 Muon sources

There are two main types of muon source: continuous wave (CW) and pulsed. In a CW beam, muons arrive at the sample one at a time, and upon entry a clock is started. Once the positron is detected, the clock is stopped and another muon may enter the sample. In pulsed sources, large numbers of muons arrive in a pulse and positrons are detected relative to the pulse arrival time. CW sources have very accurate timing measurements but low statistics (as muons can only enter one at a time, as opposed to millions at a time in pulsed sources), and so are good for measuring high precession frequencies. Pulsed sources have very high statistics, but the finite pulse width limits the timing accuracy, which makes them better suited to

experiments with lower precession frequencies. In general, μSR has a time resolution of $\sim 1\,\text{ns}$–$10\,\text{ms}$, corresponding to a static local magnetic field of $\sim 1\,\text{T}$–$0.1\,\mu\text{T}$.

The μSR experiments in this thesis were carried out using the pulsed muon source at the ISIS pulsed muon facility, Rutherford Appleton Laboratory, UK [9] and the CW beam at the Paul Scherrer Institute, Switzerland.

2.2 SQUID magnetometry

Bulk magnetometry measurements in this thesis were performed using a superconducting quantum interference device (SQUID) magnetometer. A SQUID magnetometer is a highly sensitive magnetic probe, with a sensitivity of up to $5 \times 10^{-8}\,\text{emu}$. The instrument can be used in both a dc mode (for probing a static magnetisation) and an ac mode (for examining spin dynamics). This thesis will only include dc measurements.

A SQUID magnetometer consists of a second-order gradiometer (a set of conducting pick-up coils) connected to a superconducting loop consisting of two parallel Josephson junctions. A sample is placed in a non-magnetic sample holder, and then the sample holder is inserted inside the pick-up coils. As the sample moves in the gradiometer, Faraday's law dictates that a current must be induced in the coils. The SQUID then converts the change in magnetic flux measured by the coils to a dipole response voltage. The SQUID voltage is measured for several sample positions along the length of the gradiometer, and is then fitted with the expected signal from a point-source magnetic dipole. Thus, the magnetic moment of the sample can be extracted. A schematic of a SQUID magnetometer is shown in Fig. 2.5.

There are two main dc configurations in a SQUID: zero field-cooled (ZFC) and field-cooled (FC). ZFC measurements involve cooling the sample down, then applying an external magnetic field H. FC measurements apply the field before cooling occurs. These two configurations allow for a range of magnetic phenomena to be observed,

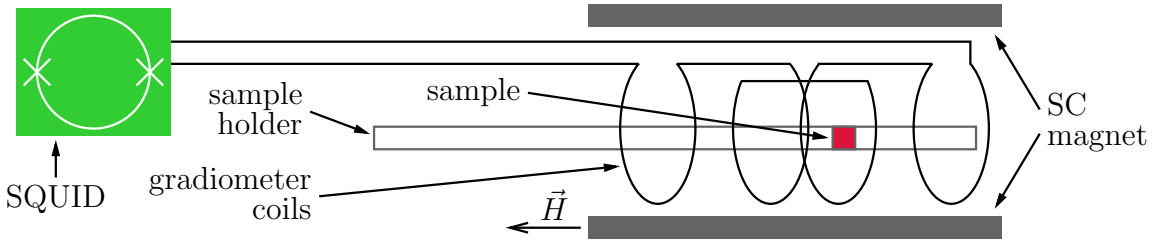

Figure 2.5: A schematic of a SQUID magnetometer. The sample is moved through the gradiometer coils, which induces a current. The current flows to the SQUID, which in turn produces a voltage response. The magnetisation is then found by fitting the voltage response.

including ordered magnetism in Chapter 5, and superconductivity in Chapters 7 and 8.

Both the magnetisation M of the sample and the magnetic susceptibility $\chi = \lim_{H\to 0} M/H$ can be measured using a SQUID, and it is particularly useful for identifying different magnetic regimes and the locations of the phase transitions between them. Often a SQUID is used to characterise the magnetic phases of a sample in preparation for a more detailed μSR experiment. What must be kept in mind, however, is that the SQUID is a bulk probe, and therefore local phenomena that can be detected using μSR (for example short-range ordered magnetism [10, 11]) may not be detectable using a SQUID.

2.3 Conclusion

This chapter provides an introduction to the two main experimental techniques used in this thesis: μSR and dc SQUID magnetometry. The combination of these methods, along with other bulk and local probes (for example neutron powder diffraction, x-ray diffraction, and nitrogen-vacancy centre magnetometry), provides a powerful tool kit to investigate the properties of a large breadth of magnetic and superconducting materials.

3

Theoretical techniques

The leap from experimental data to an understanding of nature most often occurs via theory. While textbooks are populated with successful symbioses of the physical and the mathematical, a rather more realistic situation is proposed by Jan L. A. van de Snepscheut (and later paraphrased by Yogi Berra): "the difference between theory and practice is larger in practice than the difference between theory and practice in theory". To complement the experimental probes introduced in the previous chapter, I use theoretical and computational methods throughout this thesis. This chapter serves as an introduction to those methods. The first half of this chapter deals with the tools necessary to model magnetic systems in the context of μSR: density functional theory (DFT) and dipole field calculations. The latter half will introduce the Monte Carlo simulation and its application to modelling spin dynamics.

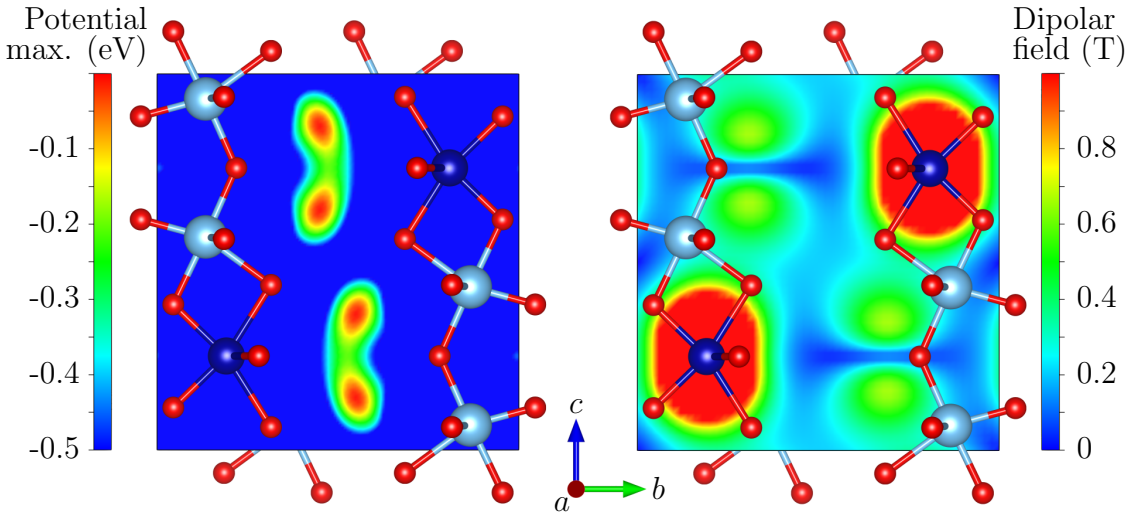

Figure 3.1: *Left:* The electrostatic potential relative to the maximum in the (100) plane for $CoTi_2O_5$. *Right:* The dipolar magnetic field in the (100) plane for $CoTi_2O_5$.

3.1 DFT+μ and dipolar field calculations

μSR experiments, as detailed in the previous chapter, allow one to probe local and bulk magnetism using the precession and decay of positive muons. The experimental data provide us with an internal magnetic field distribution at the muon site, and theoretical methods must be used to address the following questions:

1. Where is the muon?
2. Which magnetic configuration is causing the field distribution at that site?

Question 1 is addressed using a technique called DFT: a method used to find approximate solutions to the many-body problem in solids. The precise details of DFT are outside of the scope of this thesis, and more information can be found in Refs. 12, 13, and 14.

The basic premise of DFT involves populating a unit cell with atoms, each with an associated electrostatic pseudopotential (an approximation to the true electrostatic potential of an atom which simplifies the motion of non-valence electrons and the nucleus), and solving the many-body Schrödinger equation via a series of approximations. While useful for determining expected atomic positions within a unit cell,

DFT can also be used to identify potential sites at which muons stop in the sample. This approach is, aptly, called DFT+μ. A diamagnetic muon (the only variety of muon discussed in this thesis) can be modelled as a hydrogen pseudopotential.

A first approximation of the expected muon position can be found by solely examining the magnitude of the electrostatic pseudopotential across the unit cell. The maxima of such a potential map have been found to be a reliable approximation to the muon position [12, 13, 14, 15, 16, 17] [note that the maxima of the potential map are unaffected by the magnetism of the atoms in the unit cell; a comparison between the electrostatic potential and magnetic field in the unit cell of $CoTi_2O_5$ shown in Fig. 3.1]. A more detailed study can also be done, in which atom positions are allowed to relax in the presence of a muon. The latter method allows for distortions in the lattice due to the muon's presence to be quantified, and any distortion-induced magnetism to be accounted for [15].

Once the atomic and muon positions have been determined, we can move to Question 2. By modelling a series of hypothetical spin configurations in a given material, it is possible to calculate the associated μSR asymmetry spectra using dipolar field calculations (DFCs). DFCs involve placing a spin i with moment $\mathbf{m}_i$ at the position $\mathbf{r}_i$ of each magnetic atom or ion, and calculating the resulting dipolar field at the muon site $\mathbf{r}_\mu$

$$\mathbf{B}_{\text{dip}} = \sum_i \frac{\mu_0}{4\pi|\mathbf{R}_i|^3}\left[\frac{3\mathbf{R}_i\,(\mathbf{R}_i\cdot\mathbf{m}_i)}{|\mathbf{R}_i|^2} - \mathbf{m}_i\right], \tag{3.1}$$

where $\mathbf{R}_i = \mathbf{r}_i - \mathbf{r}_\mu$ is the distance from the muon to spin i.

The number of spins involved in a real sample is on the order of $\sim 10^{23}$, but it is possible to approximate the field at the muon site by summing only over spins inside a Lorentz sphere of radius $\mathrm{r_L}$. For many cases, convergence to the true value of B_{dip} is reached to within $\sim 1\mu$T for $r_{\mathrm{L}} \sim 50$–$100\,$Å. In this approximation, the dipolar field resulting from spins within a distance r_{L} is calculated, and a compensating Lorentz

field is added to approximate spins further away:

$$\mathbf{B}_{\mathrm{L}} = \mu_0 \mathbf{M}/3, \tag{3.2}$$

where $\mathbf{M}$ is the magnetisation of the Lorentz sphere. Additionally, there is a demagnetising field resulting from the divergence of $\mathbf{M}$ at the surface of the sample:

$$\mathbf{B}_{\mathrm{demag}} = -\mu_0 \mathbf{N} \cdot \mathbf{M}, \tag{3.3}$$

where $\mathbf{N}$ is the demagnetising tensor. For the specific cases of an antiferromagnet, or a distribution of randomly oriented or rapidly fluctuating spins, $\mathbf{M} = 0$.

Once the field or field distribution has been calculated, it can be converted into a muon asymmetry spectrum. There are two basic cases for this: static spins and dynamic spins. More specific functions, corresponding to special cases of magnetic field distributions, will be introduced later as necessary. A thorough discussion of asymmetry functions can be found in Refs. 4 and 8.

For a muon in a static local dipolar magnetic field of modulus $|B|$ at an angle θ to the original muon spin polarisation, the time evolution of the polarisation is

$$P_z(t) = \cos^2(\theta) + \sin^2(\theta) \cos(\gamma_\mu |B| t)\,. \tag{3.4}$$

For a polycrystalline sample, this function can be averaged over all angles to give

$$P_z(t) = \frac{1}{3} + \frac{2}{3} \cos(\gamma_\mu |B| t)\,. \tag{3.5}$$

For a system of dynamic spins, the function in Eq. 3.4 can be modified using the "strong collision" approximation. In this approximation, we assume the muon experiences a field that fluctuates as a Markov process; it experiences a series of sudden, uncorrelated changes in the field. $P_z(t)$ for general fluctuating spins is described by the dynamical Kubo Toyabe function (this is derived in Ref. 8), but a simplification can be made in the limit of fast fluctuations: where $\nu/\gamma_\mu\Delta \gtrsim 20$ (Δ is the half width

at half maximum of the static field distribution). For values of ν in this limit, it can be assumed that the relaxation tends towards an exponential [8]

$$P_z(t) \propto \exp\left(-2\gamma_\mu^2 |B|^2 t/\nu\right). \tag{3.6}$$

From this result, it follows that faster fluctuations will result in a faster dephasing of the muons' spins. An alternative interpretation is that the faster the fluctuations, the more Markovian changes in field have passed for each data point in the asymmetry spectrum, and the more uncorrelated the spins are (in fact, the polarisation function gives precisely a measure of the autocorrelation of fluctuating spins). By measuring the asymmetry, which often is over timescales much larger than $1/\nu$, it is possible to extract information about spin dynamics in the range 10^{-4}–10^{-11} s.

In a system containing a combination of static and dynamic spins, for example in $LiOsO_3$ [18], it can be assumed that the muon's polarisation evolves as a product of the individual polarisation functions resulting from the individual static and dynamic spin distributions [8].

Finally, in order to examine the fit of the polarisation function to the experimental data (the theoretical polarisation functions in Eqs. 3.4, 3.5, and 3.6 are normalised such that the initial polarisation is 1 and the baseline polarisation is 0), it can be straightforwardly converted into an asymmetry $A(t)$:

$$A(t) = A_\mathrm{r} P_z(t) + A_\mathrm{b}. \tag{3.7}$$

The relaxing asymmetry A_r is measured experimentally and gives a measure of the fraction of the muons experiencing a magnetic field inside the sample; usually $A_\mathrm{r} \approx 20 - 30\%$, but may be lower for small samples, small magnetic volumes, or a high applied field (which bends muons out of the path of the sample). A_b is the baseline asymmetry, which is also experimentally measured, and this gives a fraction of the muons landing in non-magnetic volumes of the sample, as well as muons landing in the cryostat, sample holder, and other parts of the sample environment.

3.2 Monte Carlo simulations

DFT and DFCs work well for simple spin systems, or those constrained by symmetry or by experimental data such that there only exist a small number of possible ground state configurations. For more complicated systems, it is necessary first to constrain the space of possible ground states. One method to do so is by using Monte Carlo (MC) simulations.

The Monte Carlo method has found an enormous range of applications, not only in statistical physics [19], but also in artificial intelligence [20], economics [21], and climate modelling [22]. A specific subset of the Monte Carlo method is the Metropolis-Hastings algorithm (hereafter called the Metropolis algorithm), a Markov chain Monte Carlo method used for generating probability distributions and predicting observables [23]. The Metropolis algorithm is particularly useful in the context of condensed matter physics, and has often been used to predict the ground states of spin systems and to calculate measurable quantities such as the magnetisation and heat capacity [19, 24]. For large ensembles with a highly correlated Hamiltonian (i.e. the Hamiltonian is not sparse), it is often computationally impossible to examine its thermodynamic properties by diagonalising the Hamiltonian and generating the partition function.

The Metropolis algorithm for spin systems can be described as follows.

1. Generate a random spin distribution D_0.
2. For each temperature T:
   (a) For each iteration i:
      i. Generate a new spin distribution D_i. D_i is related to D_{i-1} in a manner which will be discussed below.
      ii. Compute the energy change[1] of the system for the transition $D_{i-1} \rightarrow D_i$: $\Delta E(D_{i-1}, D_i) = E_{D_i} - E_{D_{i-1}}$.
      iii. Generate a random number ρ in $[0, 1]$.

[1] This energy change is most often calculated from the Hamiltonian.

iv. Accept D_i if $e^{-\Delta E(D_{i-1},D_i)/k_\mathrm{B}T} \geq \rho$, or reject D_i (and leave the configuration unchanged) if $e^{-\Delta E(D_{i-1},D_i)/k_\mathrm{B}T} < \rho$.

(b) Measure any variables after a certain maximum number of iterations, or after the system has converged to its ground state.

(c) Decrease the temperature by some ΔT.

At high temperatures, the probability of a new spin configuration becoming accepted is usually large (as $\lim_{T\to\infty} e^{-\Delta E(D_{i-1},D_i)/k_\mathrm{B}T} = 1$), while at low temperatures, it is hoped that the system tends to the ground state D_GS (where $\Delta E(D_\mathrm{GS}, D_i) \geq 0 \ \forall \ D_i$) as $\lim_{T\to 0} e^{-\Delta E(D_\mathrm{GS},D_i)/k_\mathrm{B}T} = 0$.

The nature of the configuration change varies by application. In many applications, a change $D_{i-1} \to D_i$ involves flipping a single spin. Each subsequent iteration then targets another individual spin, such that the algorithm will eventually flip each individual spin a large number of times. It is also possible to generate a completely new spin configuration for each D_i, which flips a random number of spins. Some specific systems, for example the spin ices discussed in Chap. 4, can harness the topological constraints of the system to generate spin flips consisting of loops of neighbouring spins [24, 25, 26], and will be discussed later.

Parallel tempering is a further technique that can be used to find the true ground state of a frustrated magnetic system, where flips between low energy states often have high energy intermediate barriers, thus making it likely that the system could become stuck in a local minimum. Here all of the MC steps at all temperatures are run simultaneously, and configurations at different temperatures T_i and T_j are swapped with probability $p = \min\left(1, \exp\left[\Delta E\left(D_i, D_j\right)\left(\frac{1}{T_i} - \frac{1}{T_j}\right)\right]\right)$. This allows the system to relax at all temperatures simultaneously towards the 'true' ground state at the global energy minimum.

As well as its use in finding the ground state of a spin system, the Metropolis algorithm can be used to model the Brownian motion of spin flips in order to study

the dynamics of such excitations in some systems [27]. Both of these applications will be presented in Chap. 4.

3.3 Conclusion

This chapter introduces the theoretical techniques used in this thesis. In order to pinpoint the physical phenomena behind an observed effect in a magnetic material, it is vital to deduce its microscopic magnetic configuration. DFT and DFCs assist in the interpretation of μSR data and allow us to draw links between the experimental data and theoretical models. While MC simulations provide guidance for DFCs, they are also powerful in their own right for determining ground states and modelling spin dynamics. These techniques often require some prior knowledge of the system (e.g. symmetry constraints deduced from x-ray diffraction, or magnetic configurations from powder neutron diffraction). The MC simulations require a Hamiltonian, which can be taken from theoretical models, and may be further be refined by experiments (e.g. inelastic neutron scattering).

4

Proposal for the detection of magnetic monopoles in spin ice via nanoscale magnetometry

The magnetic monopole is a key example of an emergent phenomenon in condensed matter physics. This chapter proposes several experiments that could provide the first microscopic observation of magnetic monopoles in the spin ices materials. I simulate the magnetic field inside a spin ice, as would be seen by a muon implanted in the sample, and demonstrate that an observation of magnetic monopoles via this method is currently out of the experimental resolution available. I then simulate the magnetic field close to the surface of the sample. I show that the fluctuations in the field arising from the dynamical behaviour of a small number of monopoles can be uniquely identified through their magnetic noise spectrum. I then discuss three different detection platforms: muon spin rotation (μSR), nitrogen-vacancy (NV) magnetometry, and nanoscale arrays of superconducting quantum interference devices (nanoSQUIDs). By utilising these techniques, it should be possible to experimentally

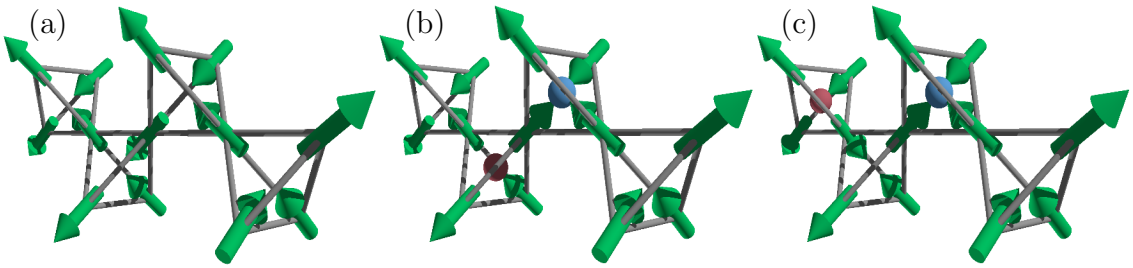

Figure 4.1: (a) Spin ice in its two-in-two-out ground state. (b) After a single spin flip, there is one three-in-one-out and an adjacent one-in-three-out tetrahedron, corresponding to a monopole-antimonopole pair. (c) Subsequent spin flips allow the monopole-antimonopole pair to move independently.

constrain parameters such as the monopole density and hop rate as a function of temperature. This chapter is based on work published in Ref. 27.

Felix Flicker, Norm Yao, and Stephen Blundell provided help in the theoretical interpretation of my results. Stephen Blundell also designed the μSR experiment. The muon site in DTO was determined by Franz Lang. Amir Yacoby designed the NV centre experiment. All computations were run on the Odyssey cluster supported by the FAS Division of Science, Research Computing Group at Harvard University. μSR experiments were carried out on the HAL-9500 spectrometer at the Paul Scherrer Institut, Switzerland with the assistance of Robert Scheuermann and Tatsuo Goko. Dharmalingam Prabhakaran synthesised the DTO sample.

4.1 Introduction

Although fundamental magnetic monopoles have so far proven elusive, it has recently become possible to study properties of monopole-like excitations in condensed matter systems [28]. The spin ices, in particular dysprosium titanate ($Dy_2Ti_2O_7$, DTO) and holmium titanate ($Ho_2Ti_2O_7$, HTO), have been identified as promising candidates to host such elementary excitations [29, 30, 31, 32]. The magnetic rare earth metal ions (Dy^{3+} or Ho^{3+}) and the non-magnetic Ti^{4+} ions are arranged on two separate interpenetrating pyrochlore sublattices, each consisting of a network of corner-sharing

tetrahedra. The rare earth moments ($\approx 10\ \mu_B$) are well-modelled as classical Ising spins, constrained by the crystal field to lie along the local $\langle 111 \rangle$ axes. Exchange and dipolar interactions acting in this lattice geometry result in the four spins in each tetrahedron adopting a ground state in which two spins point towards, and two away from, the tetrahedron's centre [see Fig. 4.1(a)]. This is termed the 'ice rule', by analogy with protons in water ice [29, 33], and leads to a macroscopic degeneracy in the ground state, with six possible spin configurations per tetrahedron.

The elementary excitations in spin ice consist of single flipped spins, which can fractionalise into a pair of monopoles, each travelling through the lattice by successive spin flips [30]. These monopoles manifest themselves as sinks and sources of magnetisation, corresponding to tetrahedra in the three-in-one-out or one-in-three-out configurations [34, 35, 36] [see Figs. 4.1(b) and (c)]. If only nearest neighbour interactions are considered, the monopoles may propagate through the lattice at no energy cost. Including the dipolar interactions between spins, the inter-monopole interaction has the form of Coulomb's law, completing the analogue to fundamental magnetic monopoles [30, 37, 38] and allowing the spin ice state to be described as a $U(1)$ classical spin liquid [39]. Unambiguous observation of the individual monopoles in spin ice would not only confirm this theoretical picture, but would allow these excitations and their dynamics to be studied directly.

Several experiments have provided support for the existence of monopoles, at least indirectly. First, sharp 'pinch point' features, indicating long-range correlations, have been observed in neutron scattering experiments. These were originally taken as proof that widely-separated tetrahedra obey the two-in-two-out rule, but it was later realised that such features can also come about due to the long range of the dipolar interactions [32, 37]. Measurements of the specific heat show a peak, possibly marking the crossover into the spin ice regime, at $\approx 1.1\,\mathrm{K}$ in DTO and $\approx 1.8\,\mathrm{K}$ in HTO [40]. When the sample is equilibrated for a number of days, however, a second upturn

is found at lower temperatures, suggesting the development of a long-range ordered state, although this state remains to be identified [41]. Third, a magnetic field was applied along [111] which acted as an effective chemical potential to increase the number of monopoles in the sample [42, 43]. In the field/temperature phase diagram a line of continuous phase transitions was found to terminate in a critical point, suggesting a 'gas' of interacting monopoles condensing into a 'liquid' at high enough densities. The direct measurement of the microscopic magnetic field from individual monopoles remains an open challenge.

4.2 Simulations

In order to make quantitative predictions we employ the full dipolar spin ice Hamiltonian:

$$H = -J \sum_{\langle (i,a),(j,b) \rangle} \mathbf{S}_i^a \cdot \mathbf{S}_j^b + D r_{\mathrm{nn}}^3 \sum_{\substack{i>j \\ a,b}} \frac{\mathbf{S}_i^a \cdot \mathbf{S}_j^b}{|\mathbf{R}_{ij}^{ab}|^3} - \frac{3\left(\mathbf{S}_i^a \cdot \mathbf{R}_{ij}^{ab}\right)\left(\mathbf{S}_j^b \cdot \mathbf{R}_{ij}^{ab}\right)}{|\mathbf{R}_{ij}^{ab}|^5}, \qquad (4.1)$$

for spin vectors $\mathbf{S}_i^a = \sigma_i^a \hat{\mathbf{z}}^a$, where $\sigma_i^a = \pm 1$ and $\hat{\mathbf{z}}^a$ is the local Ising axis at the tetrahedral sublattice site $\mathbf{r}^a$ for FCC lattice site $\mathbf{R}_i$. The vector connecting two spins $\mathbf{S}_i^a$ and $\mathbf{S}_j^b$ is thus given by $\mathbf{R}_{ij}^{ab} = \mathbf{R}_{ij} + \mathbf{r}^{ab}$. The exchange energy is $J \approx -3.72$ K for DTO and ≈ -1.56 K for HTO [44, 45]. The dipolar energy $D \approx 1.41$ K for both DTO and HTO [44, 45]. The first term in this Hamiltonian corresponds to nearest-neighbour exchange interactions, with a nearest-neighbour exchange coupling of $J_{\mathrm{nn}} = J/3$ (as the relative orientations of nearest-neighbour $\langle 111 \rangle$ axes give $\hat{\mathbf{z}}^a \cdot \hat{\mathbf{z}}^b = -1/3$). The second term corresponds to long-range dipolar interactions. Though spin ices have been predicted to undergo a first-order phase transition to long-range order below ~ 0.2 K [26], the equilibration time rises dramatically on cooling and such order has not yet been experimentally detected [41, 46, 47].

Simulations were carried out on $4 \times 4 \times 4$ unit cells of spin ice using standard Monte Carlo (MC) procedures [23], consisting of 10^4 cooling steps and 5×10^3 steps

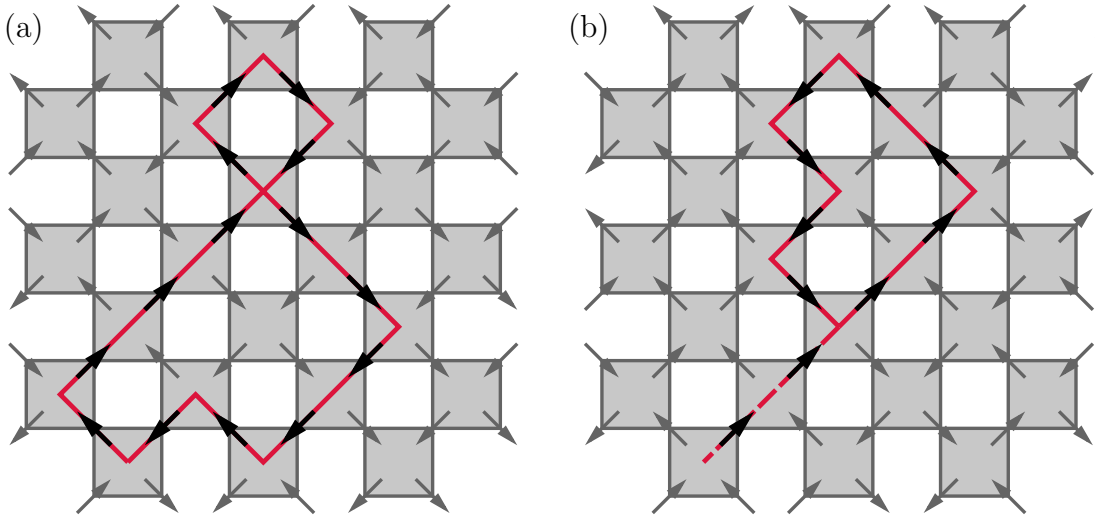

Figure 4.2: (a) A schematic of the long loop and (b) short loop algorithms. In both cases, the solid red line marks the path of the loop, where the black spins are those being flipped. The dashed red line in the short loop algorithm indicates spins which will not be flipped as they are outside the path of the connected loop.

to measure the magnetic fields inside and near to the system at temperatures between 4.5 K and 0.1 K. Each MC step consisted of an attempt to flip every individual spin in the system, along with an attempt to flip a short loop. The Barkema and Newman loop algorithms, originally applied to 2D square ices [48, 49], can be adapted to a 3D pyrochlore model [24]. The algorithms trace a loop of spins throughout the lattice, alternating between 'in' and 'out' spins. The long loop algorithm seeks to form a loop beginning and ending at a specific spin, whereas the short loop algorithm stops once the path traced by the loop passes a spin already in the path, and flips the loop beginning and ending at that spin. These two algorithms are shown schematically in Fig. 4.2. Once a loop has been completed, all spins in the loop are flipped with a Monte Carlo probability (see Sec. 3.2). If the system is in the two-in-two-out state, the state is preserved by a loop flip, but there may be small changes in the dipolar field. Hence, the loop flips may allow a system in a two-in-two-out state to relax to another two-in-two-out state with long range dipolar order. The short loop algorithm was selected for the following simulations as it has the advantage of approaching a

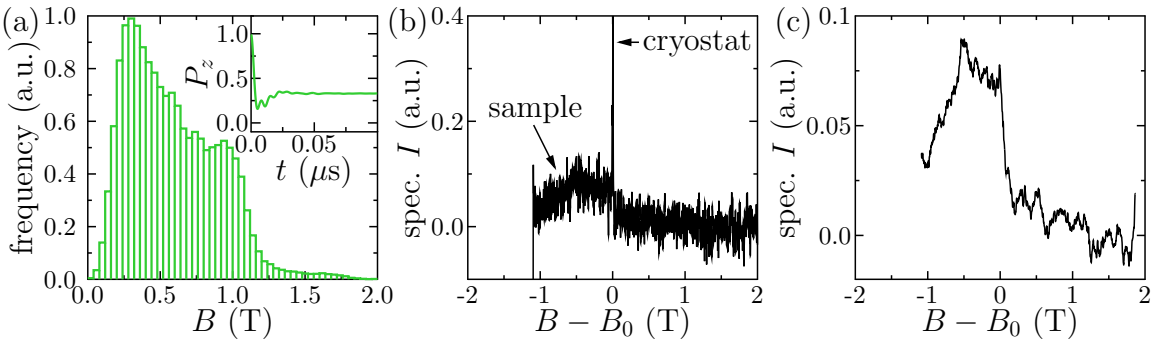

Figure 4.3: (a) The distribution of local magnetic fields (calculated using Monte Carlo simulations and dipole field calculations) at the muon site in DTO. The inset shows the resulting muon polarisation spectrum from this distribution. (b) The experimentally-measured magnetic field distribution of a sample of DTO at 0.125 K in an applied field of $B_0 = 1.1$ T. The peaks arising due to muons in the sample and muons in the cryostat have been labelled. (c) The experimental field distribution of muons landing only in the DTO sample (with $B_0 = 1.1$ T as before); details of how this has been determined are given in the main text.

finite size limit as the system size increases. The long loop algorithm does not, and the loop size scales approximately linearly with the number of spins [24], making this algorithm significantly slower for larger systems.

4.3 The magnetic field inside spin ice

As μSR can be used to directly probe fluctuating spins, one approach to observe the dynamic magnetic field arising from the motion of individual monopoles may be to implant the muon inside a spin ice sample, and infer the rate of field fluctuations (which is related to the monopole hopping rate) from the resulting asymmetry spectrum.

This is, however, challenging due to the large size of the Dy^{3+} and Ho^{3+} moments. Using DFT, we find that the muon site is $(-0.0125, 0.0471, 0.2028)$ in the unit cell, with symmetry group 96g in space group 227. Monte Carlo simulations were used to produce 50 ground state spin configurations of DTO.[1] The configurations were generated by cooling the simulated sample from 5 K to 0.01 K, well below the on-

[1]Due to the degeneracy associated with the two-in-two-out state, this is only a small fraction of the total number of possible ground states.

set temperature of the spin ice state at $\sim 0.4\,\mathrm{K}$ [44]. A muon was then placed at each symmetry-equivalent muon site within these 50 configurations, and the resulting dipolar field distribution (calculated using Eq. 3.1 and utilising periodic boundary conditions) is plotted in Fig. 4.3(a). Using Eq. 3.4, this distribution can be converted into a muon polarisation spectrum [shown in the inset in Fig. 4.3(a)]. We find that muons experience a mean field of 589 mT with a width $\sim 1\,\mathrm{T}$, in agreement with bounds placed by LF-μSR experiments [50] and early theoretical calculations [51]. The B distribution arises because there is a vast range of possible local magnetic environments for a muon, due to six-fold degeneracy associated with a single tetrahedron entering the two-in-two-out state. This large width results in relaxation of the muon asymmetry over $\sim 10\,\mathrm{ns}$, which places this experiment outside of the resolution of most μSR instruments.

The HAL-9500 spectrometer at the Paul Scherrer Institut is a μSR instrument that can operate in TF mode up to 9.5 T. This spectrometer also allows the sample to be mounted in such a way to minimise the background from muons landing in the sample holder.

A representative field spectrum,[2] measured at $T = 0.125\,\mathrm{K}$ in an applied field of $B_0 = 1.1\,\mathrm{T}$ along the $\langle 111 \rangle$ axis is shown in Fig. 4.3(b). The large peak arises from muons in the background signal. The sample mount, which is situated entirely behind the sample, does not contribute to this background signal and so the large peak consists only of muons landing in the cryostat. The background peak is centred at the applied field, as the muons landing in these portions of the experiment do not experience the internal fields of DTO.

There also exists a broad feature in the spectrum, corresponding to the muons landing in the sample. As the number of muons landing inside the sample is found by integrating under this feature, it is expected to have a very low spectral intensity due

[2]The field spectrum is the Fourier transform of the asymmetry spectrum.

to its large width. The data can be processed to remove the background peak, and to smooth some of the noise. The processed spectrum corresponding to the data in Fig. 4.3(b) is shown in Fig. 4.3(c). The background peak was fitted to a Lorentzian curve, which was subsequently subtracted. The data were then smoothed using a Savitzky-Golay filter [52].

When a magnetic field is applied to DTO or HTO along $\langle 111 \rangle$, the spins in each tetrahedron attempt to align with the field while also remaining parallel or antiparallel to their local $\langle 111 \rangle$ axis. At a sufficiently high field (approximately 1 T), it becomes favourable for tetrahedra to lie in the three-in-one-out or one-in-three out configurations [42, 53] in order to satisfy this condition. Thus, the application of a magnetic field is expected to increase the monopole concentration. However the equilibration time of DTO at 0.125 K is expected to be very large, and therefore we expect that the system is still in the ground state in our measurements.

While it is possible to qualitatively observe a similarity between the theoretical and experimental field distributions at the muon site in DTO, this measurement highlights the difficulty involved in quantifying the behaviour of monopoles inside the sample, and provides motivation to explore other possible options for studying monopoles in the spin ices.[3]

4.4 Nanoscale magnetometry and the noise spectrum

Nanoscale magnetometry near the surface of a sample can be used as an alternative to placing a probe directly inside the material. As a magnetic monopole passes close to the surface of spin ice, its motion causes the dipolar field at the probe location to fluctuate; a simple example for a monopole in a square ice is shown in Fig. 4.4.

[3]It should be noted that the internal field distribution in the spin ices can measured using NMR [54], although this technique is not applicable for the study of the dynamical behaviour of monopoles.

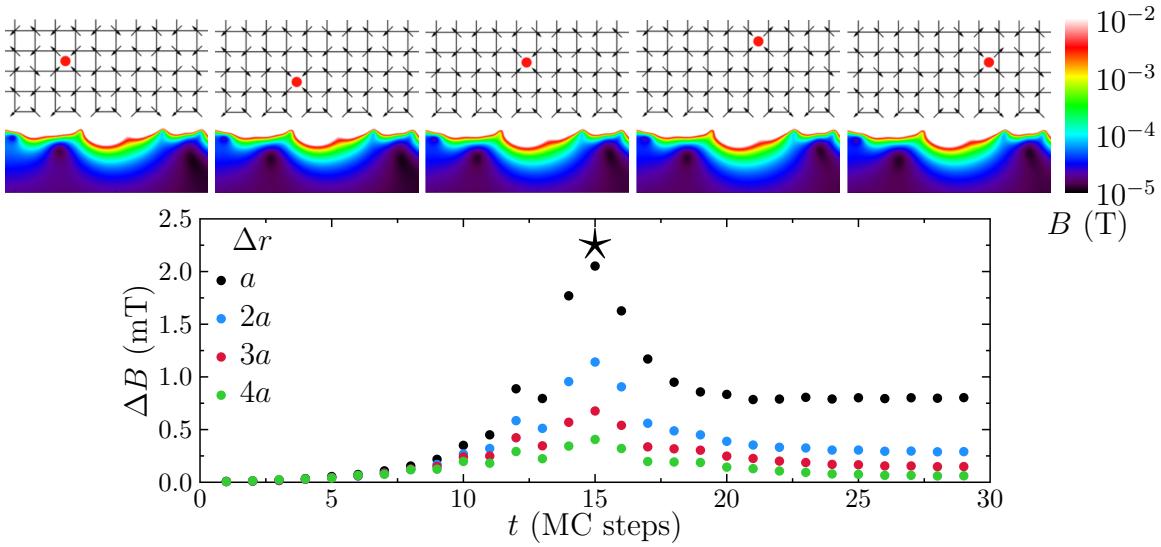

Figure 4.4: The simulated field fluctuations due to a single monopole passing close to the surface in square ice. The top panel shows the the magnetic field contours close to the surface, where the red dot indicates the square containing the monopole excitation. The bottom panel shows the magnitude of the field change (where $\Delta B(t) = B(t) - B(0)$) as the monopole passes probe points at distances $a - 4a$ from the surface, where a is the nearest neighbour spin distance. The star marks the point at which the monopole passes directly over the probe point.

In the following simulations, periodic boundary conditions were used in the $\hat{\mathbf{x}}$ and $\hat{\mathbf{y}}$ directions. The probe point for the stray fields is placed 10 nm from the sample in $\hat{\mathbf{z}}$, and the time dependence of the magnetic field $B(t)$ was calculated by summing the dipolar field produced by all the spins in the film (a schematic of this experimental arrangement is shown in Fig. 4.5). While previously MC simulations were used to generate a ground state configuration in DTO, here their use is restricted to creating a sample spin configuration at a given temperature T, then to modelling the spin flip dynamics (and therefore the monopole motion). This approximation has previously been suggested by experimental results [55].

Three different spin arrangements were studied in order to isolate the characteristics arising from the individual contributions to the Hamiltonian in Eq. 4.1. This leads us to define three distinct models. (i) The dipolar spin ice model (DSIM) uses the J and D parameters of DTO. (ii) The nearest-neighbor spin ice model (NNSIM) has

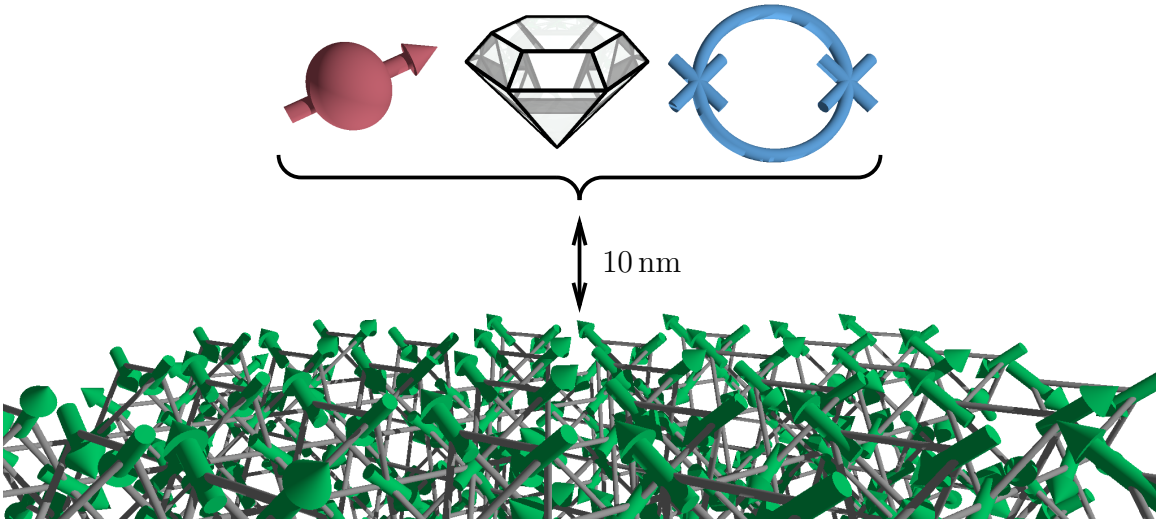

Figure 4.5: A schematic of the experimental arrangement for the techniques mentioned in this chapter, with a muon (left), NV centre in diamond (centre), and nanoSQUID (right) acting as ultrasensitive magnetic probes 10 nm from the spin ice.

no long-range interactions ($D = 0$), but retains the topological constraint from Dirac strings[4] connecting monopoles to antimonopoles. J is chosen so that the monopole density is as for the first case, and $J > 0$ ensures that the two-in-two-out ground state is favoured (iii) The all-in-all-out model (AIAO) has $D = 0$ and $J < 0$. The ground state consists of tetrahedra with either four-in or four-out spin configurations. Thermal spin flips in this case are not monopole-like excitations, thus providing a control case.

In Fig. 4.6(a) we show the DSIM prediction for the magnetic field measured at 4 K and 1 K. At 4 K most tetrahedra are not in the two-in-two-out state and a rapidly fluctuating signal is observed. At 1 K the system is close to the ground state with a density of monopoles per tetrahedron of ≈ 0.03, as predicted by Debye-Hückel theory [56]. The monopole density, calculated analytically using the methods described in Ref. 56, is slightly lower in HTO [see Fig. 4.7(e)]. At this density, most tetrahedra

[4]This topological constraint means that the path taken by a monopole cannot be immediately followed by another monopole of the same polarity. For this to be allowed, either the original monopole must first retrace its steps, or a monopole of opposite polarity must traverse the initial path.

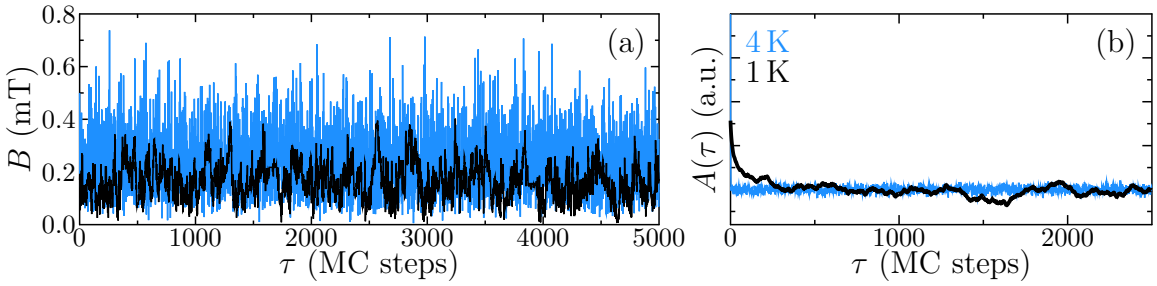

Figure 4.6: (a) The simulated field fluctuations 10 nm from the surface of a sample described by the DSIM at 4 K (blue) and 1 K (black) and (b) their autocorrelation functions, calculated using Eq. 4.3.

obey the ice rules, but there are sufficiently many monopoles that some may hop across the sample without annihilating, resulting in telegraph noise. By comparison, the AIAO features no qualitative distinction between its high- and low-temperature regimes. The amplitude of the field fluctuations are of order 0.1 mT, well within the experimentally-measurable range of the aforementioned techniques.

The timescales in Fig. 4.6(a) are in units of MC steps, the shortest possible timescale on which a spin flip may occur in the model. There has been considerable debate surrounding the timescale on which spins flip in the physical systems at low temperature, with ac susceptibility measurements suggesting a scale of ~ 1 ms [57, 58, 59, 60, 61], and μSR measurements detecting spin dynamics on a scale of ~ 1 μs [50]. It is possible that this is dependent on the relevant experimental time window ($10^{0} - 10^{-4}$ s for ac susceptibility and $10^{-4} - 10^{-11}$ s for μSR). By performing the nanoscale magnetometry measurements in the future and comparing to the MC time step, the hop rate should be deducible.

In addition to directly probing field fluctuations, complementary information is gained by measuring the noise spectrum $S(\omega)$. Experiments that measure $S(\omega)$ utilise a frequency filter, allowing us to isolate certain dynamical timescales and compare the amplitude of noise at these timescales.

A time-varying field $B(t)$ has a Fourier transform given by $\tilde{B}(\omega) = \int_{-\infty}^{\infty} B(t) \mathrm{e}^{-\mathrm{i}\omega t}\, \mathrm{d}t$.

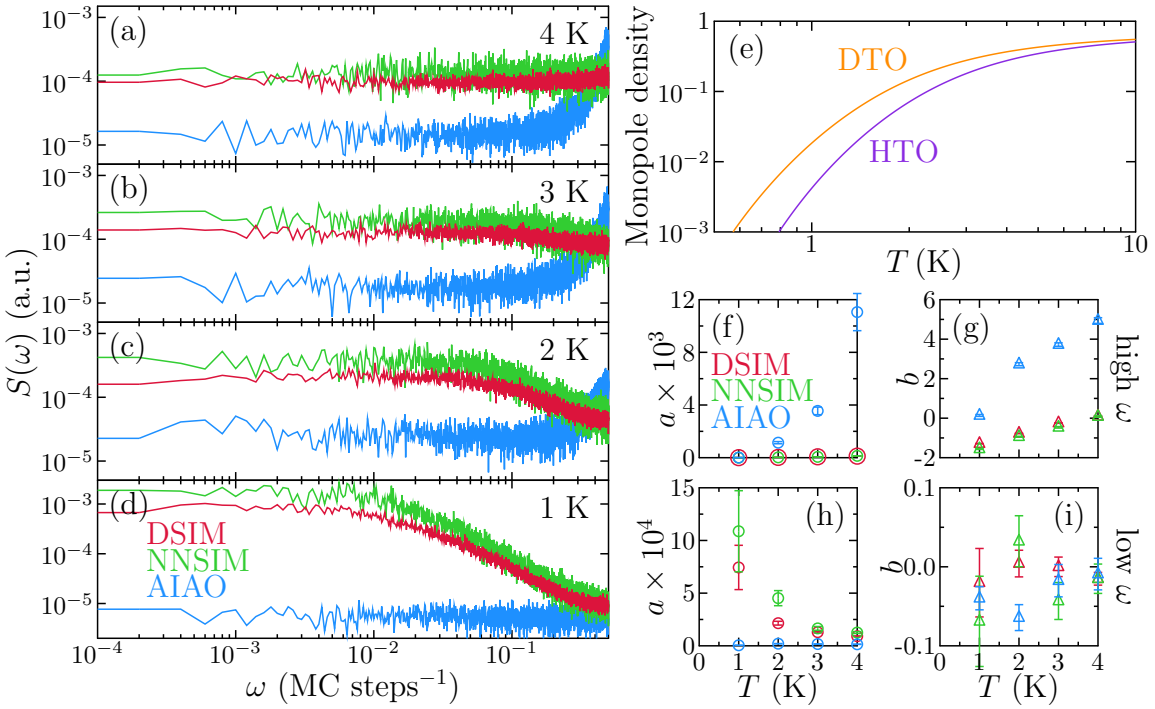

Figure 4.7: *(a–d):* Frequency dependence of noise spectra $S(\omega)$ for DSIM, NNSIM, and AIAO between 4 K and 1 K. *(e):* Evolution of the monopole density in DTO and HTO calculated using Debye-Hückel theory. *(f–i):* Temperature dependence of low- and high-frequency power laws in $S(\omega)$, fitted with $S(\omega) = a\omega^b$.

The noise spectral density is therefore [62, 63]

$$S(\omega) = \langle |\tilde{B}(\omega)|^2 \rangle, \tag{4.2}$$

and is related to the autocorrelation function

$$A(\tau) = \langle B(t)B(t+\tau) \rangle \tag{4.3}$$

by the Wiener-Khinchin theorem [64]

$$S(\omega) = 4 \int_0^\infty A(\tau) \cos(\omega\tau) \mathrm{d}\tau. \tag{4.4}$$

$A(\tau)$ for the DSIM at 4 K and 1 K is presented in Fig. 4.6(b), and the corresponding noise spectra in Figs. 4.7(a–d).

As shown in Fig. 4.7(a), there is little low-frequency structure in $S(\omega)$ at 4 K, corresponding to very little correlation between the field measurements at different times. Fluctuations are predominantly at the Nyqvist frequency [$\omega_{\mathrm{Ny}} = (2 \times$

MC time step)$^{-1}$]. The lack of structure is evident in both DSIM and NNSIM, and shows that it would be difficult to discern monopole dynamics within the temperature range of ^{4}He cryostats. For AIAO, a peak forms at ω_{Ny} as a result of rapid thermal fluctuations. The power spectrum at 1 K, however, shows a clear difference between the DSIM, NNSIM, and AIAO cases. The low-frequency structure seen in Fig. 4.6(a) is manifest in $S(\omega)$. It should be noted that the frequency at which this structure occurs is on the order of $\approx 10^{-2}$ MC steps^{-1}. The DSIM and NNSIM systems both display low-frequency plateaus and a high-frequency power law, which is absent in AIAO. This is a clear indication that the long-range forces play a relatively small role in the monopole dynamics and instead contribute more to the lowering of the overall stray field, as evidenced in a smaller area under the $S(\omega)$ curve. This is consistent with other theoretical studies, which suggest that samples are largely dominated by single monopoles as opposed to closely bound pairs [56]. In AIAO, the field fluctuations are smaller and contain no structure on longer timescales, which is expected as it is always energetically favourable for spin flips to undo shortly after creation. We can make quantitative predictions of the functional form of $S(\omega)$ by fitting power laws ($S(\omega) = a\omega^b$) to the low- and high-ω regimes. DSIM, NNSIM, and AIAO all display low-ω plateaus, with $|b| \sim 10^{-2}$. However, in the high-ω regime there are pronounced differences between the three systems. For AIAO, $b > 0$ at both low and high temperatures, indicative of a system dominated by thermal spin flips. Both DSIM and NNSIM have $b < 0$ at low temperature which increases at high temperatures as thermal spin flips take over and monopole dynamics are no longer observable. The values of a and b for all models in the low- and high-ω regimes are presented in Fig. 4.7(f–i).

4.5 Experimental techniques

We now consider a number of different nanoscale magnetometry techniques which are promising candidates for detecting monopole behaviour in spin ice materials.

4.5.1 Diamond NV magnetometry

First, we consider the use of single spin magnetometery based upon nitrogen-vacancy (NV) point defects in diamond [65, 66]. An NV centre consists of a nitrogen atom and a vacancy introduced into adjacent sites in the diamond lattice. The nitrogen and vacancy couple to form an $S = 1$ electronic spin orientated along one of the four diamond carbon-carbon bond directions. In addition to coherent manipulations via resonant microwave pulses, the NV centre's spin state can be optically initialised and detected [67, 68, 69]. There are two possible setups for NV-based monopole magnetometry: (a) a scanning NV magnetometer, consisting of a diamond nanopillar attached to an AFM tip [70], and (b) a bulk diamond surface containing a shallow layer of NV centres approximately $\sim 5 - 10\,\text{nm}$ deep, where the spin ice sample is placed in direct proximity to this surface.

To detect the characteristic signatures of individual magnetic monopoles, the NV can be utilised in two possible modes:

1. direct measurement of the stray magnetic field from a monopole (dc magnetometry), and
2. spectroscopy of the ac magnetic noise generated by the dynamics and fluctuations of a dilute monopole density.

In the case of dc magnetometry, one would observe Zeeman shifts in the NV resonance frequency (between the $|m_s = 0\rangle$ and $|m_s = -1\rangle$ spin states) in real time in order to measure the stray field of a monopole as it passes through the sensing volume of a single shallow NV centre. This can be achieved using either Ramsey spectroscopy or continuous-wave optically detected magnetic resonance spectroscopy.

Ramsey spectroscopy allows us to probe the field at the NV centre by applying two $\pi/2$ pulses separated by an integration time t. From this, we can deduce the local magnetic field experienced by the NV centre during t. Continuous-wave optically detected magnetic resonance spectroscopy uses both microwaves and an optical laser to excite and detect the splitting between the $|m_s = 0\rangle$ and $|m_s = -1\rangle$ states. The field sensitivity of the dc approach is limited by T_2^*, the NV dephasing time, leading to a sensitivity $\sim 5\,\mu\mathrm{T}/\sqrt{\mathrm{Hz}}$ [71]. Assuming an integration time $\sim 250\mu$s this enables a field sensitivity of approximately ~ 0.3 mT and a corresponding dc sensing volume of approximately ~ 10 nm surrounding the NV centre. This sensitivity is sufficient to detect the real time dynamics of individual monopoles.

For ac magnetometry, we are interested in the individual Fourier components of the time varying magnetic field. To generate such a frequency filter, the NV centre is manipulated using a series of periodic microwave pulses separated by a free-evolution time τ. This modulation creates a narrow band-pass frequency filter at $1/\tau$; by varying the free-evolution time, one can map out the noise spectral density associated with magnetic fluctuations. Compared to the dc case, the key advantage of this approach is that the field sensitivity is no longer limited by T_2^* , but rather by T_2, the intrinsic spin decoherence time of the NV centre. For shallow-implanted NVs, this yields a field sensitivity ~ 50 nT$/\sqrt{\mathrm{Hz}}$ [71]. Assuming an integration time $\approx 250\,\mu$s this enables a field sensitivity of approximately $\approx 3\,\mu$T which is well within the desired sensitivity.

4.5.2 Low energy μSR

While μSR is usually a bulk probe, a low-energy variant [72], in which the energy of the muon beam can be continuously varied from 0.5 to 30 keV, provides an extension of the technique which allows depth-dependent studies of thin films and multilayered structures in the range from ~ 1 to ~ 200 nm. This allows for experiments involving

proximal magnetometry [73] in which the field close to an ultrathin magnetic layer can be probed. μSR probes fields fluctuating on a timescale $\sim 10^{-11}$–10^{-5} s. In the cases of ZF-μSR or LF-μSR (in an external field $B_{\rm L}$), the relaxation rate λ of the muon polarisation spectrum can be related to the autocorrelation function of the components of $\mathbf{B}^{\perp}(t)$, the local field transverse to the muon, using

$$\lambda = \frac{\gamma_\mu^2}{2} \int_0^\infty \langle \mathbf{B}^{\perp}(t) \cdot \mathbf{B}^{\perp}(0) \rangle \mathrm{e}^{\mathrm{i}\gamma_\mu B_{\rm L} t}\, \mathrm{d}t. \tag{4.5}$$

The relaxation rate λ is then proportional to the power spectrum at $\omega = \gamma_\mu B_{\rm L}$. As shown in Sec. 4.3(a), the field inside spin ice is very large at the muon site, but outside the sample the field is dominated by a long-range stray field [50, 74]. Our interest here is in the nanoscale stray field fluctuations close to the surface. A potential disadvantage of these techniques is that the stopping profile of slow muons or other polarised probes is not sharp, so that implantation occurs at a range of depths.

4.5.3 nanoSQUID arrays

The third experimental method employs arrays of nanoSQUIDs. The superconducting quantum interference device (SQUID) is an extremely sensitive detector of magnetic flux, and decreasing its size leads to a highly versatile sensor of local magnetic fields [75, 76], with a spin sensitivity that has reached below a single Bohr magneton [77].

4.5.4 Experimental considerations

The experimental techniques above have different advantages and drawbacks. The nanoSQUID technique, despite excellent sensitivity and the ability to work at the required temperature regime, may suffer from a large spatial averaging of fields across the area of the sensor ($\sim 10^5$ nm^2). This is much larger than that for the polarised probes and NV centres for which the active sensor is essentially point-like. Low energy muons, though point probes, can only be implanted over a range of depths. Thus a

suitable overlayer can be deposited on the surface of spin ice and muons implanted into it, but the observed signal will average over a spread of distances between the spin ice surface and the probe. The energy of the incoming muons controls both the implantation depth and the distribution of stopping depths, and so this parameter could be tuned to minimise the spread. NV centres may be much better in this regard, though measurements need to be obtained with an applied magnetic field, which is not the case for μSR.[5]

Both μSR and NV magnetometry experiments are currently limited to temperatures above 4.2 K by the use of ^{4}He cryostats.

In general, one expects a range of timescales to be important in $S(\omega)$ originating from a slowing of dynamics heading out of equilibrium at the lowest temperatures. The nanoscale probes proposed can cover a wide range of frequencies from $10^0 - 10^{-4}$ s (NV magnetometers) through $10^{-5} - 10^{-11}$ s (μSR) in order to probe the relevant dynamics and to understand the scaling between experimental timescales and those used in MC simulations, both of which can be tuned by temperature.

The role of the sample surface may be important as it is thought that different surface termination directions may produce 'orphan spins' localised at the surface [78]. A uniform surface of dipoles would produce a field $\propto 1/r^2$ which would be distinguishable from the effect of a $1/r$ monopole field, but, most importantly, surface monopole charges are likely to be largely static (as monopoles have lower energy staying at surface and are fixed by the topological constraints acting there), so there would be little contribution to $S(\omega)$. However, if there were to be monopoles moving in a correlated manner across the surface, this could mask the signal from the bulk.

This effect may also manifest in rough surfaces, where it may be possible for orphan spins to become trapped. However, these surface effects are not known in any

[5] As mentioned previously, the application of a magnetic field may cause an increase in the density of monopoles in the sample. However, for a small field and low temperatures, this effect is expected to be negligible.

detail as the existing theoretical studies use minimal models that attempt to explore the effect of altered nearest-neighbour coupling parameters at the surface [78, 79].

The best experimental strategy would be to measure the noise spectra close to the surface in samples with different surface terminations (surfaces cut parallel to the (100), (110) or (111) planes, where different effects are expected [79]) and also with different surface roughnesses (by controlling film growth conditions and/or annealing samples, and measuring the surface roughness using small-angle x-ray and neutron scattering).

4.6 Conclusion

This chapter presents a road map for future experiments of monopole behaviour using nanoscale magnetic probes of the noise spectrum of the dipolar field measured very close to the surface of spin ice. While measurements inside the sample are challenging, we show that the magnetic field fluctuations resulting from individual, or small ensembles of, magnetic monopoles can be detected close to the surface. The proposed techniques have varying advantages and disadvantages and need to be extended to the 1 K regime where the monopole density is sufficiently low that observation of magnetic monopoles is possible. When such experiments are able to reach temperatures of $\approx 1.5\,\mathrm{K}$, there are clearly-discernible, qualitative signatures of two key characteristics of magnetic monopoles: their Coulomb interaction and topological constraints deriving from Dirac strings. Unconstrained thermal spin flips feature a Debye-type noise spectral density, matching that of Brownian motion, with a low-frequency plateau followed by a turnover to inverse-square flicker noise at characteristic timescale τ. Coulomb interactions between Brownian particles decrease the timescale τ through the recombination of particle/antiparticle pairs [27]. An observation of the magnetic noise spectrum predicted in this chapter would open up an era of direct measurement of monopole transport in these topologically constrained systems and provide new

insight into the classical $U(1)$ spin liquid. There are many possible extensions to these experiments, for example by the use of two probes in NV magnetometry. Such measurements could identify and time the hops of single magnetic monopoles, helping constrain system parameters.

5

Spin Jahn-Teller antiferromagnetism in $CoTi_2O_5$

While there are many examples of materials exhibiting the Jahn-Teller effect, the *spin* Jahn-Teller effect is much rarer. In this chapter, I present an in-depth study of the spin Jahn-Teller effect in $CoTi_2O_5$, which employs magnetometry, heat capacity, μSR, neutron powder diffraction, DFT, and DFCs to understand the magnetic ordering of this system and its coupling to a symmetry-required structural distortion. $CoTi_2O_5$ has a much lower crystal symmetry than other spin Jahn-Teller systems, and this work shows that this effect may be present in a much wider class of materials than previously thought. This chapter is based on the work in Ref. 80.

Stephen Blundell assisted with the μSR experiment and the theoretical interpretation of results. Franz Lang assisted with the μSR experiment and carried out the DFT calculations. Roger Johnson carried out the neutron powder diffraction (NPD) experiment and the subsequent symmetry analysis. Dmitry Khalyavin and Pascal

Manuel assisted with the NPD experiment. The $CoTi_2O_5$ sample was synthesised by Dharmalingam Prabhakaran.

5.1 Introduction

In systems with an orbital degeneracy, the degeneracy may be lifted through a spontaneous breaking of structural symmetry [81]. This is the Jahn-Teller effect. There also exists an analogous, albeit much rarer, spin Jahn-Teller effect, in which the degeneracy lies in the spin, rather than the orbital, degrees of freedom. This effect occurs in several highly-symmetric compounds, in which the onset of magnetic order can produce frustration which in turn is relieved via a structural distortion. Examples include some pyrochlore materials [82, 83] and spinels [84, 85], where tetragonal distortions occur at the onset of magnetic order. A similar effect has also been reported in molecular wheels [86, 87].

$CoTi_2O_5$ possesses a relatively lower-symmetry structure compared to the pyrochlores and spinels; the space group is $Cmcm$. The site symmetry of the magnetic Co^{2+} ($3d^7$) ion is $m2m$ (C_{2v}), meaning no conventional Jahn-Teller transition occurs as the orbital levels are already non-degenerate.

Cobalt titanates are of interest due to their numerous applications. Co_2TiO_4 has a complex spinel magnetic structure [88, 89, 90, 91], which has found uses in catalysis [92, 93], microwave devices [94], and Li-ion cells [95]. $CoTiO_3$ has been used as a photocatalyst [96], gas sensor [97], and also in semiconductor transistors and memory storage [98]. $CoTi_2O_5$, however, is less well-studied. It is the only cobalt titanate to melt incongruently [99], and its pseudo-brookite structure [100] is an entropy-stabilised high temperature phase [101] which is susceptible to decomposition below 1414 K [102, 103]. Only recently has it become possible to synthesise high-quality single crystals of $CoTi_2O_5$ [104].

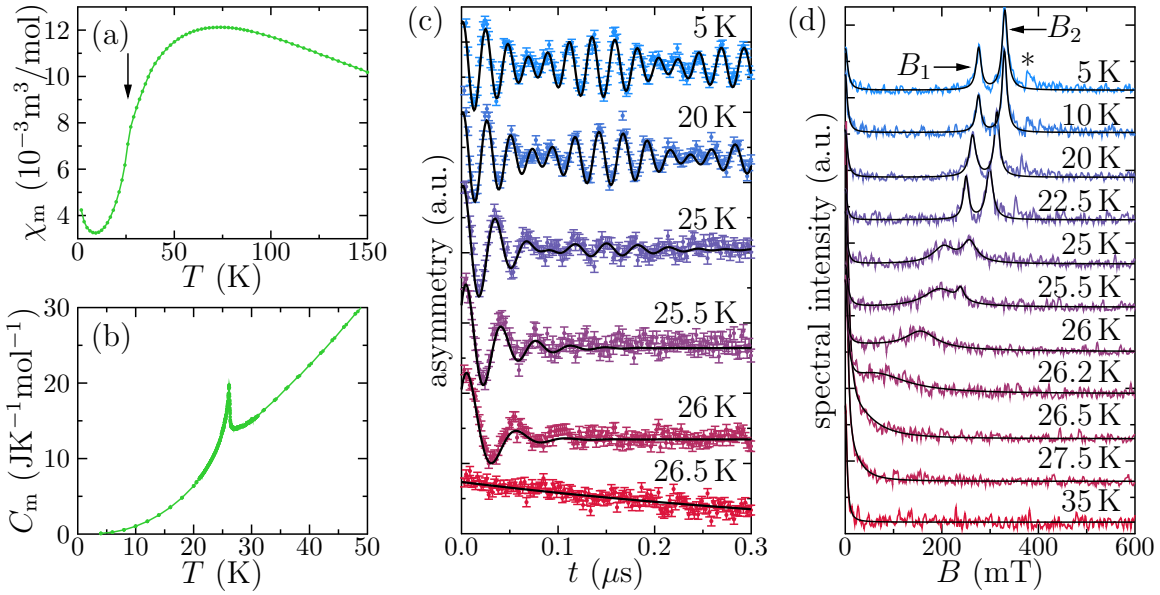

Figure 5.1: (a) Magnetic susceptibility of $CoTi_2O_5$ measured in an applied field of $\mu_0 H = 10\,\mathrm{mT}$. The arrow marks a kink at T_N. (b) Molar heat capacity. (c) ZF-μSR spectra above and below T_N. Fits to Eq. 5.2 are also plotted. (d) The Fourier transform of these spectra with fits with Eq. 5.1. The asterisk indicates an additional feature, which may arise due to site mixing.

5.2 Identification of magnetic order

A high-quality single crystal $CoTi_2O_5$ sample was prepared using the method described in Ref. 80.

5.2.1 Magnetometry and heat capacity

The magnetic susceptibility measurements were made using a Quantum Design MPMS. The heat capacity measurements were made using a Quantum Design PPMS. Magnetic susceptibility and heat capacity data are shown in Fig. 5.1(a) and (b) respectively and are consistent with a magnetic transition at a Néel temperature $T_N \approx 26\,\mathrm{K}$. The calculated entropy $\Delta S = \int (C/T)\,\mathrm{d}T$ associated with the transition is 48% of the expected $R\ln(2J+1) = R\ln(4)$ associated with the spin-only moment, indicative of significant correlations above T_N.

5.2.2 ZF-μSR

ZF-μSR experiments [4, 105] were performed using a Quantum Continuous Flow Cryostat mounted on the general purpose spectrometer (GPS) at the Swiss Muon Source. All of the μSR data were analysed using WiMDA [106].

ZF-μSR asymmetry spectra $A(t)$ are shown in Fig. 5.1(c). At low temperature, we observe an oscillatory beating pattern of $A(t)$, along with two peaks in the Fourier transform spectra [Fig. 5.1(d)]. This is indicative of long-range magnetic order and two inequivalent muon stopping sites. The data can be fitted either in the time domain or in the field domain.

Below T_{N}, the spectral intensity $I(B)$ in the field domain can be modelled with a sum of three Lorentzian distributions:

$$I(B) = I_1 L(B; B_1, \lambda_1) + I_2 L(B; B_2, \lambda_2) + I_{\mathrm{b}} L(B; 0, \lambda_{\mathrm{b}}), \tag{5.1}$$

where $L(B; B_i, \lambda_i)$ is a Lorentzian distribution centred on B_i with a width λ_i/γ_μ. The first two terms correspond to muons precessing in the internal fields of the sample; the two frequencies correspond to the two different dipolar fields at symmetry-inequivalent muon stopping sites. The Lorentzian distribution associated with each precession frequency indicates a small spread in the magnetic field distribution at the muon site, possibly due to the site disorder that has been observed between the Co and Ti sites in $CoTi_2O_5$ [100], small fluctuations of the Co moments, or due to muons near the boundaries of magnetic domains. The third term consists partially of a background signal, corresponding to muons which land in the cryostat and sample holder, and therefore do not experience any of the sample's internal fields. There is an additional contribution to the third term arising from the component of the local field at the muon site that is longitudinal to the initial muon polarisation. The small width of this component, $\lambda_{\mathrm{b}} \approx 4\,\mathrm{mT}$ for all T, may be due to these muons experiencing a small field close to the surface of the sample, or due to a spread of longitudinal fields.

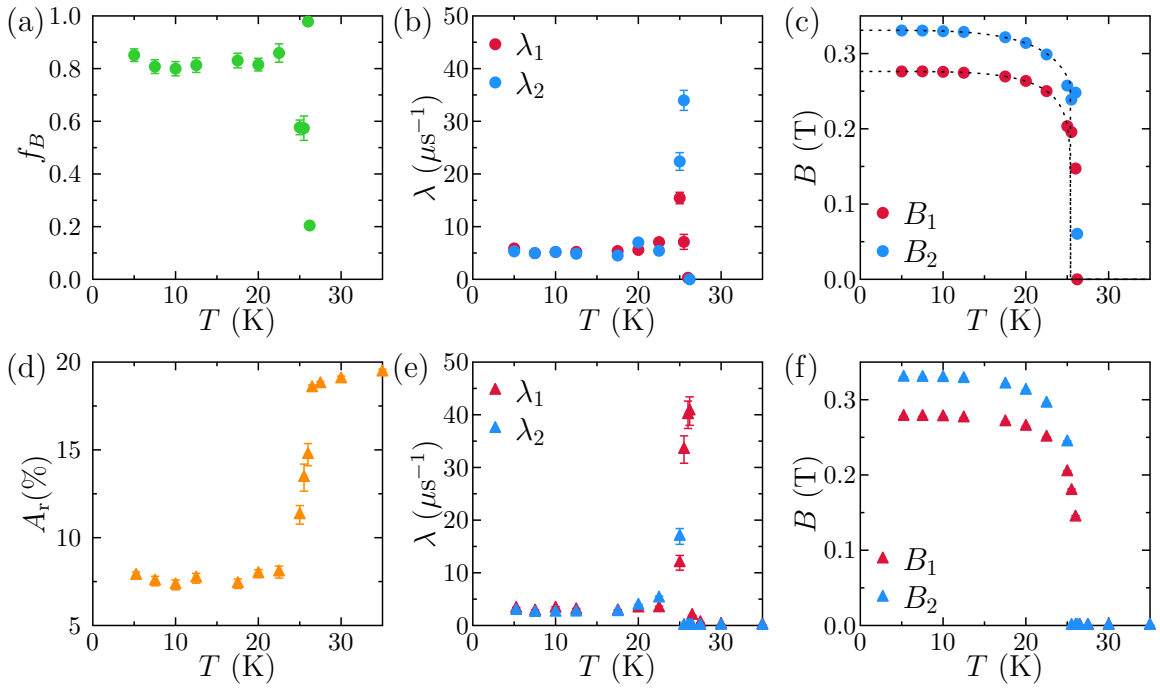

Figure 5.2: (a) Temperature dependence of the fraction of muons experiencing a coherent magnetic field. Temperature dependences of the peak width and centers, as fitted from Eq. 5.1 applied to the Fourier transform of the ZF-μSR spectra, are shown in (b) and (c) respectively. The dotted lines in (c) show phenomenological fits to $B = B_0\,(1-(T/T_\mathrm{N})^\alpha)^\beta$. (d) The temperature dependence of the fitted relaxing asymmetry (using Eq. 5.2). The temperature dependences of the relaxations and local fields at the muon sites are shown in (e) and (f) respectively.

The fraction of muons contributing to each peak in Fig. 5.1(d) f_i is given by the integral under that peak. The total fraction of muons experiencing a non-zero field, $f_B = (f_1+f_2)\,/\,(f_1+f_2+f_3)$, is plotted in Fig. 5.2(a). The drop in f_B above $\mathrm{T_N}$ marks the transition into the paramagnetic state.

The fitted values from Eq. 5.1 for the T evolution of λ_i and B_i are presented in Figs. 5.2(b) and (c) respectively. As T increases towards T_N, the two peaks broaden and merge, while their centers move towards 0 T as the long-range ordered magnet transitions to the paramagnetic regime. The data in Fig. 5.2(c) were fitted with the phenomenological formula $B = B_0\,(1-(T/T_\mathrm{N})^\alpha)^\beta$, giving $T_\mathrm{N} = 26.0(11)$ K for both components.[1] We also find values of the internal fields at the muon sites as $T \to 0$:

[1]We also find $\alpha \approx 4$–6 and $\beta \approx 0.1$, although these values are very sensitive to data points in the

$B_1 = 330(3)$ mT and $B_2 = 276(6)$ mT. There appears to be an additional small feature in the data at low temperature at ≈ 400 mT [marked by the asterisk in Fig. 5.1(d)], which may arise due to the site disorder and is discussed below.

The data in Fig. 5.1(a) can be fitted in the time domain using a sum of two oscillating components with a Lorentzian relaxation, and a background term:

$$A(t) = A_{\mathrm{r}} \left[a_1 \cos\left(\gamma_\mu B_1 t\right) e^{-\lambda_1 t} + a_2 \cos\left(\gamma_\mu B_2 t\right) e^{-\lambda_2 t} \right] + A_{\mathrm{b}}. \tag{5.2}$$

The first two terms correspond to muons precessing in the internal fields of the sample, as described for the field domain fitting. The relative amplitudes of these two components were fixed to their low temperature values ($a_1 \approx 0.37$; $a_1 + a_2 = 1$). The third term contains contributions from both the background and longitudinal field at the muon site ($A_{\mathrm{b}} \approx 5\%$), which is also discussed above. The discontinuity in the relaxing asymmetry A_{r}, shown in Fig. 5.2(d), marks the transition into the ordered state, with the drop in asymmetry likely due to a fast-relaxing component outside the resolution of the spectrometer. The fitted values of the relaxations λ_i and internal fields B_i are shown in Figs. 5.2(e) and (f) respectively. The values of λ_i and B_i extracted from the time domain fitting are consistent with those from the field domain fitting.

5.3 Solving the magnetic structure

5.3.1 Neutron powder diffraction

Neutron powder diffraction (NPD) measurements were performed on the WISH time-of-flight diffractometer [107] at ISIS, the UK Neutron and Muon Source. The single crystal sample was ground to a fine powder and loaded into a cylindrical vanadium can, which was mounted within a ^{4}He cryostat. Data were collected at 1.5 K and at

immediate vicinity of T_{N}.

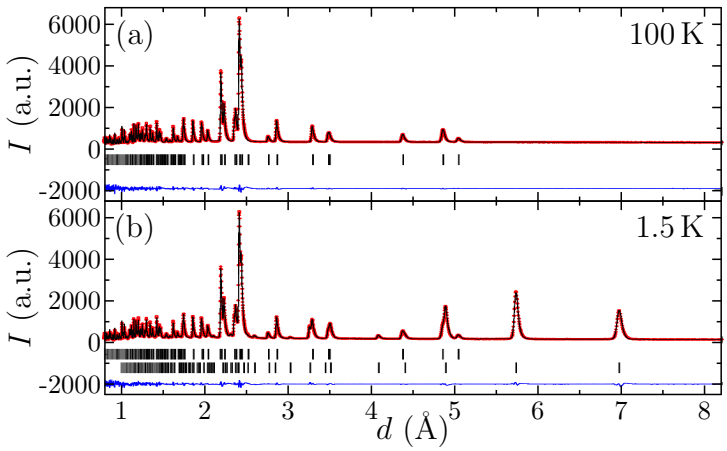

Figure 5.3: Neutron powder diffraction data (red points) measured in bank 2 (average diffraction angle $2\theta = 58.3°$) of the WISH diffractometer from $CoTi_2O_5$ in (a) the paramagnetic phase and (b) the antiferromagnetic phase. The solid black lines are fits to (a) the *Cmcm* nuclear model, and (b) the nuclear and magnetic model. The respective peak positions are shown as black tick marks (nuclear top, magnetic bottom). Difference patterns ($I_{\text{obs}} - I_{\text{calc}}$) are given as solid blue lines at the bottom of the panes.

100 K, in the long range ordered and paramagnetic phases respectively. All diffraction data were refined using FULLPROF [108].

NPD data collected at 100 K were fitted with a nuclear model based on the published crystal structure [100]. The goodness-of-fit was excellent, and the data and fit are shown in Fig. 5.3(a), with the refined structural parameters are given in Ref. 80. There was no evidence of impurity phases in these data. There is a small amount of site mixing whereby 2.8% of Co sites are occupied by Ti, and 1.4% of Ti sites are occupied by Co.

When compared to the NPD pattern at 100 K, data collected at 1.5 K showed more than 10 new diffraction peaks [Fig. 5.3(b)]. Based on the magnetometry and heat capacity measurements, as well as the results of our ZF-μSR experiments, the new intensities at low temperature very likely arise due to long range magnetic order. As there are a large number of new peaks, we can unambiguously determine the magnetic propagation vector: $\mathbf{k}_1 = (\frac{1}{2}, \frac{1}{2}, 0)$, or $\mathbf{k}_2 = (-\frac{1}{2}, \frac{1}{2}, 0)$, or both.[2] Note that

[2]The propagation vector $\mathbf{k} = (k_1, k_2, k_3)$ describes the periodicity of the magnetic structure with

these two vectors are distinct, meaning they are not related by an allowed reciprocal lattice vector of the parent structure, but they cannot be differentiated by NPD.

5.3.2 Symmetry analysis

Symmetry analysis, taking the *Cmcm* crystal structure of $CoTi_2O_5$ [100] as the parent, was performed using the ISOTROPY Suite [109, 110]. Out of the four irreducible representations of the reducible magnetic representation of $\mathbf{k}_1$ and $\mathbf{k}_2$, only one irreducible representation, mS_2^-, was able to reproduce the relative intensities of the magnetic diffraction peaks in Fig. 5.3(b) [we assume that the magnetic structure is described by a single irreducible representation]. In this discussion, we make reference to four symmetry-equivalent Co crystallographic sites, defined with respect to the *Cmcm* unit cell: Co1: $[0, y, \frac{1}{4}]$; Co2: $[\frac{1}{2}, \frac{1}{2} - y, \frac{3}{4}]$; Co3: $[\frac{1}{2}, \frac{1}{2} + y, \frac{1}{4}]$; Co4: $[0, 1 - y, \frac{3}{4}]$, where $y = 0.1911(6)$ at 100 K.

The irreducible representation mS_2^- is 2D, and therefore the magnetic order parameter can take one of three distinct directions: (η, η), $(\eta, 0)$, or (η, ϵ). In all three cases, the respective magnetic structures involve moments oriented parallel to the orthorhombic c axis. As all of the Co ions in the lattice are structurally equivalent, and therefore have the same chemical environment, all of the moments on these ions are constrained to be equal in magnitude. The only order parameter direction consistent with this constraint is $(\eta, 0)$.

$(\eta, 0)$ corresponds to a magnetic structure where magnetic moments on the Co1, Co2 and Co4 sites are parallel, but with the moment on the Co3 sites aligned antiparallel. A second domain exists with order parameter $(0, \eta)$, in which Co1, Co3, and Co4 sites are aligned parallel to each other, with Co2 antiparallel. The $(\eta, 0)$ and $(0, \eta)$ magnetic domains are interchanged by the symmetry operator $\{m_x|0, 0, 0\}$,

respect to the periodicity of the crystal structure. $k_i = \frac{1}{2}$ indicates antiferromagnetic order along the ith real-space axis (i.e. the periodicity of the magnetic structure is double that of the crystal) and $k_i = 0$ represents ferromagnetic order along that axis. Therefore $\mathbf{k} = (\pm\frac{1}{2}, \frac{1}{2}, 0)$ describes a structure which is antiferromagnetic along **a** and **b** and ferromagnetic along **c**.

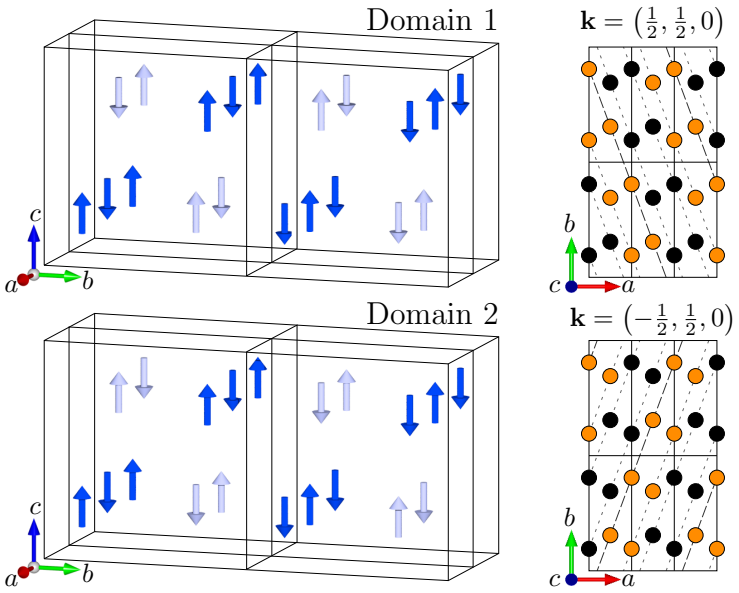

Figure 5.4: The magnetic structure of $CoTi_2O_5$. In the left hand panes four *Cmcm* unit cells are drawn, which represent a full repeating unit of the magnetic structure. Co1 and Co4 moments, drawn as dark blue arrows, are related to the Co2 and Co3 moments, drawn as light blue arrows, by C-centring. The diagrams on the right hand side illustrate the two propagation vectors associated with the two domains, where antiparallel moments are drawn as orange and black circles. Planes of parallel moments are denoted by faint dotted grey lines, and the periodicity of the magnetic structure is highlighted by the bold dashed grey lines.

which is broken below the magnetic phase transition.[3] The magnetic structure therefore reduces the symmetry of the system to monoclinic. Furthermore, the $(\eta, 0)$ and $(0, \eta)$ domains are described by $\mathbf{k}_1$ and $\mathbf{k}_2$, respectively, which are also related by m_x. The two domains are shown in Fig. 5.4, with the schematic in the right hand panes illustrating the two propagation vector directions. The magnitude of the Co moment was refined against the diffraction data and found to be $2.72(1)\,\mu_B$ at 1.5 K [see Fig. 5.3(b)]. We also note that, as the order parameter is $(\eta, 0)$, η can be taken to be equal to the Co moment. We can therefore directly observe the suppression of the magnetic order parameter by inspecting the temperature evolution of the internal fields at the muon site [Figs. 5.2(c) and (f)].

[3] This can be deduced by inspecting the transformation of the magnetic order parameter under the mS_2^- matrices.

5.4 Structural distortions and the spin Jahn-Teller effect

5.4.1 Symmetry considerations

The only nearest neighbour, super-exchange interactions between cobalt atoms (Co–O–Co) connect magnetic moments along the a-axis in Coi–Coi chains. All other nearest-neighbour interactions are mediated by super-super-exchange (Co–O–O–Co). We can assume that the super-exchange interactions are dominant and, by the experimentally determined magnetic structure, antiferromagnetic. All exchange interactions between the (Co1,Co4) and (Co2,Co3) sites, coloured dark and light blue in Fig. 5.4 respectively, are exactly frustrated by the m_x symmetry element. This frustration will likely lead to one dimensional ordering of the a-axis chains above T_{N}, but below the mean field energy of the dominant super-exchange interaction, consistent with the missing entropy evidenced in the heat capacity. For long range order to develop in $CoTi_2O_5$, the m_x mirror symmetry must be broken either at a structural phase transition above T_{N}, or through the spin Jahn-Teller effect, where the primary magnetic order parameter couples to a secondary, symmetry breaking structural order parameter spontaneously at T_{N} [82, 83]. We have no evidence for a higher temperature phase transition, and therefore we must examine possible magnetostructural coupling schemes.

The free energy invariant associated with the phase transition at T_{N} must be invariant by translation. Although the sign of the magnetic moments changes as we move from one unit cell to the next, the squares of the moments is unchanged. Therefore η^2 and ϵ^2 must couple to a $\mathbf{k}_{\mathrm{s}} = (0, 0, 0)$, Γ-point structural distortion in order to satisfy translational invariance. Through exhaustive searches performed using the ISOTROPY suite [109, 110], the lowest order invariant that can couple a

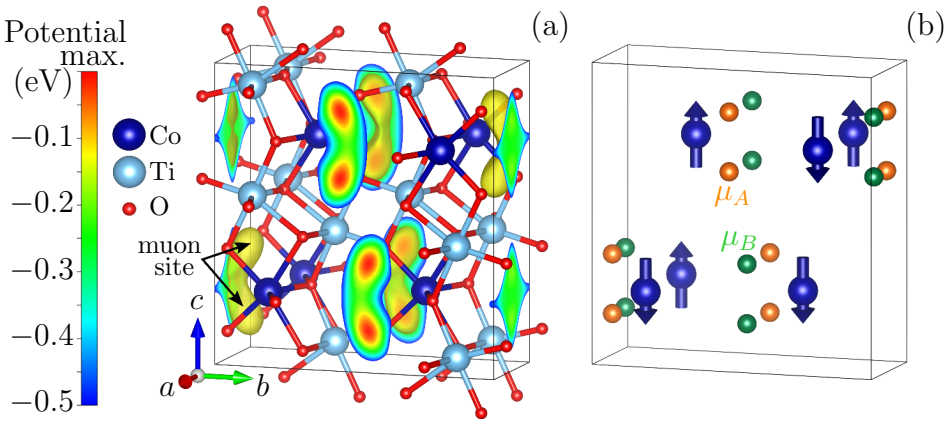

Figure 5.5: (a) Electrostatic Coulomb potential of $CoTi_2O_5$ computed with DFT. The potential is shown on the surface of the unit cell up to 0.5 eV below its maximum value, and a yellow isosurface is plotted within the unit cell at 0.25 eV below the maximum. (b) Muon positions inside $CoTi_2O_5$, with the two symmetry inequivalent groups μ_A and μ_B marked in orange and green respectively. The spin structure of domain 1 is shown on the Co ions.

non-trivial Γ-point structural distortion to the magnetic order is

$$\delta\left(\eta^2 - \epsilon^2\right), \tag{5.3}$$

where the irreducible representation of the structural order parameter δ is Γ_2^+. This distortion represents either a monoclinic shear in the unit cell, corresponding to $\gamma \neq 90°$, or a series of atomic displacements. There is also a trivial coupling invariant $\xi\left(\eta^2 + \epsilon^2\right)$ where the structural order parameter ξ transforms according to the totally symmetric Γ_1^+ irreducible representation. This case indicates that structural distortions that were already allowed within the *Cmcm* parent symmetry (*i.e.* strains parallel to the unit cell axes) can also occur at T_N.

High resolution laboratory based x-ray powder diffraction experiments yielded no evidence of the distortions associated with Eq. 5.3 below T_N. We therefore assume that any structural distortion in $CoTi_2O_5$ will be small, and the following calculations utilise the undistorted unit cell.

5.4.2 DFT and DFCs

In order to establish the potential muon stopping sites in $CoTi_2O_5$, we used DFT calculations (see Sec. 3.1) to map out the electrostatic Coulomb potential of $CoTi_2O_5$ throughout its unit cell, plotted using the VESTA software [111] in Fig 5.5(a). We also carried out relaxation calculations. These gave a single symmetry-inequivalent muon stopping site at $[0.322, 0.03, 0.151]$ in the unit cell, with a 1.0 Å O–H-like bond with the nearest oxygen.

There are 16 symmetry equivalent muon sites in the $Cmcm$ parent structure, which are split into two groups of eight in the magnetic unit cell, related by the broken m_x symmetry, and are denoted by μ_A and μ_B in Fig. 5.5(b). The muon stopping probability is dependent upon the electrostatic potential local to the stopping sites. Under a small structural distortion induced at the phase transition, μ_A and μ_B become structurally inequivalent, and are therefore associated with different muon stopping probabilities. Changing from one magnetic domain to another swaps the stopping probabilities of the two subgroups.

Using the muon stopping site and magnetic structure determined above, we calculated the expected dipolar field at the muon site resulting from the Co ions using Eq. 3.1 (see Sec. 3.1). The symmetry of the magnetic structure dictates that μ_A and μ_B will have different local magnetic fields: we calculate these to be 335(1) mT and 277(1) mT, in excellent agreement with our experimental observations at low temperature. As the area under the higher-field peak in Fig. 5.1(d) is larger than that of the lower-field peak, this suggests that the muon site experiencing the higher field is preferentially occupied. By comparing the energies at the muon sites under small distortions we can propose a possible coupling between a shear distortion and the magnetic domains.

The distortion associated with the invariant in Eq. 5.3 causes a monoclinic shear in the unit cell with the c-axis unique, or a series of atomic displacements. The

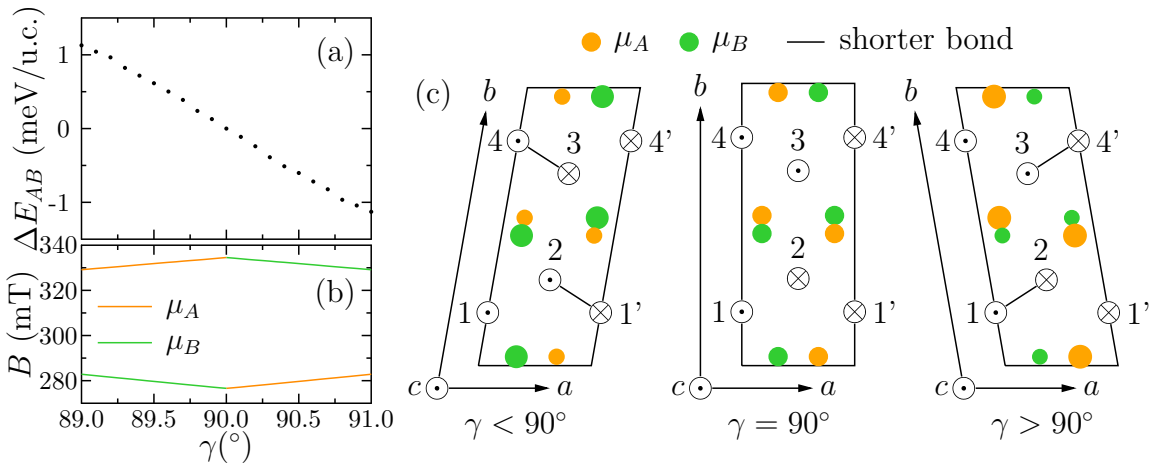

Figure 5.6: (a) The γ dependence of the difference in energy between the two structurally inequivalent sites $\Delta E_{AB} = E_{\mu_A} - E_{\mu_B}$. E_{μ_i} is the DFT-calculated energy of the relaxed unit cell with the μ_i site occupied by a muon. (b) The domain structure at shearing angles above and below $\gamma = 90°$ as predicted by the μSR data in the main text. The muon sites μ_i are also plotted, where the larger circles indicate muon sites that are energetically favourable.

shear manifests in a perturbation of γ, the angle between the **a** and **b** directions. This perturbation can either result in an increase or decrease of γ, dependent on the domain. In the absence of the monoclinic distortion, $\gamma = 90°$ and both muon sites are structurally equivalent (although they are magnetically inequivalent). If $\gamma \neq 90°$, the two sites μ_A and μ_B become structurally inequivalent, and their ground state energies differ. The difference between the ground state energies $\Delta E_{AB} = E_{\mu_A} - E_{\mu_B}$, where E_{μ_i} is the ground state energy of the unit cell containing a muon in site μ_i, is plotted in Fig. 5.6(a). When $\Delta E_{AB} < 0$, muons preferably occupy μ_A, whereas if $\Delta E_{AB} > 0$, muons preferably occupy μ_B. By simulating the local dipolar field at the muon site for $\gamma \neq 90°$ [Fig. 5.6(b)], we find a possible correspondence between γ and the domain, presented in Fig. 5.6(c). In this configuration, the high-field site is always energetically favorable.

Finally we consider the additional feature marked by an asterisk in Fig. 5.1(d) at $\approx 400\,\mathrm{mT}$. This feature likely arises due to a Co ion occupying the nearest Ti site so that a small fraction of muons stopping close to this defect experience a slightly

larger field. Indeed, modelling this disorder gives a field at the muon site of $\approx 410\,\mathrm{mT}$, consistent with the experimental value.

5.4.3 First order or second order?

Our proposed magnetostructural coupling may affect the order of the phase transition. The transition from paramagnetism to antiferromagnetism is often second order, but coupling to a structural distortion may push the transition to first order [112]. The rapid suppression of the magnetic order parameter in Figs. 5.2(c) and (f) appears to support this notion. Heat capacity measurements taken in steps of 0.1 K around T_N on cooling did not result in an observable shift in T_N compared to those taken on warming (hysteresis would be expected for a first order transition). It is, however, still possible that there is a shift in T_N smaller than the resolution of our experiment.

5.5 Conclusion

To conclude, we have identified long range magnetic order in $CoTi_2O_5$, which is antiferromagnetic with $\mathbf{k} = (\pm\frac{1}{2}, \frac{1}{2}, 0)$. Frustration in the super-super-exchange interactions, along with the absence of a structural distortion above $T_\mathrm{N} \approx 26\,\mathrm{K}$, indicate that the magnetic transition must be coupled to a structural transition at T_N in order to relieve the frustration. This coupling occurs due to the spin Jahn-Teller effect, which has so far only been identified in higher-symmetry crystal structures [82, 83, 84, 85]. Our results show that magnetic order driven by spin-phonon coupling can be extended to lower-symmetry systems. While the predicted distortion in $CoTi_2O_5$ was not resolvable in high resolution laboratory based x-ray powder diffraction experiments, it may be possible to resolve using higher-resolution synchrotron x-ray powder diffraction experiments. The study of compounds structurally related to $CoTi_2O_5$ may provide further insight into the conditions required for the spin Jahn-Teller effect to, or not to, occur.

6

Introduction to superconductivity

High temperature superconductivity is a phenomenon rich in industrial applications, yet still shrouded by uncertainty as to its underlying mechanisms. Below a critical temperature T_c, the electrons in a superconductor form Cooper pairs which can scatter off one another without the dissipation of energy. This results in zero resistivity below T_c and several interesting field-induced effects. The discovery of superconductivity took place in Leiden by Kammerlingh Onnes [113], and the discovery of many similar, conventional, superconductors followed, along with a theory to describe them [114]. This was all thrown out of the water when, in 1986, Bednorz and Müller discovered the first high temperature superconductor ($Ba_xLa_{5-x}Cu_5O_{5(3-y)}$ with a T_c of 35 K), opening up a wealth of research on the cuprates [115]. A couple of decades later, two new classes of high temperature superconductors were discovered: the iron pnictides and chalcogenides [116, 117]. The current record for highest T_c is held by hydrogen

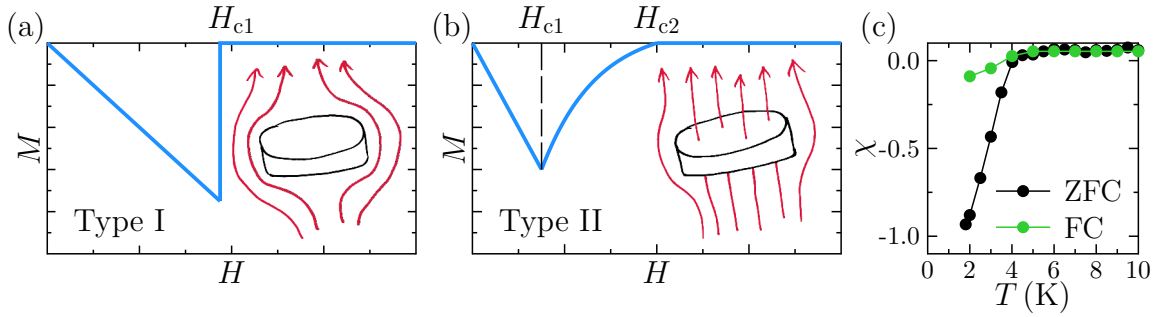

Figure 6.1: (a) The field dependence of the magnetisation for a type I superconductor. The inset shows the magnetic field lines around a type I superconductor in the Meissner state. (b) The field dependence of the magnetisation for a type II superconductor. The inset shows the magnetic field lines penetrating the superconductor in the vortex state. (c) The field-cooled (FC) and zero-field-cooled (ZFC) dimensionless susceptibility of FeS in an applied field of 5 mT.

sulphide[1] under high pressure; here $T_c \approx 203\,\mathrm{K}$ [118].

This chapter gives an introduction to superconductivity. The BCS and Ginzburg-Landau theories, and their key results, are presented, with a focus on the parameters that can be measured using μSR experiments.

6.1 Type I and type II

There are two main types of superconductivity, (imaginatively) named types I and II. The key difference between these two types is their behaviour in an external magnetic field. Type I superconductors fully expel the field below T_c and up to some critical applied field H_{c1} (this phenomenon is the Meissner state). As the field is totally expelled, the magnetisation of the sample is proportional to the applied field; this relationship has been plotted in Fig. 6.1(a). Type II superconductors also exhibit the Meissner state up to some H_{c1}, and then above H_{c1} (but below a second critical field H_{c2}) quantised flux lines from the applied field are trapped in the

[1]Hydrogen sulphide normally takes the form of H_2S (the compound responsible for the smell of rotten eggs) under ambient pressure, but it is thought that H_3S, which is formed via the decomposition of H_2S under high pressure, is the compound responsible for the superconductivity [118].

sample, forming the flux line lattice (FLL). These flux lines, also known as Abrikosov vortices, are small pockets of the normal state surrounded by the superconductor; this state is therefore known as the mixed state. As the applied field increases, the density of vortices increase, until a critical flux density is reached at H_{c2}, and superconductivity is destroyed. A plot of the field dependence of the magnetisation of a type II superconductor is shown in Fig. 6.1(b).

The presence of superconductivity can be inferred by examining the dimensionless magnetic susceptibility $\chi = \lim_{H\to 0} M/H$. As a superconductor is perfectly diamagnetic in the Meissner state, we expect $M = -B/\mu_0$ and therefore $\chi = -1$. The susceptibility of FeS,[2] determined using SQUID magnetometry (see Chap. 2 for an introduction to this technique), is given in Fig. 6.1(c).

6.2 BCS theory

Bardeen–Cooper–Schrieffer (BCS) theory is a microscopic model of Cooper pairs which has been very successful in describing the properties of conventional superconductors [114]. This thesis concerns itself primarily with unconventional superconductors, but fortunately some aspects of BCS can be used to an extent to also describe unconventional properties.

In the superconducting ground state, Cooper pairs occupy the lowest energy level in a Bose-Einstein condensate. When heat is added into the system, some Cooper pairs gain enough thermal energy to cross the energy gap Δ and therefore break up and become normal-state conduction electrons. The pair-breaking mechanism, described by the topology and magnitude of the energy gap, is intricately linked to the microscopic details of the superconductor and can be altered in numerous ways,

[2] H_2S may be a precursor to another superconductor. When boiling an egg, H_2S is formed in the white, and then migrates towards the yolk (where T is lowest). It then reacts with Fe in the yolk, forming FeS ($T_c \approx 4\,K$ [119, 120]), and giving the characteristic green tinge to the yolks of over-boiled eggs. There are two possible crystalline structures for FeS (only one superconducts), so it remains an open question as to whether FeS synthesised *in ovo* is indeed a superconductor.

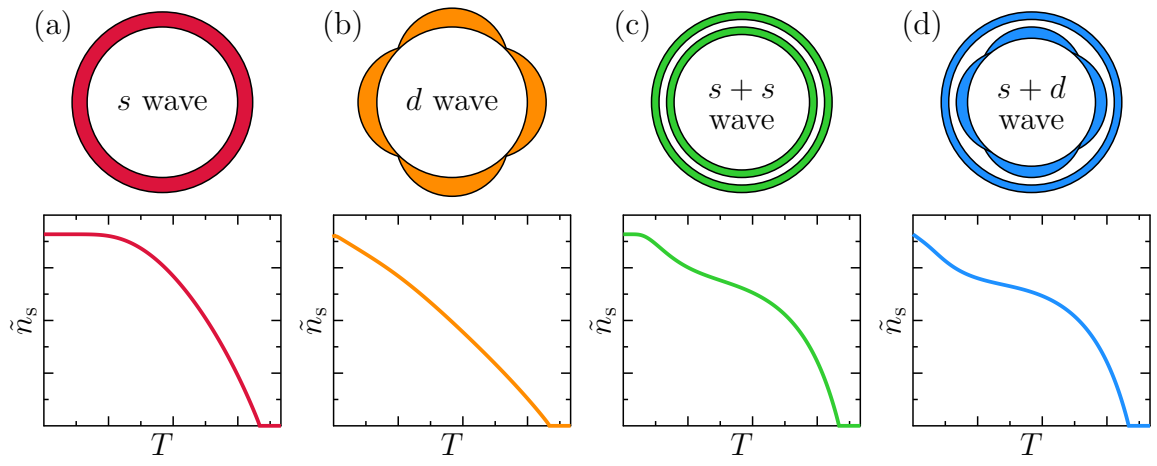

Figure 6.2: *Top:* A schematic of the superconducting gap symmetry and *bottom:* the T dependence of the superfluid density of (a) s-wave, (b) d-wave, (c) $s+s$-wave, and (d) $s+d$-wave superconductors.

for example using pressure [121] or chemical doping [122, 123]. Gap topologies broadly fall into two main categories: fully-gapped and nodal. Some examples of fully-gapped and nodal topologies are shown in Fig. 6.2. The temperature dependence of the gap can be described using the approximate form

$$\Delta(\phi, T) = \Delta(\phi) \tanh\left(1.82\left[1.018\{T_c/T - 1\}\right]^{0.51}\right), \tag{6.1}$$

where $\Delta(\phi) = \Delta_0$, a constant, for an s-wave (fully-gapped) superconductor, and $\Delta(\phi) = \Delta_0 \cos(2\phi)$ for a d-wave (nodal) superconductor.

While the cuprate superconductors have a universal pair-breaking mechanism and a nodal superconducting gap [124], the iron-based superconductors have been found to contain both gapped and nodal systems, with no clear universal pair-breaking mechanism.

Near the surface of a superconductor, an external magnetic field can penetrate a small volume, dropping off exponentially with the distance from the surface x

$$B(x) = B(0) \exp(-x/\lambda), \tag{6.2}$$

with a characteristic length scale λ: the London penetration depth. λ can be described in terms of the mass m, number density n_s and charge q of the Cooper pairs as

$\lambda = (m/\mu_0 n_s q)^{1/2}$. The superfluid density n_s is a measure of the number of Cooper pairs in the system, and so as T is increased, n_s is expected to drop and therefore λ increases as the external field can penetrate further into the sample.

The temperature evolution of the normalised superfluid density can be described as [125]

$$\tilde{n}_s(T) = \frac{n_s(T)}{n_s(0)} = \frac{\lambda^{-2}(T)}{\lambda^{-2}(0)} = 1 + \frac{1}{\pi}\int_0^{2\pi}\int_{\Delta(\phi,T)}^{\infty} \frac{\partial f}{\partial E}\frac{E\,\mathrm{d}E\,\mathrm{d}\phi}{\sqrt{E^2 - \Delta^2(\phi,T)}}, \tag{6.3}$$

where $\Delta(\phi, T)$ is the superconducting gap function described in Eq. 6.1 and f is the Fermi function:

$$f = \left[1 + \exp\left(E/k_B T\right)\right]^{-1}. \tag{6.4}$$

The temperature evolution of $\tilde{n}_s(T)$ for several gap topologies is given in Fig. 6.2. By examining the low temperature behaviour of $\tilde{n}_s(T)$, it becomes relatively straightforward to tell whether a gap is nodal or not. For a fully-gapped superconductor, the low temperature region has a plateau in the superfluid density. This is because Cooper pairs need to reach a certain temperature $T \sim \Delta_0/k_B$ in order to have sufficient thermal energy to cross the gap and break up. Nodal superconductors, on the other hand, exhibit a linear dependence of $\tilde{n}_s(T)$ at low temperatures. The absence of a gap in nodal systems means low-energy excitations are possible as there is always sufficient energy for some Cooper pairs to break up.

It is important to note that μSR experiments are not sensitive to the sign of the gap function;[3] a d-wave gap in Chapters 7 and 8 therefore simply refers to a gap with line nodes. As such, it is always possible that an observed d-wave $\tilde{n}_s(T)$ could in fact arise from a highly anisotropic s-wave gap where the characteristic plateau in $\tilde{n}_s(T)$ is only observable at very low temperatures.

BCS theory holds well for sufficiently weak electron interactions. By inspecting the ratio $\Delta_0/k_B T_c$ (which = 1.764 for weakly-coupled BCS superconductors), it is

[3]The sign of a gap can be deduced by examining the evolution of $\Delta(\phi)$ as one moves across the Fermi surface.

possible to determine whether the coupling in a superconductor is strong or weak. For strongly-coupled superconductors, $\Delta_0/k_\mathrm{B}T_\mathrm{c} > 1.764$.

6.3 Ginzburg-Landau theory

In 1950, Ginzburg and Landau introduced a thermodynamic theory of superconductivity [126], which was later shown by Gor'kov to be a mean-field form of BCS theory [127]. Although Ginzburg-Landau theory does not include the microscopic details contained within BCS theory, it does in fact describe many properties of superconductors, and in particular it can describe properties of unconventional superconductors where BCS theory fails to do so.

By inspecting the free energy of a superconductor near the superconducting transition, the Ginzburg-Landau (GL) equations can be derived; this derivation is given in Ref. 128. The GL equations describe the behaviour of the superconducting order parameter ψ. Through solving the GL equations in a magnetic field, Abrikosov discovered that the order parameter's spatial distribution meant that, in a type II superconductor in the mixed state, ψ forms into an ordered periodic structure of vortices [6]. Usually this structure consists of a hexagonal lattice, but several examples of a square lattice of vortices exist [129]. In this thesis, we concern ourselves only with the hexagonal lattice. The magnetic field and spatial distributions of a hexagonal vortex lattice have been plotted in Fig. 6.3(a) and (b) respectively.

A result that follows from the vortex lattice in the mixed state is that each vortex contains a single quantum of magnetic flux in its centre. When $T < T_\mathrm{c}$, a vortex can therefore be described by a temperature-dependent length scale $\xi(T) = \xi(0)\left(|T_\mathrm{c} - T|/T_\mathrm{c}\right)^{-1/2}$ which is related to the upper critical field via $\mu_0 H_{\mathrm{c}2} = \phi_0/2\pi\xi(T)^2$. By inspecting the phase transition between the Meissner and mixed states, the Ginzburg-Landau parameter $\kappa = \lambda/\xi$ can be used to differentiate between type I and II superconductors: for type I, $\kappa < 1/\sqrt{2}$, while for type II, $\kappa > 1/\sqrt{2}$.

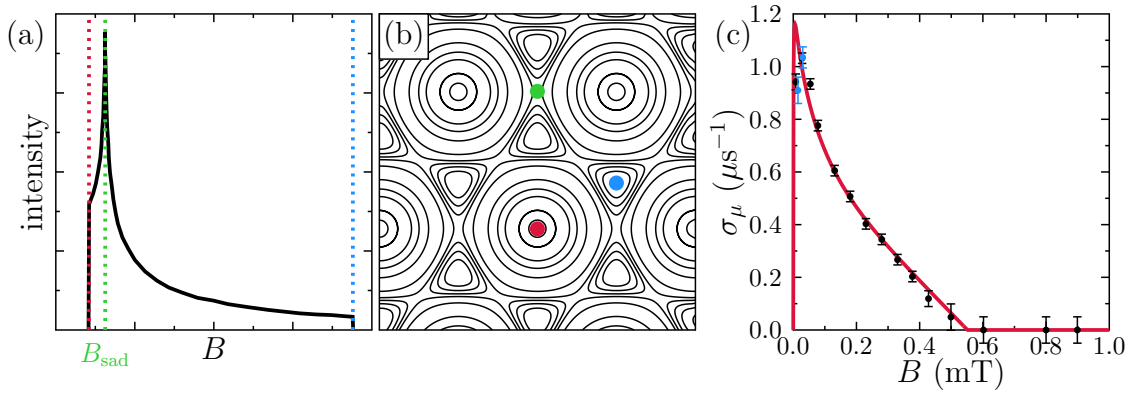

Figure 6.3: (a) The magnetic field distribution inside a hexagonal FLL in a type II superconductor. The minimum (red), maximum (blue), and saddle point (green; $B_{\rm sad}$) have been marked. (b) The spatial distribution of the magnetic field resulting from the hexagonal vortex lattice. The corresponding points with minimum, maximum, and saddle point fields have been marked in red, blue, and green respectively. (c) The field dependence of the width of the magnetic field (here given in μs^{-1}, where $\sigma_\mu = \gamma_\mu \sigma$, and σ is as defined in Eq. 6.6), for FeS. The blue points are from Ref. 120 and the black points from Ref. 130. The data have been fitted with Eq. 6.6.

In this thesis, properties of superconductors are calculated by measuring the standard deviation of the magnetic field distribution (plotted in Fig. 6.3(a)) of a FLL using μSR. This measurement is taken by cooling the sample below $T_{\rm c}$ in an applied field $B_{\rm c1} < B < B_{\rm c2}$. A full treatment of the vortex lattice in superconductors is given in Refs. 7, 131, and 132, with key results presented below.

The relationship between the magnetic field width (i.e the standard deviation), σ, and λ is dependent on κ and the applied field B. In μSR, the muons always land in a set of structurally equivalent sites inside the unit cell. However, as the distance between vortices a is often much larger than the lattice constants of the unit cell of the superconductor, muons implanted in the sample will be able to experience the full width of the distribution. The field distribution of a hexagonal FLL is plotted in Fig. 6.3(b). There are three key features of this distribution: $B_{\rm sad} = B(a/2, 0)$, the saddle point between to vortices; $B_{\rm max} = B(0, 0)$, the maximum field at each vortex core; and $B_{\rm min} = B(0, a/\sqrt{3})$, the minimum field between the vortices.[4] These three

[4]The coordinate system here is defined such that a vortex centre lies at (0,0) and the distance

Limit	Approximation
$\kappa \geq 70$; $0.13/\kappa^2 \ll b \ll 1$	$\sigma = 0.0609\phi_0/\lambda^2$ (London approximation)
$\kappa \geq 5$; small b [$b < 0.01/\kappa^2$ for $\kappa = 5$, $b < 0.04/\kappa^2$ for $\kappa \geq 10$]	$\sigma = \sqrt{b}\kappa\phi_0/2\sqrt{2}\pi\lambda^2$
$\kappa \geq 5; 0.25/\kappa^{1.3} \leq b \leq 1$	$\sigma = 0.172\,(B_{c2} - B)\,\kappa^{-2}\left[1 + 1.21\left(1 - \sqrt{b}\right)^3\right]$

Table 6.1: Several approximations for the width of the magnetic field distribution of the FLL (Eq. 6.6). These expressions are derived in Ref. 132.

points have been marked in Fig. 6.3(b). The field distribution due to the FLL can be approximated to be Gaussian, and therefore the peak of the Gaussian approximately corresponds to B_{sad}, where

$$B_{\text{sad}} = B - 0.146 B_{c2} \frac{1-b}{\kappa^2 - 0.069} \tag{6.5}$$

and $b = B/B_{c2}$ [132]. As the applied field only penetrates the superconductor in the vortices themselves, the peak field is always lower than the applied field.

The variance of the magnetic field inside a superconductor is

$$\sigma^2 = \langle [B\,(x,y) - B]^2 \rangle = \langle \left[B\,(x,y)^2 - B^2\right] \rangle = \sum_{\mathbf{k} \neq 0} B_{\mathbf{k}}^2, \tag{6.6}$$

where $B_{\mathbf{k}}$ are the Fourier coefficients of the field distribution $B(x,y)$, and $\mathbf{k}$ are the reciprocal lattice vectors [132]. In suitable limits, approximations can be applied to this formula such that λ can be extracted. The relationship between σ and $b = B/B_{c2}$ for FeS is plotted in Fig. 6.3(c), and approximations to Eq. 6.6 in the low- and high-field limits are given in Table 6.3 (a derivation of these approximations is given in Ref. 132).

between neighbouring vortices is a.

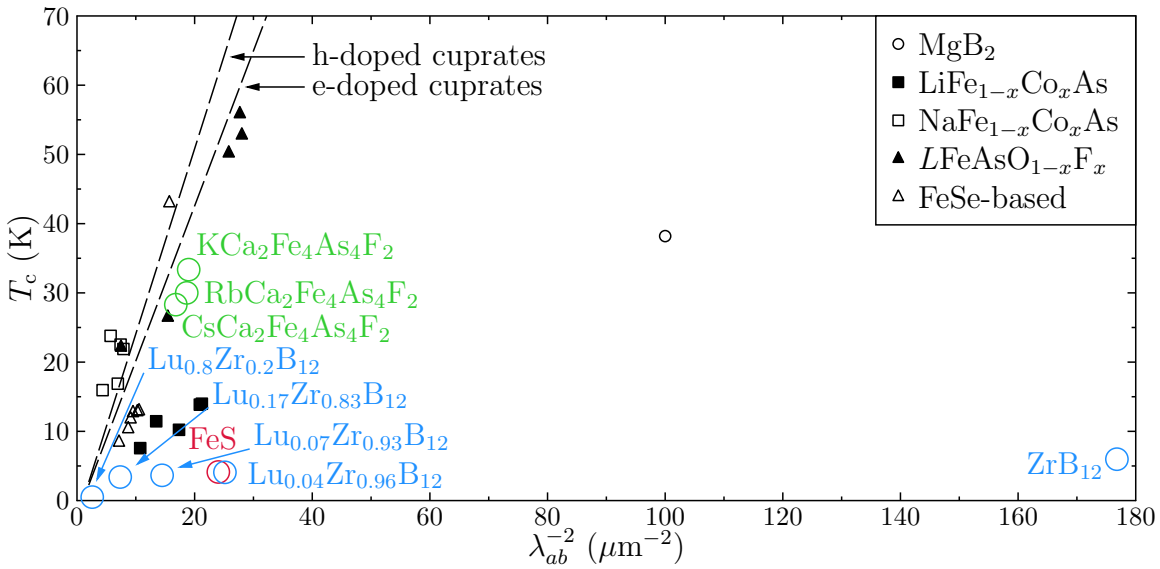

Figure 6.4: A Uemura plot displaying several well-studied families of superconductors, along with the superconductors investigated in this thesis. The two dashed lines represent fits to the λ_{ab}–T_c relationship for the electron- and hole-doped cuprates. Note that, as the $Lu_xZr_{1-x}B_{12}$ family is isotropic, the penetration depth $\lambda = \lambda_{ab}$.

Many interesting superconductors are anisotropic: the cuprates and iron-based superconductors both consist of planes of atoms, and the manipulation of these planes through pressure [133], chemical doping [134], and thin film growth [135] can have drastic effects on the properties of the superconductor. In anisotropic superconductors, λ is also anisotropic. In practice, it is most useful to calculate the in-plane penetration depth λ_{ab}, which for many anisotropic superconductors is $\ll \lambda_c$, the out of plane penetration depth. This is because $\lambda_i \propto \sqrt{m_i}$, the component of the effective mass tensor in direction i. μSR measures the effective penetration depth, which is related to λ_{ab} via [136]

$$\lambda_{\text{eff}} = 3^{1/4}\lambda_{ab}. \tag{6.7}$$

It is useful to inspect the evolution of T_c and λ_{ab} for different families of superconductors, in order to spot inter- and intra-family trends. The Uemura plot shows such correlations, and was initially designed to map the universal relations underlying the cuprate superconductors [137]. Through examination of the often linear

scaling behaviour between T_c and λ_{ab}, it is possible to identify different classes of superconductors. For example, the electron- and hole-doped cuprates both display a linear scaling, but the gradient for the hole-doped materials is much larger. Recently, the Uemura plot has been extended to show many families of high temperature superconductors, and an example is presented in Fig. 6.4.

6.4 Conclusion

This chapter presents an introduction to superconductivity, with a focus on the physical properties of superconductors that can be measured using μSR. While the key results of the BCS and Ginzburg-Landau theories are presented, many extensions to these results exist, and therefore μSR often only provides us with a minimal model. Further information on the superconducting ground state can be gleaned from using complementary experimental techniques. Examples of such techniques include ARPES, which can be used to determine the Fermi surface and superconducting gap [138, 139], and neutron scattering, which can measure spin fluctuations and phonon spectra[5] [141].

[5]While the coupling between phonons and Cooper pairs is a result of BCS theory, several promising theories of high-temperature superconductivity involve spin fluctuation-mediated Cooper pairing [140].

7

Nodal multigap superconductivity in ACa$_2$Fe$_4$As$_4$F$_2$ (A=K, Rb, and Cs)

In order to understand the underlying mechanisms of high-temperature superconductors, it is vital to study the methods by which one can manipulate their superconducting properties. In this chapter, I present an experimental study of the ACa$_2$Fe$_4$As$_4$F$_2$ (A = K, Rb, and Cs) family of iron pnictide superconductors. These compounds are related to the fully-gapped superconductors ACaFe$_4$As$_4$, but here the Ca-containing spacer layer is replaced with one containing Ca$_2$F$_2$. I show that the ACa$_2$Fe$_4$As$_4$F$_2$ compounds are nodal multigap superconductors, paving a new path from nodal to gapped superconductivity. The work in this chapter is based on Refs. 142, 143, and 144.

Aidy Hillier, Peter Baker, Franz Lang, Michael Smidman, and Adroja assisted with running the experiment. Stephen Blundell helped with the theoretical interpretation

of results. All samples in this chapter were synthesised by Zhi-Cheng Wang and Guang-Han Cao, who also carried out the SQUID measurements.

7.1 Introduction

Unlike the cuprate high temperature superconductors [145], the iron-based superconductors do not appear to have a universal superconducting gap structure: it has been found to vary between families of compounds, as well as within a single family through doping [122] or pressure [121]. The first iron arsenide superconductor family is a prime example: $LaFeAsO_{1-x}F_x$, with a maximum critical temperature $T_c = 26\,K$ [117], is thought to have either extended s-wave pairing [146] with a reversal of the sign of the order parameter between Fermi surfaces [147], or d-wave pairing with line nodes [146, 148, 149]. The need for a universal picture of gap structures is vital to understand the mechanism with which Cooper pairs are formed in the iron-based superconductors.

The gap structure has been found to vary between members of a single FeAs family. $Ba_{1-x}K_xFe_2As_2$, part of the 122 family,[1] was initially found to have two s-wave gaps [150, 151]. Subsequent studies, however, found evidence that KFe_2As_2, which is in the strong hole doping regime in this family, exhibits d-wave nodal superconductivity [122, 124, 152, 153] which may arise from antiferromagnetic spin fluctuations near the quantum critical point [154]. It has also been suggested that KFe_2As_2 has a Fermi surface-selective multigap structure, resulting in s-wave superconductivity with accidental line nodes [155]. The replacement of K with Rb or Cs has been reported to conserve the nodal gap structure [156, 157, 158], although there have also been studies to suggest these compounds are $s + s$-wave [159, 160].

There have been several attempts to account for this variation in gap symmetry amongst the iron arsenides. Ref. 161 suggests that, away from optimal doping,

[1] Superconductors can be grouped into families of compounds with related crystal structures. The nomenclature reflects the numbers of each atom in the chemical formula.

subdominant interactions (for example Coulomb interactions) and pair scattering between electron-like Fermi surface sheets increase and frustrate the isotropic $s\pm$ gap, leading to anisotropy and eventually nodes, as evidenced in the 122 family. It has also been theorised that this frustration in FeAs superconductors may lead to time-reversal symmetry breaking (TRSB) and, as a result, an $s + id$ pairing [162]. Maiti *et al.* [163] propose a mechanism based on spin-fluctuation exchange, similar to Ref. 161. In Ref. 163, the variation between family members is explained through the degree of electron or hole doping in the compound: small to moderate dopings have an s-wave pairing driven by the interpocket electron-hole interaction, strong electron dopings have a d-wave pairing from the attraction between electron pockets, and strong hole dopings have either a d-wave pairing from attraction within one of the hole pockets or an s-wave pairing from the interaction of hole pockets at (0,0). Another cause of the varying gap symmetries may be the height of the pnictogen atom, which alters the competition or cooperation of the spin fluctuation modes [146].

No such drastic variation is seen in the 1144 family (ACaFe$_4$As$_4$, $A =$ K, Rb, or Cs [164]), with evidence for multigap s-wave superconductivity and a clear absence of nodes in both experimental and theoretical studies [165, 166, 167, 168, 169, 170]. Interestingly, this family has a maximum $T_\mathrm{c} = 35\,\mathrm{K}$ for $A =$ Rb, the alkali atom with intermediate size. This contrasts with 1111-type FeAs superconductors [117, 171, 172], as well as other alkali metal arsenide superconductors, such as the chain-based compounds A_2Cr$_3$As$_3$ ($A =$ K, Rb, or Cs), where increasing the ionic radius of A leads to a chemical pressure-induced suppression of T_c [158, 173, 174].

Another example of a FeAs family with an inverse correlation between T_c and alkali metal atomic radius is the 12442 family. The first ACa$_2$Fe$_4$As$_4$F$_2$ compound to be discovered was $A =$ K ($T_\mathrm{c} = 33\,\mathrm{K}$) [175], and subsequently $A =$ Rb, Cs ($T_\mathrm{c} = 31\,\mathrm{K}$ and $28\,\mathrm{K}$ respectively) [176] were also synthesised. This family can be viewed as an intergrowth of AFe$_2$As$_2$ and CaFeAsF layers (see Fig. 7.1). Double FeAs layers

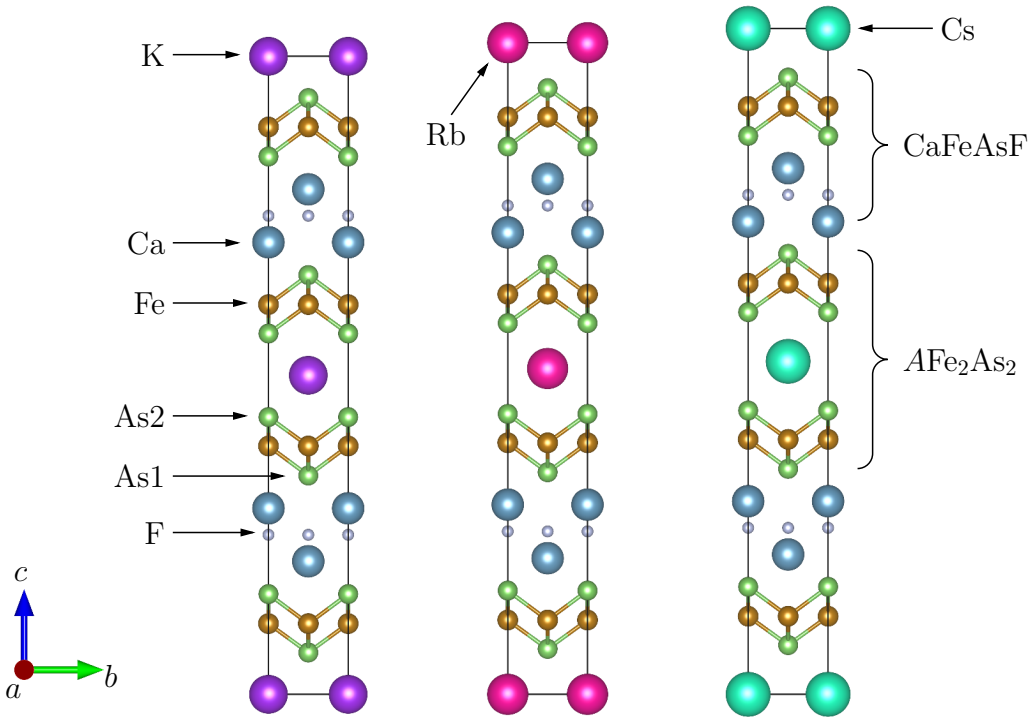

Figure 7.1: The unit cells of ACa$_2$Fe$_4$As$_4$F$_2$ for *left:* A = K, *centre:* A = Rb, and *right:* A = Cs. The CaFeAsF and AFe$_2$As$_2$ subunits have been marked for A = Cs.

are sandwiched between A atoms on one side and Ca$_2$F$_2$ on the other, leading to two distinct As sites. These compounds are self-hole-doped, in contrast to other hole-doped FeAs superconductors [177, 178]. It has been suggested that the complex nature of the electronic structure of these materials could lead to a multiband gap structure [179].

7.2 Experimental details

Polycrystalline samples of ACa$_2$Fe$_4$As$_4$F$_2$ (A = K, Rb, and Cs) were synthesised via the solid state reaction in Ref. 175, and were found to have a sharp superconducting transitions (see Fig. 7.2). The A = Rb and Cs samples in this work were found to have a higher superconducting volume fraction than that for A = K, indicating that these samples have a higher purity.

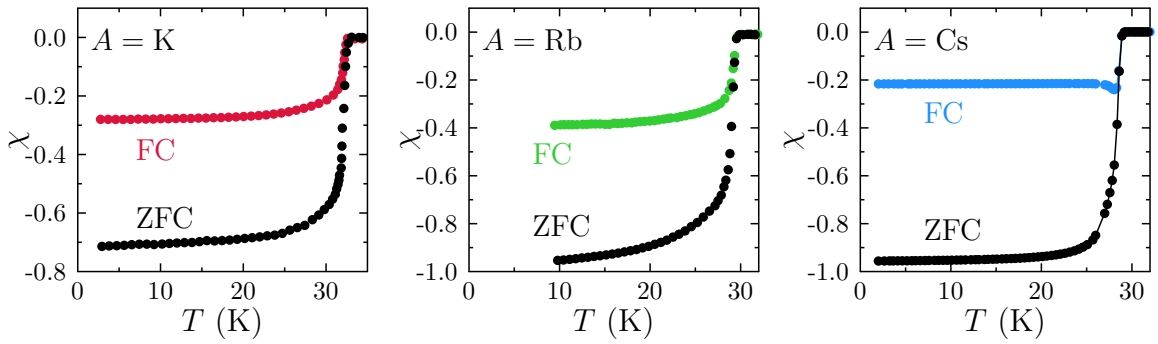

Figure 7.2: The field-cooled (FC) and zero-field-cooled (ZFC) dimensionless susceptibilities ($\chi = M/H$, where M is the sample's magnetisation) of $A Ca_2Fe_4As_4F_2$ for A =K, Rb, and Cs, measured in an applied magnetic field of $\mu_0 H = 1\,\mathrm{mT}$.

μSR experiments [4, 105] were performed using a ^{3}He cryostat mounted on the MuSR spectrometer at the ISIS pulsed muon facility (Rutherford Appleton Laboratory, UK) [9]. Zero-field (ZF) measurements were carried out to check for magnetism, TRSB across the superconducting transition, and to see if an FμF state (in which the muon forms a hydrogen bond with fluorine atoms in the sample [180, 181]) exists.[2] Transverse-field (TF) measurements were performed to identify the superconducting ground state. All of the data were analysed using WiMDA [106].

7.3 Superconductivity

Transverse field measurements were performed in an applied field $B_{\mathrm{app}} = 40\,\mathrm{mT}$ in order to probe the superconducting ground state. Representative spectra for A = Cs above and below T_c are shown in Fig. 7.3(a). There is a clear increase of the relaxation in the superconducting state (compared to the normal state) which arises from the inhomogeneous field distribution of the vortex lattice [131]. All TF-μSR spectra were fitted with the two-component function

$$A(t) = A_B \cos\left(\gamma_\mu B_{\mathrm{app}} t + \phi\right) + A_{\mathrm{SC}} \cos\left(\gamma_\mu B_{\mathrm{SC}} t + \phi\right) e^{-\frac{\sigma^2 t^2}{2}}, \tag{7.1}$$

[2]The presence of an FμF state is useful for identifying the muon site in the unit cell.

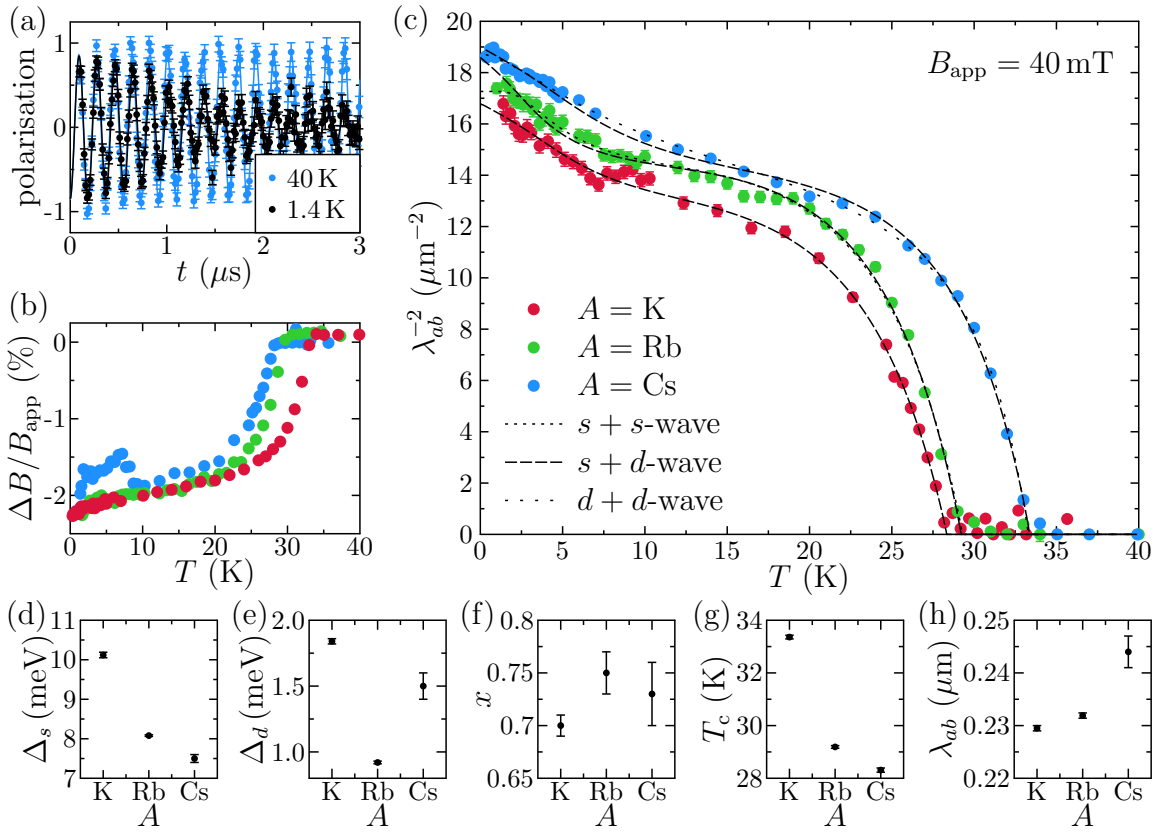

Figure 7.3: (a) Normalised TF-μSR asymmetry for A = Cs above and below $T_{\rm c}$. (b) The shift in the magnetic field $\Delta B = B_{\rm SC} - B_{\rm app}$ due to the superconducting vortex lattice in an applied field of 40 mT. (c) The temperature dependence of the inverse square penetration depth in the $a-b$ plane. Best fits to Eq. 6.3 for each compound are also shown. The bottom panel shows the A dependences of (d) the s-wave gap, (e) the d-wave gap, (f) the weighting factor, (g) the critical temperature, and (h) the penetration depth in the $a-b$ plane, extracted using fits to (c) with an $s+d$-wave model.

where ϕ is a phase related to the detector geometry; ϕ was fitted for each of the eight detector groups of the spectrometer. The first term represents those muons which are not implanted into the superconducting volume and precess only in the external magnetic field, and so do not experience any relaxation. This component also includes muons implanted in the sample holder and cryostat. The second term arises from muons in the superconducting volume, which experience a Gaussian broadening $\sigma(T) = \sqrt{\sigma_{\rm SC}^2(T) + \sigma_{\rm nucl}^2}$ consisting of a temperature-dependent component from the vortex lattice, and a temperature-independent component from nuclear moments. By

	$s+s$-wave	$s+d$-wave	$d+d$-wave
K	10.5	**6.0**	**6.2**
Rb	**3.0**	**3.1**	6.2
Cs	10.9	**7.7**	11.0

Table 7.1: The values of χ^2 for the best fits to various single and multigap models for all A. The values in bold indicate the best fitting models.

fitting the residual, temperature-independent component of σ, we find $\sigma_{\rm nucl} \approx 0.1\mu{\rm s}^{-1}$ for all of the samples.

The field shifts caused by the vortex lattice $\Delta B = B_{\rm SC} - B_{\rm app}$ are shown in Fig. 7.3(b). There is a clear negative shift in the peak field as the samples transition into their superconducting states. Interestingly, there is a small peak in the field shift at $T \approx 8\,{\rm K}$ for $A = {\rm Cs}$, which may be linked to a magnetic phase in the sample that will be discussed below.

In order to extract the penetration depth from $\sigma_{\rm SC}$, the conversion [132]

$$\sigma_{\rm SC} = 0.0609\gamma_\mu\phi_0\lambda_{\rm eff}^{-2}(T) \tag{7.2}$$

can be used. This conversion holds as B_{c2} is expected to be $> 30\,{\rm T}$ for all A [175, 176]. As the sample is anisotropic [175, 176] and polycrystalline, it can therefore be assumed that the effective penetration depth $\lambda_{\rm eff}$ is dominated by the in-plane penetration depth λ_{ab} (a discussion of this is given in Sec. 6.3). The temperature dependence of λ_{ab}^{-2} is plotted in Fig. 7.3(c). The low-T region in Fig. 7.3(c) shows, for at least $A = {\rm K}$ and Cs, a clear linear dependence of λ_{ab}. This indicates that the superconducting gaps of these compounds likely contain line nodes (see Sec. 6.2).

The data in Fig. 7.3(c) have been fitted with single- and two-gap BCS models involving s- and d-wave gaps. The BCS model of the normalised superfluid density of a superconductor is given by Eq. 6.3. The total normalised superfluid density for a two-gap model is a weighted sum of the superfluid densities associated with the individual gaps: $\tilde{n}_{\rm s}(T) = x\tilde{n}_{\rm s}^{(\text{gap 1})}(T) + (1-x)\tilde{n}_{\rm s}^{(\text{gap 2})}(T)$.

The existence of an inflection point in $\lambda_{ab}(T)$ for all A strongly suggests the existence of two gaps, and is supported by poor single-gap s-wave and d-wave fits. The χ^2 values of two-gap fits for $s+s$, $s+d$, and $d+d$ gaps are given in Tab. 7.1. We find that the $s+d$-wave model describes all three superconductors well, although the $d+d$-wave and $s+s$-wave models also provide a good fit for $A = \mathrm{K}$ and $A = \mathrm{Rb}$ respectively. To compare the compounds directly, the fitted parameters from the $s+d$-wave models are plotted in Fig. 7.3(d–h). $\lambda_{ab}(0)$ increases and T_c decreases with increasing atomic radius of the A atom. The increase in T_c is accompanied by a increase in size of the larger s-wave gap Δ_s. There does not appear to be a correlation between T_c and the smaller d-wave gap, but this gap contributes relatively little ($1 - x \approx 0.3$) to the total superfluid stiffness and therefore is not expected to strongly influence the superconducting properties.

One key difference between the compounds is the lattice parameter c (32.363(1) Å for $A = \mathrm{Cs}$, compared with 31.007(1) Å for $A = \mathrm{K}$ and 31.667(1) Å for $A = \mathrm{Rb}$ [175, 176]). However, this geometric difference is insufficient to account for the change in superfluid stiffness (for a contrary case see Ref. 182). For $A\mathrm{Ca_2Fe_4As_4F_2}$, a relatively small increase in c ($\approx 5\%$) provides a much larger decrease in $\lambda_{ab}(0)$ ($\approx 20\%$), demonstrating that the increase in c is, at best, only partially responsible for the reduction in $\lambda_{ab}(0)$ and suggesting that other effects associated with the electronic band structure must be contributing more strongly.

7.4 Magnetism

ZF-μSR measurements were made in order to investigate the possibility of magnetism, TRSB, and an FμF state. Sample spectra above and below T_c are presented in Fig. 7.4(a–c). It is clear that there are no oscillations in the spectra, indicating no long range magnetic order or FμF bonds in these compounds. The absence of an FμF signal is common to all fluorine-containing iron-based superconductors studied

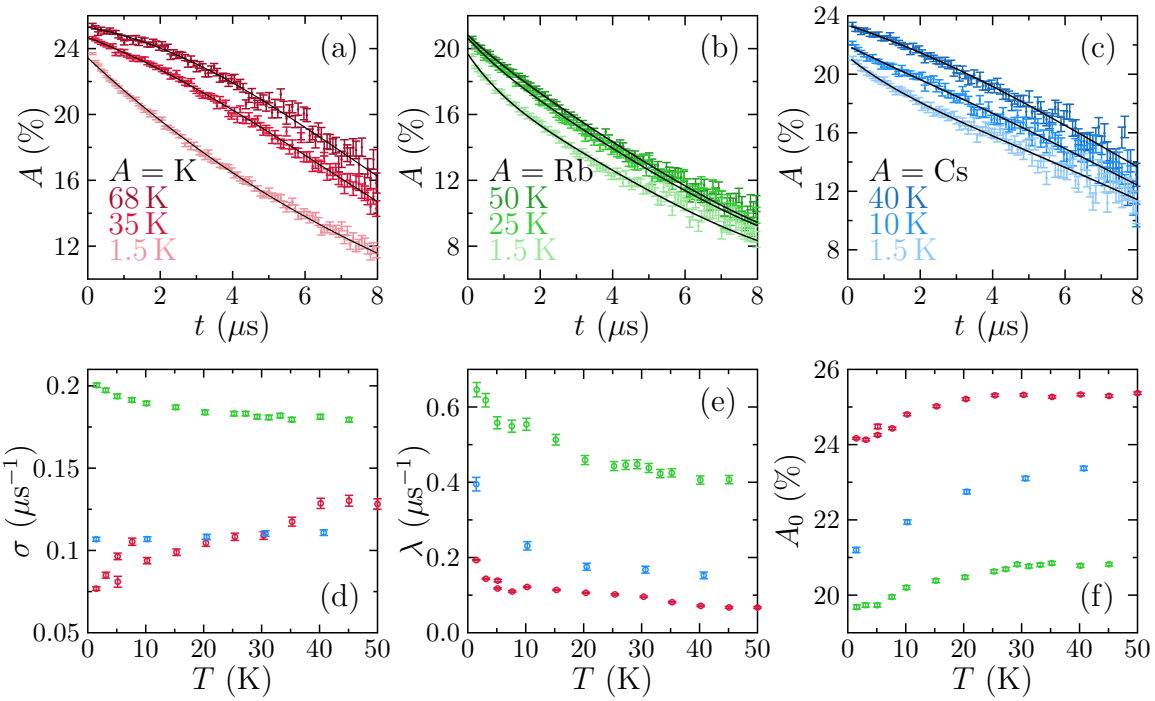

Figure 7.4: ZF-μSR spectra below, near, and above T_c are shown for (a) A = K, (b) Rb, and (c) Cs. Temperature dependence of the Lorentzian relaxation rate λ, Gaussian relaxation rate σ and initial asymmetry A_0 from fits to the ZF spectra in (a–c) using Eq. 7.3 are shown in (d), (e), and (f) respectively.

so far [183, 184, 185]. This may be due either to a muon site close to the FeAs planes (sitting between the As and Ca ions), away from the fluorine ions, or to the metallic nature of the material. The data can be modelled well with

$$A(t) = (A_0 - A_b)\left(ae^{-\sigma^2 t^2/2} + (1-a)e^{-\lambda t}\right) + A_b. \tag{7.3}$$

The first component in this function was found to have an approximately constant Gaussian relaxation, plotted in Fig. 7.4(d), likely arising from nuclear moments in the sample. The second component contained a temperature-dependent, fast Lorentzian relaxation, plotted in Fig. 7.4(e). The third component, the baseline asymmetry A_b, is due to muons that do not stop in the superconducting volume of the sample; this includes muons implanted in the cryostat and sample holder, as well as muons that are in non-superconducting parts of the sample. For A = K and Cs, $A_b = 0$, and for A = Rb, $A_b \approx 6\%$. We note a decrease in the initial asymmetry A_0, also plotted

in Fig. 7.4(f), which likely arises from an additional fast relaxation outside of the resolution of the spectrometer.

The presence of two relaxing components in Eq. 7.3 suggests that there are at least two potential muon sites. The values for a were found to be $a_{A=\mathrm{K}} \approx 0.43$, $a_{A=\mathrm{Rb}} \approx 0.63$, and $a_{A=\mathrm{Cs}} \approx 0.76$, meaning that, in the case of multiple muon sites, they appear to be sensitive to the structural changes caused by changing A.[3]

It is possible that the ZF relaxation may affect the TF spectra in Fig. 7.3(c), similar to the behaviour seen in Ref. 186. By fitting the data in Fig. 7.3(c) with an additional Lorentzian relaxation, we find a negligible change in the extracted superconducting parameters as well as a larger value of χ^2. It is therefore likely that the source of relaxation in ZF has little effect on the superconductivity observed in the TF data.

While we expect fluorine to be the dominant contribution to σ (as the muon site is likely to be near a fluorine atom, and the F nuclear moment is large: $2.63\,\mu_\mathrm{N}$), there also appears to be some A dependence. The nuclear magnetic moments of K, Rb, and Cs are $0.21\mu_\mathrm{N}$, $1.35\mu_\mathrm{N}$, and $2.58\mu_\mathrm{N}$ respectively. However, we note that the largest Gaussian relaxation is observed for $A = \mathrm{Rb}$. This may be due to a combination of both the size of the rare earth nuclear moment and the muon's distance from the rare earth atom; as discussed above, c increases with A's atomic radius. Therefore, although the Cs has a larger nuclear moment than Rb, it is possible that the muon site lies further from the rare earth atom in $CsCa_2Fe_4As_4F_2$, therefore reducing the width of the field distribution at the muon site (and so giving a lower σ).

There are several possible explanations for the gradual increase of λ and decrease of A_0 at low T. One possibility is the slowing of fluctuating electronic moments with field width Δ (where $\lambda = 2\Delta^2/\nu$ for fluctuation frequency ν). Similar behaviour has been observed in other FeAs superconductors [186]. A source of these moments may

[3] a and $1 - a$ denote the fractions of muons experiencing Gaussian and Lorentzian relaxations respectively.

be Fe-based impurities, which cannot be ruled out below the 1% level. The asymmetry of the TF data does not change significantly below T_c, which is compatible with weak magnetism similar to that observed in heavily doped $CaFe_{1-x}Co_xAsF$ [184]. We can differentiate true nodal superconductors (where the nodes are imposed by symmetry) to gapped superconductors with 'accidental nodes', as impurity scattering acts to broaden symmetry nodes and lifts accidental nodes and therefore removes the residual linear term in the case of accidental nodes. If the relaxation arises from Fe-based impurities, this would support the notion that the nodes are symmetry-imposed. Another possible explanation for the anomalous behaviour for A = Cs in Fig. 7.3(b) could be due to the opening of the second superconducting gap at approximately the same T. This situation may be similar to the Q phase in $CeCoIn_5$ [187, 188] and the pair-density waves in undoped cuprates [189], both of which exhibit intertwined magnetic order coupled to d-wave superconductivity [190]. The anomalous behaviour in Fig. 7.3(b) could also be explained by such a scenario, although we note that, interestingly, the anomaly is absent for A = K and Rb. Despite the absence of oscillations in this experiment, it is possible that magnetic order does exist with oscillations faster than the resolution of the spectrometer; such behaviour has previously been seen in the near-zero doping of $CaFe_{1-x}Co_xAsF$, where oscillations from a magnetic phase with frequency ≈ 25 MHz are observed [184].

The signature of a TRSB superconductor is the spontaneous formation of an internal magnetic field below T_c [191]; as this is not seen via a discontinuity in A_0 or λ at T_c, we conclude the $ACa_2Fe_4As_4F_2$ compounds do not undergo this transition. We can therefore deduce that the gap symmetry is probably $s + d$-wave, rather than $s + id$.

7.5 Conclusion

We have measured the superconducting and magnetic properties of polycrystalline samples of $A\mathrm{Ca_2Fe_4As_4F_2}$ (A = K, Rb, and Cs). We find that a small potentially magnetic phase exists in the sample, which does not appear to compete with the superconductivity. Remarkably, we find that all of the samples appear to exhibit multigap nodal superconductivity, with A = K being either $s + d$- or $d + d$-wave, A = Rb being either $s + s$- or $s + d$-wave, and A = Cs being $s + d$-wave. However, as μSR experiments are insensitive to the sign of the superconducting gap, it is also possible that our observed d-wave gaps are in fact highly anisotropic s-wave gaps. The ratio $\Delta_0/k_\mathrm{B}T_\mathrm{c}$ of the larger gap suggests strongly coupled superconductivity in all three compounds, although the value of the fitted gap may be sensitive to the area of the nodal region in the Fermi surface [192]. Due to the crystallographic structure of these compounds, there are two distinct As sites either side of the Fe atoms, and it can be distinguished from the s-wave superconductor $A\mathrm{CaFe_4As_4}$ by exchanging one of the spacer layers between the FeAs planes. As such, these results indicate a new path from gapped to nodal superconductivity in iron-based superconductors.

8

Observation of a crossover from nodal to gapped superconductivity in $Lu_xZr_{1-x}B_{12}$

While the superconducting gap symmetry can vary between families of superconductors, variation within a family is relatively rare. Compounds in the same family share similar crystal structures and often have similar electronic and magnetic properties. By looking at the small differences between the family members, it allows us to more easily pinpoint the properties that strongly influence the superconducting parameters. In this chapter, I present a μSR study of the $Lu_xZr_{1-x}B_{12}$ superconductors. By increasing x, it is possible to change the gap symmetry from nodal to fully gapped. A small magnetic phase coexists in the sample, and the exact details of this phase appear to be dependent on the sample preparation. I find, however, that the superconductivity appears to be robust. This work is based on that in Ref. 123.

Stephen Blundell calculated the muon site and helped with the μSR experiments. Francis Pratt, and Chris Baines also assisted with the μSR experiments. The samples

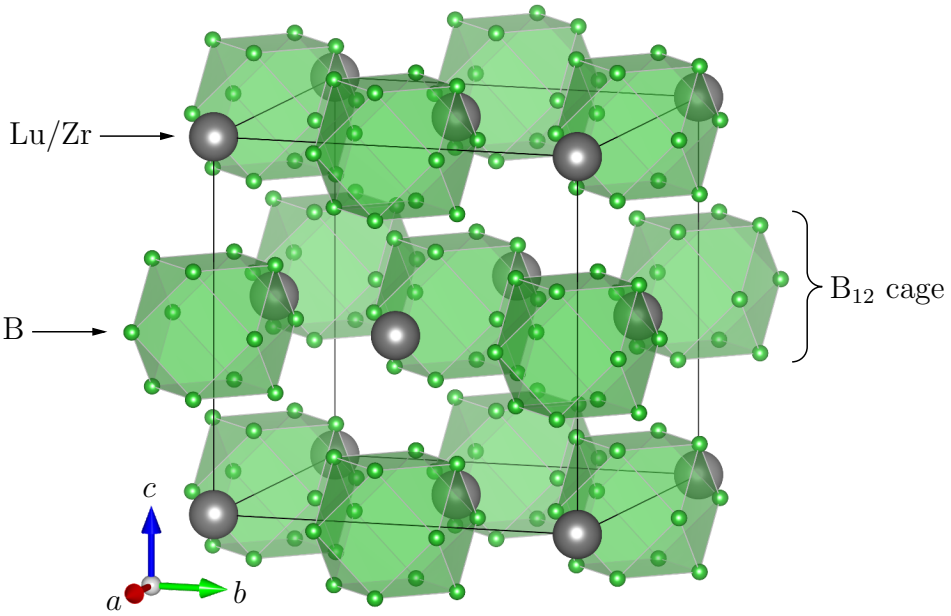

Figure 8.1: The unit cell of Lu/ZrB_{12}. The B_{12} cages are highlighted in green.

were synthesised by Natalya Shitsevalova and Vladimir Filipov. Nickolay Sluchanko assisted with the theoretical interpretation of the results, performed the resistivity measurements, and calculated κ and B_{c2}.

8.1 Introduction

Since the discovery of superconductivity in MgB_2 [193], there has been a great interest in searching for superconductivity in a wide class of borides. ZrB_{12} is BCS superconductor with one of the highest critical temperatures ($T_c = 6\,K$) among boron-rich compounds [194]. LuB_{12}, another dodecaboride, is also a superconductor, albeit with a much lower $T_c = 0.48\,K$ [194] despite having a very similar crystal structure [195, 196], electronic density of states [197, 198, 199], and phonon density of states [200, 201] to ZrB_{12}. It is thought that the high T_c in ZrB_{12} originates from the soft vibrations of Zr^{4+} ions in the boron cages (this structure is shown in Fig. 8.1). These vibrations lead to a strong electron-phonon interaction [202, 203, 204]. In LuB_{12}, vibrations of Lu^{3+} ions have almost no contribution to the electron-phonon coupling,

perhaps due to the 'volume filling factor' of the B cages, which tunes the hybridisation between the Lu/Zr and B orbitals [201]. Another factor which may contribute to the lower T_c in LuB_{12} is the development of an electron instability due to the formation of dynamic charge stripes [205]. Though LuB_{12} appears to display s-wave behaviour [206], there has been considerable debate surrounding the nature of the superconducting gap function in ZrB_{12}. It has been suggested that ZrB_{12} is either a single-gap s-wave [207, 208], two-gap s-wave [209], or a d-wave [202] superconductor, with its Fermi surface composed of one open and two closed sheets [197, 199].

Nonmagnetic impurity substitutions impact on superconducting properties in various ways dependent on the pair-breaking mechanism. For example, Anderson's theorem implies that a small number of nonmagnetic impurities can dramatically suppress superconductivity in the case of an anisotropic gap in a d-wave superconductor [210, 211, 212]. Experiments on cuprates reveal that a spinless impurity introduced into the high-temperature superconductor host produces a large and spatially extended alternating magnetic polarisation in its vicinity [213]. Somewhat analogous behavior was found in $Lu_xZr_{1-x}B_{12}$, in which nonmagnetic Lu^{3+} ions are substituted for Zr^{4+} ions. Spin-polarised nanodomains of size ≈ 5 Å, containing moments $\approx 6\mu_B$ and nucleated around the Lu^{3+} ions, were found in some crystals [214], but not in others [215]. This is possibly due to details of the distribution of the Lu^{3+} ions in the lattice, or the presence of vacancies (as found in YB_6 [216]).

8.2 Experimental details

Four single crystals of $Lu_xZr_{1-x}B_{12}$ were investigated in this experiment; these included one 'magnetic' sample, which had previously displayed the nanodomain behaviour, and three 'nonmagnetic' samples, which displayed no such phenomena. The magnetic sample, $x = 0.07$, was identical to that used in Ref. 214. The remaining

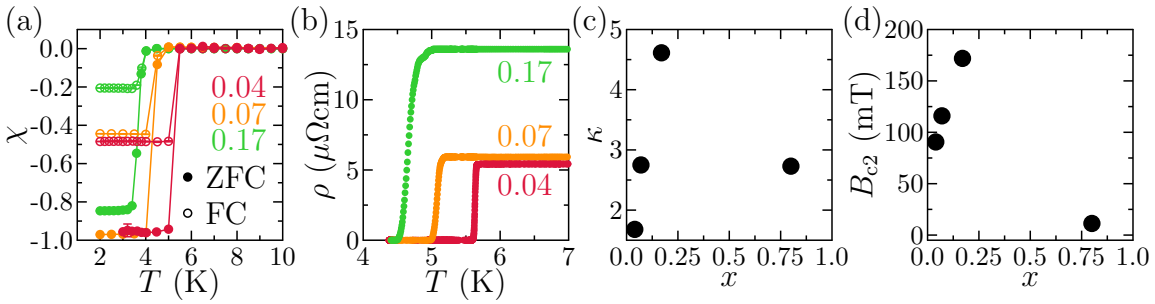

Figure 8.2: (a) Zero-field-cooled (ZFC) and field-cooled (FC) susceptibility for $x = 0.04$, 0.07, and 0.17. Measurements were made in an applied field of $\mu_0 H = 2\,\mathrm{mT}$. (b) Temperature dependence of the resistivity for $x = 0.04$, 0.07, and 0.17, showing a sharp superconducting transition at T_c. (c) Ginzburg-Landau parameter for various doping levels, calculated using the method in Ref. 204. (d) The dependence of the upper critical field on doping, calculated using the method in Refs. 214 and 215.

three samples, $x = 0.04$, 0.17, and 0.8, were nonmagnetic and identical to those studied in Ref. 215. Details of the crystal growth are described in Refs. 214 and 215. The crystal growth methods were identical for both the magnetic and nonmagnetic samples, with the single crystal samples being grown from a sintered rod. However, the sintered rods were obtained via different methods. For the magnetic sample, the sintered rod was produced from a powder of the crushed single crystal LuB_{12} and ZrB_{12}. Both powders were mixed and sintered into rods at 1750°C in a vacuum; this method is unable to guarantee a homogeneous mixture of Lu and Zr. Since there was a gradual re-melting of the rod during the synthesis of the single crystal, we cannot exclude an inhomogeneous distribution of Lu and Zr in the final crystal. In the case of the nonmagnetic samples, amorphous boron was mixed with Lu and Zr oxides (Lu_2O_3 and ZrO_2). These mixtures were pressed into tablets and held in a vacuum furnace for two hours at 1650°C to perform a solid-state synthesis, producing $(Lu,Zr)B_{12}$. To achieve a homogeneous distribution of the metal components after synthesis the tablets were crushed, pressed and annealed at 1650°C in vacuum. Then they were crushed and pressed once more to produce the rods, which were sintered in vacuum at 1750°C for one hour. As this method for producing the sintered rods

had one more homogenising annealing, we anticipate the Lu/Zr distribution in these samples to be significantly more homogeneous than in the sample produced using the first synthesis method.

μSR experiments [4, 105] were performed using a dilution refrigerator and ^{3}He sorption cryostat mounted on the MuSR spectrometer at the ISIS pulsed muon facility (Rutherford Appleton Laboratory, UK) [9]. Further experiments were carried out using the low temperature facility (LTF) and general purpose spectrometer (GPS) at the Swiss Muon Source. Transverse-field (TF) measurements were made to probe the superconducting ground state and its evolution with x. Zero-field (ZF) and longitudinal-field (LF) measurements were carried out in order to test for magnetic phases in the sample. All of the μSR data were analysed using WiMDA [106]. Magnetometry measurements were carried out on a Quantum Design SQUID magnetometer.

8.3 Superconductivity

TF-μSR measurements were performed on all of the samples to determine their superconducting properties. $x = 0.04$, 0.07, and 0.17 were measured above and below T_c in transverse applied fields B_{TF} of 30 mT and $x = 0.8$ was measured in $B_{TF} = 2.5$ mT [fields were chosen in order to lie below B_{c2} for each compound; see Fig. 8.2(d) for B_{c2} values]. Representative spectra for $x = 0.04$ above and below T_c are shown in Fig. 8.3(a). Transverse field sweeps were also made to determine the field dependence of the internal field distribution of the superconducting state.

The data were fitted with

$$A = A_{TF}\cos(\gamma_\mu B_{TF} t + \phi)e^{-\frac{\sigma_{TF}^2 t}{2}} + A_{SC}\cos(\gamma_\mu B_{SC} t + \phi)e^{-\frac{\sigma^2 t}{2}}, \qquad (8.1)$$

where ϕ is related to the detector geometry [the data were divided among eight groups of detectors with ϕ fitted for each group]. The first term corresponds to a background signal arising from muons that stop outside of the superconducting volume:

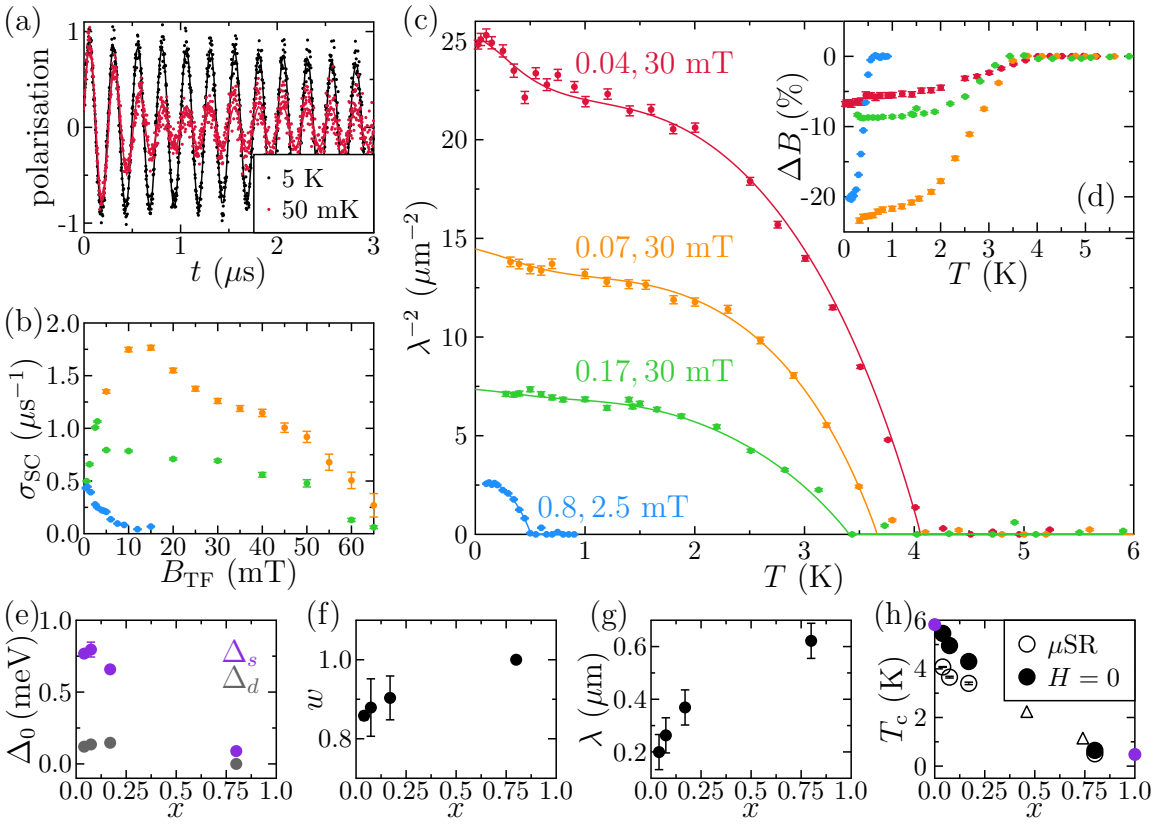

Figure 8.3: (a) Sample TF-μSR spectra above and below T_c for $x = 0.04$. Fits as in Eq. 8.1 are also plotted. (b) Field dependence of the relaxation due to superconductivity for $x = 0.07$ at 1.5 K (orange), $x = 0.17$ at 1.5 K (green), and $x = 0.8$ at 0.1 K (blue). (c) Temperature dependence of the inverse square penetration depth, with $s + d$-wave fits for $x = 0.04, 0.07$, and $x = 0.17$, and an s-wave fit for $x = 0.8$. (d) T dependence of the field shift $\Delta B = B_{SC} - B_{TF}$, expressed as a percentage of B_{TF}, due to the superconducting vortex lattice. The evolution of the superconducting gaps, the gap ratio, and the penetration depth with x are given in (e), (f), and (g) respectively. (h) The critical temperature measured in an applied field using μSR, as well as zero field ($H = 0$) values calculated from the magnetometry data. In the μSR study on $x = 0.8$, the applied field was 2.5 mT, while for all other samples it was 30 mT. The purple points are the T_c values for ZrB_{12} and LuB_{12} from Ref. 194, and the triangles are recently measured points for intermediate doping.

in the cryostat, sample holder, and non-superconducting regions of the sample. These muons precess only in the external field and experience a small Gaussian relaxation. The second term corresponds to muons in the superconductor, which experience an approximately Gaussian relaxation arising from the field distribution of the vortex lattice. These muons also experience a small, temperature independent relaxation

x	s-wave	d-wave	$s+s$-wave	$s+d$-wave
0.04	20.9	23.2	15.8	**14.1**
0.07	11.9	10.9	12.1	**10.0**
0.17	18.8	16.5	16.6	**13.8**
0.8	**16.9**	19.7	19.3	22.6

Table 8.1: The values of χ^2 for the best fits to various single and multigap models, using Eq. 6.3 for all of the samples (details of the fits are given in the main text.). The values in bold indicate the best fitting models.

from nuclear moments, giving a total relaxation $\sigma(T) = \sqrt{\sigma_{\rm SC}^2(T) + \sigma_{\rm nucl}^2}$.

The transverse field dependences of $\sigma_{\rm SC}$ for $x = 0.07$, 0.17, and 0.8 are shown in Fig. 8.3(b). There is a muon quadrupolar resonance due to the boron nuclei at $\approx$ 4 mT, which may affect the low-field dependence (this will be further discussed below). Apart from $x = 0.8$, the upper critical fields $B_{\rm c2}$ of all the samples are larger than the fields resolvable by the experiment; these have instead been calculated from magnetometry and heat capacity measurements in Refs. 214 and 215, and are shown in Fig. 8.2(d).

Assuming all of the samples are type II superconductors with an isotropic hexagonal Abrikosov vortex lattice that can be described by Ginzburg-Landau theory, the in-plane penetration depth λ can be extracted from the relaxation due to superconductivity using $\sigma_{\rm SC} = 0.0609\gamma_\mu\phi_0\lambda^{-2}(T)$ [132].[1] Although the values of κ and $B_{\rm TF}/B_{\rm c2}$ (plotted in Fig. 8.2(c) and (d) respectively) for some of these compounds are slightly outside the parameters suggested for this approximation to be valid (see Table 6.3), we can estimate an error by comparing this approximation and the analytical relationship between $\sigma_{\rm SC}$ and the applied field in Ref. 132. We find the approximation correctly describes this relationship to within 10% for the $x = 0.04$ and 0.07 samples, and to within 20% for $x = 0.17$ and 0.8. The temperature dependence of λ^{-2} is shown in Fig. 8.3(c), and the corresponding field shifts due to the vortex lattice $\Delta B = B_{\rm SC} - B_{\rm TF}$ are given in Fig. 8.3(d).

[1] As $Lu_xZr_{1-x}B_{12}$ is cubic, we assume the penetration depth is isotropic.

To determine the nature of the superconducting gaps in the samples, we fitted the data with single-gap BCS s-wave and d-wave models, as well as two-gap $s+s$- and $s+d$-wave models. The BCS model of the normalised superfluid density of a superconductor is given by Eq. 6.3. As introduced in Sec. 7.3, the total $\tilde{n}_{\rm s}(T)$ in a multigap model can be described as $\tilde{n}_{\rm s}(T) = w\tilde{n}_{\rm s}^{\rm gap\ 1}(T) + (1-w)\tilde{n}_{\rm s}^{\rm gap\ 2}(T)$. In the case of the $s+d$-wave fits, the first gap is s-wave, whereas the second gap is d-wave.

We find that $x = 0.04$, 0.07, and 0.17 are $s+d$-wave superconductors, whereas $x = 0.8$ is purely s-wave. χ^2 values for s-, d-, $s+s$-, and $s+d$-wave fits for all of the samples are shown in Tab. 8.1. A key indicator of nodal superconductivity is the linear dependence of λ^{-2} at low T, which is observed in $x = 0.04$, 0.07, and 0.17. $x = 0.8$, on the other hand, shows a low temperature plateau in λ^{-2}, corresponding to a fully gapped superconductor where low-energy excitations are strongly suppressed [217] (this is further discussed in Sec. 6.3). This is consistent with the s-wave superconductivity observed in LuB_{12} [206]. Our observations show that the nodal gap becomes less anisotropic and eventually becomes isotropic as x increases. This change of gap structure is accompanied by a rapid suppression of $T_{\rm c}$, shown in Fig. 8.3(g). The fitted values of the s- and d-wave superconducting gaps, Δ_s and Δ_d respectively, are shown in Fig, 8.3(e); we find that along with the complete suppression of the nodal gap (indicated by $w \to 1$ in Fig. 8.3(f)), the s-wave gap also decreases significantly in size with increasing x. For all of the samples, we find that the gap to $T_{\rm c}$ values $\Delta_s/k_{\rm B}T_{\rm c} \approx 2$–$2.5$ (> 1.76, the BCS value) for the larger s-wave gap, meaning these compounds are likely strongly-coupled superconductors (although for the multi-gapped samples, $\Delta_d/k_{\rm B}T_{\rm c} \approx 0.3$–$0.5$ in all cases). As x increases, the superfluid density ($n_{\rm s} \propto \lambda^{-2}(0)$) is suppressed, leading to a longer penetration depth as shown in Fig. 8.3(h). The multigap model agrees well with the two peaks observed in the field dependence of $\sigma_{\rm SC}$ for $x = 0.07$ [see Fig. 8.3(b)]. The peak at $B_{\rm TF} \approx 12\,{\rm mT}$ may be a reflection of the field dependence of the weak d-wave term on top of the

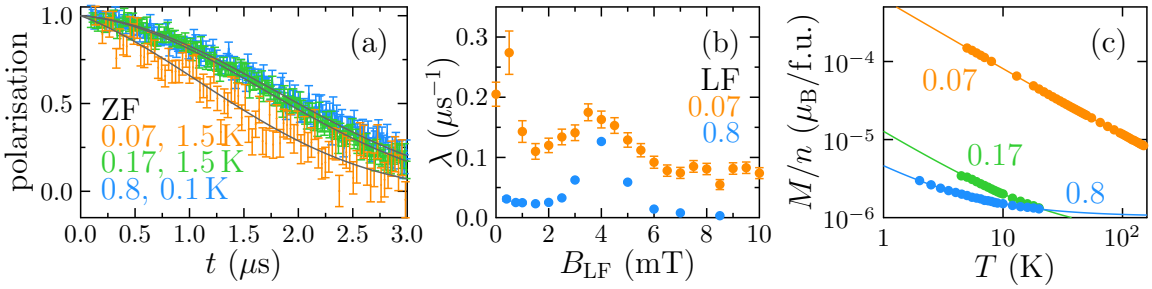

Figure 8.4: (a) Sample ZF-μSR spectra in the superconducting state. (b) The field dependence of the relaxation for one magnetic sample ($x = 0.07$, orange) and one nonmagnetic sample ($x = 0.8$, blue). The measurements for $x = 0.07$ were taken at 5 K and for $x = 0.8$ at 0.7 K. (c) The temperature dependence of the magnetisation per formula unit.

s-wave term. As the d-wave contribution is more easily suppressed by an external field, we expect w to be field-dependent. From the amplitude of the 12 mT peak we can estimate that the corrected value of w in the low field London limit should be closer to 0.7 for this sample and will be similarly reduced for the other low-x samples.

The observed gap evolution in the $Lu_xZr_{1-x}B_{12}$ is similar to that seen in Fe-based superconductors. The $Ba_{1-x}K_xFe_2As_2$ family of materials shows fully gapped behaviour for $x = 0.4$, with line nodes appearing at $x = 1$ [122]. A similar transition is achieved in $Ba_{0.65}Rb_{0.35}Fe_2As_2$ using hydrostatic pressure, which promotes a nodal gap [121].

8.4 Magnetism

8.4.1 ZF- and LF-μSR

To address the apparent discrepancy between the differing magnetic behaviours of this family of compounds observed in Refs. 214 and 215, ZF- and LF-μSR experiments were carried out.

ZF spectra below T_c for one magnetic sample ($x = 0.07$) and two nonmagnetic samples ($x = 0.17$ and 0.8) are shown in Fig. 8.4(a). For all samples there was no detectable change in the ZF spectrum as T was increased above T_c, meaning that any

magnetism present in the samples does not compete with the superconducting phase. No oscillations were seen in the forward-backward asymmetry spectra, and there were also no discontinuous jumps in either the initial or the baseline asymmetry, which suggests there is no long-range order inside the sample. The data were fitted with the zero-field Kubo-Toyabe function [218] with an additional Lorentzian relaxation:

$$A = A_0 \left(\frac{1}{3} + \frac{2}{3} \left(1 - \Delta_{\mathrm{ZF}}^2 t^2\right) e^{-\Delta_{\mathrm{ZF}}^2 t^2/2} \right) e^{-\lambda_{\mathrm{ZF}} t} + A_{\mathrm{b}}, \tag{8.2}$$

where A_0 and A_{b} are the relaxing and baseline amplitudes. The relaxing amplitude corresponds to muon stopping in the magnetic portion of the sample, while the baseline amplitude represents muons landing in nonmagnetic regions, for example in the cryostat or sample holder. The Kubo-Toyabe function is often used to describe a system of static spins with a Gaussian field distribution characterised by an RMS width $\Delta_{\mathrm{ZF}}/\gamma_\mu$.

Δ_{ZF} was found to be constant and temperature independent ($0.40(3)\,\mu\mathrm{s}^{-1}$) across all of the samples. It is therefore likely that the Kubo-Toyabe relaxation arises due to the nuclear moments associated with the B cage. The additional Lorentzian relaxation was equal and very small for the two nonmagnetic samples ($\approx\ 0.05\,\mu\mathrm{s}^{-1}$), and significantly larger for the magnetic sample ($\approx\ 0.2\,\mu\mathrm{s}^{-1}$).

To further probe the nature of the magnetism, LF-μSR was carried out on one magnetic and one nonmagnetic sample: $x = 0.07$ and $x = 0.8$ respectively. The data were fitted with a longitudinal-field Kubo-Toyabe function [5] with an additional Lorentzian relaxation $e^{-\lambda_{\mathrm{ZF}} t}$; the field dependence of λ_{ZF} is plotted in Fig. 8.4(b). Both samples have a peak in their relaxation at $B \approx 4\,\mathrm{mT}$, corresponding to the muon experiencing a quadrupolar resonance with the ^{11}B nucleus [219, 220]. The additional relaxation seen in the ZF spectrum of the magnetic sample is quenched above $\approx 1\,\mathrm{mT}$, indicating an internal field on the order of $0.1\,\mathrm{mT}$ arising from static magnetic moments [an applied longitudinal field $B_{\mathrm{LF}} > 10 B_{\mathrm{internal}}$ rapidly quenches relaxation arising from static moments [4, 5]].

Using DFT, we identify a single muon site at $[0.5, 0.5, 0.5]$, in the centre of the B_{12} cage. This muon position was calculated by solely examining the electrostatic potential within the unit cell (see Sec. 3.1), and so does not take into account any distortions of the crystal structure due to the muon's presence. We can, however, estimate the distortion in the unit cell by examining the Kubo-Toyabe relaxation in Eq. 8.2. As the muon is surrounded by a boron cage, it is likely that the largest distortion will be a small, symmetric expansion or contraction of the cage, such that each boron moves along the vector connecting it to the muon. For a system of randomly oriented nuclear spins with nuclear quantum number I at positions r_i [4],

$$\Delta_{\mathrm{ZF}}^2 = \frac{2}{3}\gamma_\mu^2\gamma_{\mathrm{nucl}}^2\left(\frac{\mu_0}{4\pi}\right)^2 I(I+1)\hbar^2\sum_i \frac{1}{(r_i - r_\mu)^6}, \tag{8.3}$$

where γ_{nucl} is the gyromagnetic ratio of the nuclei. By considering both ^{10}B and ^{11}B nuclei (with $I = 3$ and $3/2$ respectively), we can tune the positions of the B atoms to find the most probable distortion. We find that the theoretical and experimental values of Δ_{ZF} are in excellent agreement for a small contraction of the B_{12} cage, with each B moving ≈ 0.36–$0.37\,\text{Å}$ towards the muon.[2]

The Lorentzian relaxation in Eq. 8.2 likely arises due to static, dilute moments [221], and hence the relatively large λ_{ZF} for the magnetic sample may be due to the formation of dilute nanodomains consisting of static moments associated with the Lu atoms. Using DFCs (see Sec. 3.1), we find domains of size $\sim 7\,\text{Å}$ give $\lambda_{\mathrm{ZF}} \approx 0.1$–$0.2\,\mu\mathrm{s}^{-1}$, where the moments associated with these domains is $\approx 0.8\mu_{\mathrm{B}}$.

8.4.2 Magnetometry

The observed differences in magnetism are supported by bulk magnetometry measurements of $x = 0.07$, 0.17, and 0.8 above T_{c}, as shown in Fig. 8.4(c). The data were

[2]The variation here arises from the x-dependence of the lattice parameter a.

fitted to a Curie-Weiss function with an additional constant background magnetisation:

$$M = M_0 + n\mu_0\mu^2 H/3k_{\mathrm{B}}T, \tag{8.4}$$

where μ is the effective magnetic moment per formula unit, n is the number density, and $\mu_0 H = 2\,\mathrm{mT}$ is the applied external field. We find that the moment per formula unit in the magnetic sample ($\mu_{0.07} \approx 1.2\mu_{\mathrm{B}}$; close to that predicted by DFCs) is significantly higher than for the nonmagnetic samples ($\mu_{0.17} \approx 0.2\mu_{\mathrm{B}}$, $\mu_{0.8} \approx 0.1\mu_{\mathrm{B}}$).

From these data, we postulate that the ZF signal observed in the nonmagnetic samples, which is insensitive to Lu^{3+} concentration, is dominated by B nuclei in the cages, similar to that observed in LuB_{12} [222]. In addition to this nuclear signal, the magnetic sample also contains static, disordered moments, which may potentially be associated with clusters of Lu^{3+}, similar to the phenomena discussed in Refs. 214 and 216. As the apparent clustering effect is only present in one sample, we conclude that the differences in magnetism we observe are likely due to the detailed distribution of cations that is established during sample preparation, rather than an intrinsic effect linked to x. We do note, however, that it is also possible that this magnetic behaviour could arise due to some extrinsic impurity phase. Although x-ray diffraction experiments indicate that our samples are of a high quality [214, 215], we cannot rule out such impurity phases below the $\sim 1\%$ level.

8.5 Conclusion

In summary, we have carried out μSR and magnetometry measurements to probe the nature of the magnetism and superconductivity in the $Lu_xZr_{1-x}B_{12}$ family of superconductors. ZF-μSR, LF-μSR, and magnetometry measurements reveal a strong magnetic signal in one sample, which was thought to contain magnetic nanodomains. The other samples were found to exhibit much weaker magnetism. We attribute this sample dependence to a clustering effect in which the distribution of Lu^{3+} may affect

the formation of static moments. We find that the moments associated with this effect are of order $1\,\mu_{\mathrm{B}}$. Scanning tunnelling microscopy or scanning electron microscopy may provide further insights into this effect. TF-μSR measurements revealed that the superconductivity was robust to these variations in magnetism. We find that the increase in T_{c} associated with the decrease of x is also accompanied by a decrease in penetration depth and the formation of nodes in the superconducting gap function. There are many extensions to the models we have used to fit our data. While our minimal models fit the data well, we stress that more in-depth studies of this family of materials are required to further probe the gap symmetries observed in our μSR data. The nodal superconductivity appears to occur even in the magnetic sample, we can deduce that the nodal gaps we observe are probably due to d-wave pairing (where line nodes are must exist due to the symmetry of $\Delta(\phi)$), rather than s-wave pairing with accidental nodes: impurity scattering (which is possible due to the variability in the magnetic properties of the sample) would broaden symmetry-imposed nodes and lift any accidental nodes. However, as introduced in Sec. 6.2, it is also possible that the observed d-wave behaviour is due to a very highly anisotropic s-wave gap; further low temperature studies are required to gain additional information about the precise gap topologies in these compounds. The unusual transition from nodal to gapped superconductivity is similar to that observed in iron pnictide superconductors, although we note that in the case of the pnictides, the formation of nodes in the superconducting gap is accompanied by a decrease in T_{c} and an decrease in the superfluid density [121, 122]. It has recently become possible to synthesise samples of $\mathrm{Lu}_x\mathrm{Zr}_{1-x}\mathrm{B}_{12}$ with $0.17 < x < 0.8$, and our work emphasises the need to probe the intermediate doping region in order to understand the full details of the crossover.

9

Conclusions

This thesis presents a series of theoretical and experimental studies on a broad selection of quantum materials.

The first study, presented in Chapter 4, explores the concept of emergence in the spin ices. While these materials are comprised of dipolar spins, the particular geometry of and interactions between these spins leads to excitations which manifest as emergent magnetic monopoles. The bulk properties of the spin ices have been investigated in detail, but a microscopic profile of individual and small ensembles of magnetic monopoles remains to be observed experimentally. In this chapter, I study the spin ice $Dy_2Ti_2O_7$ in order to propose several experiments to make this first microscopic observation of emergent monopoles. Monopoles traversing the lattice produce a fluctuating magnetic field. I show that, although these fluctuations are difficult to measure experimentally with a local probe inside the sample, it is possible to detect signatures of monopole motion from a nanoscale probe placed in close proximity to

the surface of a sample. I use Monte Carlo simulations to find the precise form of the magnetic noise spectrum produced by a small concentration of monopoles in a sample, and describe experiments that ought to be able to make such a measurement.

I then move to a different exotic magnet: $CoTi_2O_5$. In Chapter 5, I present the first investigation into the ground state of this material and find that it is an antiferromagnet below 26 K with propagation vector $\mathbf{k} = (\pm 1/2, 1/2/0)$. Remarkably, in the antiferromagnetic regime, the super-super-exchange interactions are perfectly frustrated, and therefore by symmetry it is required that the unit cell undergoes some sort of symmetry-breaking structural transition to relieve this frustration. As a result, the transition to magnetic order in $CoTi_2O_5$ is expected to be mediated by the spin Jahn-Teller effect. I find it is the lowest-symmetry structure known to exhibit this behaviour. Using a combination of theoretical techniques, I therefore propose a possible magnetostructural coupling scheme.

Moving to the topic of topology, the remaining two projects investigate the intricate link between the topology of the energy gap in superconductors and their other chemical, physical, and material properties.

Chapter 7 focusses on the $A Ca_2Fe_4As_4F_2$ family of iron-based superconductors, where A = K, Rb, or Cs. I find that these superconductors have multiple superconducting gaps, at least one of which is likely to be nodal. These compounds are structurally related to other superconductors; it is possible to construct $A Ca_2Fe_4As_4F_2$ by manipulating the spacer layers in the fully-gapped $A CaFe_4As_4$ compounds. The iron-based superconductors exhibit a wide range of gap topologies, and therefore it is vital to construct a coherent theory explaining why this is so. Multiple mechanisms have already been proposed, and my work adds to this by showing a new route through which it is possible to manipulate this topology.

This thesis reaches its crescendo with a study of the $Lu_xZr_{1-x}B_{12}$ family of superconductors in Chapter 8. Although it is possible to alter the gap topology by moving

between different families of superconductors, a variable gap topology within a single family is relatively rare. This is because members of a single family often have very similar crystal and electronic structures, and are therefore likely to have very similar superconducting properties. I show that by increasing x in $Lu_xZr_{1-x}B_{12}$, it is possible to cross over from a fully-gapped superconducting regime at high x to a nodal multigapped regime at low x. The formation of nodes is accompanied by a tenfold increase in the critical temperature of these superconductors, and I discuss the correlation between these and other superconducting properties, and their importance in the wider scope of theories of superconductivity.

Bibliography

[1] P. W. Anderson, Science **177**, 393 (1972).

[2] C. S. Wu, E. Ambler, R. W. Hayward, D. D. Hoppes, and R. P. Hudson, Physical Review **105**, 1413 (1957).

[3] R. L. Garwin, L. M. Lederman, and M. Weinrich, Physical Review **105**, 1415 (1957).

[4] A. A. Yaouanc and P. Dalmas de Réotier, *Muon spin rotation, relaxation, and resonance: applications to condensed matter* (Oxford University Press, 2011).

[5] R. S. Hayano, Y. J. Uemura, J. Imazato, N. Nishida, T. Yamazaki, and R. Kubo, Physical Review B **20**, 850 (1979).

[6] A. A. Abrikosov, Journal of Physics and Chemistry of Solids **2**, 199 (1957).

[7] E. H. Brandt, Reports on Progress in Physics **58**, 1465 (1995).

[8] Y. J. Uemura, T. Yamazaki, D. R. Harshman, M. Senba, and E. J. Ansaldo, Physical Review B **31**, 546 (1985).

[9] P. J. C. King, R. de Renzi, S. P. Cottrell, A. D. Hillier, and S. F. J. Cox, Physica Scripta **88**, 068502 (2013).

[10] S. Nakatsuji, Y. Nambu, H. Tonomura, O. Sakai, S. Jonas, C. Broholm, H. Tsunetsugu, Y. Qiu, and Y. Maeno, Science **309**, 1697 (2005).

[11] A. Yaouanc, P. Dalmas de Réotier, Y. Chapuis, C. Marin, G. Lapertot, A. Cervellino, and A. Amato, Physical Review B **77**, 092403 (2008).

[12] F. Bernardini, P. Bonfà, S. Massidda, and R. De Renzi, Physical Review B **87**, 115148 (2013).

[13] J. S. Möller, D. Ceresoli, T. Lancaster, N. Marzari, and S. J. Blundell, Physical Review B **87**, 121108 (2013).

[14] J. S. Möller, P. Bonfà, D. Ceresoli, F. Bernardini, S. J. Blundell, T. Lancaster, R. De Renzi, N. Marzari, I. Watanabe, S. Sulaiman, and M. I. Mohamed-Ibrahim, Physica Scripta **88**, 068510 (2013).

[15] F. R. Foronda, F. Lang, J. S. Möller, T. Lancaster, A. T. Boothroyd, F. L. Pratt, S. R. Giblin, D. Prabhakaran, and S. J. Blundell, Physical Review Letters **114**, 017602 (2015).

[16] J. S. Möller, *Muon-spin relaxation and its application in the study of molecular quantum magnets*, PhD thesis, University of Oxford, 2013.

[17] F. Lang, *Muon-spin relaxation and density functional techniques in the study of novel magnetic systems*, PhD thesis, University of Oxford, 2016.

[18] F. K. K. Kirschner, F. Lang, F. L. Pratt, T. Lancaster, Y. Shi, Y. Guo, A. T. Boothroyd, and S. J. Blundell, Proceedings of the 14th International Conference on Muon Spin Rotation, Relaxation and Resonance (μSR2017), JPS Conference Proceedings **21**, 011013 (2018).

[19] K. Binder, Reports on Progress in Physics **60**, 487 (1997).

[20] C. B. Browne, E. Powley, D. Whitehouse, S. M. Lucas, P. I. Cowling, P. Rohlfshagen, S. Tavener, D. Perez, S. Samothrakis, and S. Colton, IEEE Transactions on Computational Intelligence and AI in Games **4**, 1 (2012).

[21] D. Creal, Econometric Reviews **31**, 245 (2012).

[22] U. Cubasch, B. D. Santer, A. Hellbach, G. Hegerl, H. Höck, E. Maier-Reimer, U. Mikolajewicz, A. Stössel, and R. Voss, Climate Dynamics **10**, 1 (1994).

[23] N. Metropolis, A. W. Rosenbluth, M. N. Rosenbluth, A. H. Teller, and E. Teller, The Journal of Chemical Physics **21**, 1087 (1953).

[24] R. G. Melko and M. J. P. Gingras, Journal of Physics: Condensed Matter **16**, R1277 (2004).

[25] S. T. Bramwell and J. P. Gingras, Science **294**, 1495 (2001).

[26] R. G. Melko, B. C. den Hertog, and M. J. Gingras, Physical Review Letters **87**, 067203 (2001).

[27] F. K. K. Kirschner, F. Flicker, A. Yacoby, N. Y. Yao, and S. J. Blundell, Physical Review B **97**, 140402 (2017).

[28] K. A. Milton, Reports on Progress in Physics **69**, 1637 (2006).

[29] M. J. Harris, S. T. Bramwell, D. F. McMorrow, T. Zeiske, and K. W. Godfrey, Physical Review Letters **79**, 2554 (1997).

[30] C. Castelnovo, R. Moessner, and S. L. Sondhi, Nature (London) **451**, 42 (2008).

[31] I. A. Ryzhkin, Journal of Experimental and Theoretical Physics **101**, 481 (2005).

[32] D. J. P. Morris, D. A. Tennant, S. A. Grigera, B. Klemke, C. Castelnovo, R. Moessner, C. Czternasty, M. Meissner, K. C. Rule, J.-U. Hoffmann, K. Kiefer, S. Gerischer, D. Slobinsky, and R. S. Perry, Science **326**, 411 (2009).

[33] L. Pauling, Journal of the American Chemical Society **57**, 2680 (1935).

[34] D. A. Huse, W. Krauth, R. Moessner, and S. L. Sondhi, Physical Review Letters **91**, 167004 (2003).

[35] S. V. Isakov, K. Gregor, R. Moessner, and S. L. Sondhi, Physical Review Letters **93**, 167204 (2004).

[36] C. L. Henley, Physical Review B **71**, 014424 (2005).

[37] T. Fennell, P. P. Deen, A. R. Wildes, K. Schmalzl, D. Prabhakaran, A. T. Boothroyd, R. J. Aldus, D. F. McMorrow, and S. T. Bramwell, Science **326**, 415 (2009).

[38] C. L. Henley, Annual Review of Condensed Matter Physics **1**, 179 (2010).

[39] M. Hermele, M. P. A. Fisher, and L. Balents, Physical Review B **69**, 064404 (2003).

[40] A. P. Ramirez, A. Hayashi, R. J. Cava, R. Siddharthan, and B. S. Shastry, Nature (London) **399**, 333 (1999).

[41] D. Pomaranski, L. R. Yaraskavitch, S. Meng, K. A. Ross, H. M. L. Noad, H. A. Dabkowska, B. D. Gaulin, and J. B. Kycia, Nature Physics **9**, 353 (2013).

[42] T. Sakakibara, T. Tayama, Z. Hiroi, K. Matsuhira, and S. Takagi, Physical Review Letters **90**, 207205 (2003).

[43] M. E. Fisher, Journal of Statistical Physics **75**, 1 (1994).

[44] B. C. den Hertog and M. J. P. Gingras, Physical Review Letters **84**, 3430 (2000).

[45] S. T. Bramwell, M. J. Harris, B. C. den Hertog, M. J. Gingras, J. S. Gardner, D. F. McMorrow, A. R. Wildes, A. L. Cornelius, J. D. Champion, R. G. Melko, and T. Fennell, Physical Review Letters **87**, 047205 (2001).

[46] K. Matsuhira, C. Paulsen, E. Lhotel, C. Sekine, Z. Hiroi, and S. Takagi, Journal of the Physical Society of Japan **80**, 123711 (2011).

[47] P. Henelius, T. Lin, M. Enjalran, Z. Hao, J. G. Rau, J. Altosaar, F. Flicker, T. Yavors'kii, and M. J. P. Gingras, Physical Review B **93**, 24402 (2016).

[48] G. T. Barkema and M. E. J. Newman, Physical Review E **57**, 1155 (1998).

[49] M. E. J. Newman and G. T. Barkema, *Monte Carlo methods in statistical physics* (Oxford University Press, Oxford, 1999).

[50] J. Lago, S. J. Blundell, and C. Baines, Journal of Physics: Condensed Matter **19**, 326210 (2007).

[51] S. R. Dunsiger, A. A. Aczel, C. Arguello, H. Dabkowska, A. Dabkowski, M. H. Du, T. Goko, B. Javanparast, T. Lin, F. L. Ning, H. M. L. Noad, D. J. Singh, T. J. Williams, Y. J. Uemura, M. J. P. Gingras, and G. M. Luke, Physical Review Letters **107**, 207207 (2011).

[52] A. Savitzky and M. J. Golay, Analytical Chemistry **36**, 1627 (1964).

[53] E. Lefrançois, V. Cathelin, E. Lhotel, J. Robert, P. Lejay, C. V. Colin, B. Canals, F. Damay, J. Ollivier, B. Fåk, L. C. Chapon, R. Ballou, and V. Simonet, Nature Communications **8**, 209 (2017).

[54] G. Sala, C. Castelnovo, R. Moessner, S. L. Sondhi, K. Kitagawa, M. Takigawa, R. Higashinaka, and Y. Maeno, Physical Review Letters **108**, 217203 (2012).

[55] L. Bovo, J. A. Bloxsom, D. Prabhakaran, G. Aeppli, and S. T. Bramwell, Nature Communications **4**, 1535 (2013).

[56] C. Castelnovo, R. Moessner, and S. Sondhi, Physical Review B **84**, 144435 (2011).

[57] J. Snyder, B. G. Ueland, J. S. Slusky, H. Karunadasa, R. J. Cava, and P. Schiffer, Physical Review B **69**, 064414 (2004).

[58] L. D. C. Jaubert and P. C. W. Holdsworth, Nature Physics **5**, 258 (2009).

[59] J. A. Quilliam, L. R. Yaraskavitch, H. A. Dabkowska, B. D. Gaulin, and J. B. Kycia, Physical Review B **83**, 094424 (2011).

[60] V. Kaiser, S. T. Bramwell, P. C. W. Holdsworth, and R. Moessner, Physical Review Letters **115**, 037201 (2015).

[61] B. Tomasello, C. Castelnovo, R. Moessner, and J. Quintanilla, Physical Review B **92**, 155120 (2015).

[62] B. Raquet, Electronic Noise in Magnetic Materials and Devices, in *Spin Electronics*, 232–273, Springer Berlin Heidelberg, Berlin, Heidelberg, 2001.

[63] J. Müller, ChemPhysChem **12**, 1222 (2011).

[64] N. Wiener, Acta Mathematica **55**, 117 (1930).

[65] L. Rondin, J. P. Tetienne, T. Hingant, J. F. Roch, P. Maletinsky, and V. Jacques, Reports on Progress in Physics **77**, 056503 (2013).

[66] I. Lovchinsky, A. O. Sushkov, E. Urbach, N. P. de Leon, S. Choi, K. De Greve, R. Evans, R. Gertner, E. Bersin, C. Müller, L. McGuinness, F. Jelezko, R. L. Walsworth, H. Park, and M. D. Lukin, Science **351**, 836 (2016).

[67] L. Childress, M. V. Gurudev Dutt, J. M. Taylor, A. S. Zibrov, F. Jelezko, J. Wrachtrup, P. R. Hemmer, and M. D. Lukin, Science **314**, 281 (2006).

[68] J. R. Maze, P. L. Stanwix, J. S. Hodges, S. Hong, J. M. Taylor, P. Cappellaro, L. Jiang, M. V. G. Dutt, E. Togan, A. S. Zibrov, A. Yacoby, R. L. Walsworth, and M. D. Lukin, Nature (London) **455**, 644 (2008).

[69] F. Shi, Q. Zhang, P. Wang, H. Sun, J. Wang, X. Rong, M. Chen, C. Ju, F. Reinhard, H. Chen, J. Wrachtrup, J. Wang, and J. Du, Science **347**, 1135 (2015).

[70] M. S. Grinolds, S. Hong, P. Maletinsky, L. Luan, M. D. Lukin, R. L. Walsworth, and A. Yacoby, Nature Physics **9**, 215 (2012).

[71] P. Maletinsky, S. Hong, M. S. Grinolds, B. Hausmann, M. D. Lukin, R. L. Walsworth, M. Loncar, and A. Yacoby, Nature Nanotechnology **7**, 320 (2012).

[72] E. Morenzoni, T. Prokscha, A. Suter, H. Luetkens, and R. Khasanov, Journal of Physics: Condensed Matter **16**, S4583 (2004).

[73] Z. Salman and S. J. Blundell, Physics Procedia **30**, 168 (2012).

[74] S. J. Blundell, Physical Review Letters **108**, 147601 (2012).

[75] W. Wernsdorfer, Superconductor Science and Technology **22**, 64013 (2009).

[76] C. Granata and A. Vettoliere, Physics Reports **614**, 1 (2016).

[77] D. Vasyukov, Y. Anahory, L. Embon, D. Halbertal, J. Cuppens, L. Neeman, A. Finkler, Y. Segev, Y. Myasoedov, M. L. Rappaport, M. E. Huber, and E. Zeldov, Nature Nanotechnology **8**, 639 (2013).

[78] L. D. Jaubert, T. Lin, T. S. Opel, P. C. Holdsworth, and M. J. Gingras, Physical Review Letters **118**, 207206 (2017).

[79] É. Lantagne-Hurtubise, J. G. Rau, and M. J. P. Gingras, *arXiv* 1709.00012 (2017).

[80] F. K. K. Kirschner, R. D. Johnson, F. Lang, D. D. Khalyavin, P. Manuel, T. Lancaster, D. Prabhakaran, and S. J. Blundell, *arXiv* 1808.01387 (2018).

[81] G. A. Gehring and K. A. Gehring, Reports on Progress in Physics **38**, 1 (1975).

[82] Y. Yamashita and K. Ueda, Physical Review Letters **85**, 4960 (2000).

[83] O. Tchernyshyov, O. Tchernyshyov, R. Moessner, and S. L. Sondhi, Physical Review Letters **88**, 067203 (2002).

[84] M. Onoda and J. Hasegawa, Journal of Physics: Condensed Matter **15**, L95 (2003).

[85] T. Watanabe, S. I. Ishikawa, H. Suzuki, Y. Kousaka, and K. Tomiyasu, Physical Review B **86**, 144413 (2012).

[86] O. Waldmann, C. Dobe, S. T. Ochsenbein, H. U. Güdel, and I. Sheikin, Physical Review Letters **96**, 027206 (2006).

[87] O. Waldmann, Physical Review B **75**, 174440 (2007).

[88] S. Ogawa and S. Waki, Journal of the Physical Society of Japan **20**, 540 (1965).

[89] J. K. Srivastava, S. Ramakrishnan, V. R. Marathe, G. Chandra, R. Vijayaraghava, J. A. Kulkarni, V. S. Darshane, and S. Singh, Journal of Physics C: Solid State Physics **20**, 2139 (1987).

[90] G. Gavoille, J. Hubsch, and S. Koutani, Journal of Magnetism and Magnetic Materials **102**, 283 (1991).

[91] S. Nayak, S. Thota, D. C. Joshi, M. Krautz, A. Waske, A. Behler, J. Eckert, T. Sarkar, M. S. Andersson, R. Mathieu, V. Narang, and M. S. Seehra, Physical Review B **92**, 214434 (2015).

[92] D.-C. Kim and S.-K. Ihm, Environmental Science & Technology **35**, 222 (2001).

[93] J. Zhu and Q. Gao, Microporous and Mesoporous Materials **124**, 144 (2009).

[94] V. G. Harris, A. Geiler, Y. Chen, S. D. Yoon, M. Wu, A. Yang, Z. Chen, P. He, P. V. Parimi, X. Zuo, C. E. Patton, M. Abe, O. Acher, and C. Vittoria, Journal of Magnetism and Magnetic Materials **321**, 2035 (2009).

[95] C. P. Sandhya, B. John, and C. Gouri, Ionics **20**, 601 (2014).

[96] R. Ye, H. Fang, Y.-Z. Zheng, N. Li, Y. Wang, and X. Tao, ACS Applied Materials & Interfaces **8**, 13879 (2016).

[97] X. Chu, X. Liu, G. Wang, and G. Meng, Materials Research Bulletin **34**, 1789 (1999).

[98] T. S. Chao, W. M. Ku, H. C. Lin, D. Landheer, Y. Y. Wang, and Y. Mori, IEEE Transactions on Electron Devices **51**, 2200 (2004).

[99] B. Brezny and A. Muan, Journal of Inorganic and Nuclear Chemistry **31**, 649 (1969).

[100] H. Müller-Buschbaum and M. Waburg, Monatshefte für Chemie **114**, 21 (1983).

[101] A. Navrotsky, American Mineralogist **60**, 249 (1975).

[102] A. Yankin, O. Vikhreva, and V. Balakirev, Journal of Physics and Chemistry of Solids **60**, 139 (1999).

[103] K. T. Jacob and G. Rajitha, Journal of Chemical Thermodynamics **42**, 879 (2010).

[104] A. M. Balbashov, A. A. Mukhin, V. Y. Ivanov, L. D. Iskhakova, and M. E. Voronchikhina, Low Temperature Physics **43**, 965 (2017).

[105] S. J. Blundell, Contemporary Physics **40**, 175 (1999).

[106] F. L. Pratt, Physica B **710**, 289 (2000).

[107] L. C. Chapon, P. Manuel, P. G. Radaelli, C. Benson, L. Perrott, S. Ansell, N. J. Rhodes, D. Raspino, D. Duxbury, E. Spill, and J. Norris, Neutron News **22**, 22 (2011).

[108] J. Rodríguez-Carvajal, Physica B **192**, 55 (1993).

[109] B. J. Campbell, H. T. Stokes, D. E. Tanner, and D. M. Hatch, Journal of Applied Crystallography **39**, 607 (2006).

[110] H. T. Stokes, D. M. Hatch, and B. J. Campbell, ISOTROPY Software Suite, 2007.

[111] K. Momma and F. Izumi, Journal of Applied Crystallography **41**, 653 (2008).

[112] N. P. Grazhdankina, Soviet Physics Uspekhi **11**, 727 (1969).

[113] H. K. Onnes, Comm. Phys. Lab. Univ. Leiden **119-120** (1911).

[114] J. Bardeen, L. N. Cooper, and J. R. Schrieffer, Physical Review **108**, 1175 (1957).

[115] J. G. Bednorz and K. A. Müller, Zeitschrift für Physik B Condensed Matter **64**, 189 (1986).

[116] Y. Kamihara, H. Hiramatsu, M. Hirano, R. Kawamura, H. Yanagi, T. Kamiya, and H. Hosono, Journal of the American Chemical Society **128**, 10012 (2006).

[117] Y. Kamihara, T. Watanabe, M. Hirano, and H. Hosono, Journal of the American Chemical Society **130**, 3296 (2008).

[118] A. P. Drozdov, M. I. Eremets, I. A. Troyan, V. Ksenofontov, and S. I. Shylin, Nature (London) **525**, 73 (2015).

[119] X. Lai, H. Zhang, Y. Wang, X. Wang, X. Zhang, J. Lin, and F. Huang, Journal of the American Chemical Society **137**, 10148 (2015).

[120] F. K. K. Kirschner, F. Lang, C. V. Topping, P. J. Baker, F. L. Pratt, S. E. Wright, D. N. Woodruff, S. J. Clarke, and S. J. Blundell, Physical Review B **94**, 134509 (2016).

[121] Z. Guguchia, A. Amato, J. Kang, H. Luetkens, P. K. Biswas, G. Prando, F. von Rohr, Z. Bukowski, A. Shengelaya, H. Keller, E. Morenzoni, R. Fernandes, and R. Khasanov, Nature Communications **6**, 8863 (2015).

[122] J. P. Reid, M. A. Tanatar, A. Juneau-Fecteau, R. T. Gordon, S. R. De Cotret, N. Doiron-Leyraud, T. Saito, H. Fukazawa, Y. Kohori, K. Kihou, C. H. Lee, A. Iyo, H. Eisaki, R. Prozorov, and L. Taillefer, Physical Review Letters **109**, 087001 (2012).

[123] F. K. K. Kirschner, N. E. Sluchanko, V. B. Filipov, F. L. Pratt, C. Baines, N. Y. Shitsevalova, and S. J. Blundell, Physical Review B **98**, 094505 (2018).

[124] K. Hashimoto, A. Serafin, S. Tonegawa, R. Katsumata, R. Okazaki, T. Saito, H. Fukazawa, Y. Kohori, K. Kihou, C. H. Lee, A. Iyo, H. Eisaki, H. Ikeda, Y. Matsuda, A. Carrington, and T. Shibauchi, Physical Review B **82**, 014526 (2010).

[125] B. S. Chandrasekhar and D. Einzel, Annalen der Physik **505**, 535 (1993).

[126] V. L. Ginzburg and L. D. Landau, Soviet Physics JETP **20**, 1064 (1950).

[127] L. P. Gor'kov, Soviet Physics JETP **9**, 1364 (1959).

[128] J. F. Annett, *Superconductivity, Superfluids, and Condensates* (Oxford University Press, Oxford, 2005).

[129] R. Gilardi, J. Mesot, A. Drew, U. Divakar, S. L. Lee, E. M. Forgan, O. Zaharko, K. Conder, V. K. Aswal, C. D. Dewhurst, R. Cubitt, N. Momono, and M. Oda, Physical Review Letters **88**, 217003 (2002).

[130] S. Holenstein, U. Pachmayr, Z. Guguchia, S. Kamusella, R. Khasanov, A. Amato, C. Baines, H. H. Klauss, E. Morenzoni, D. Johrendt, and H. Luetkens, Physical Review B **93**, 140506 (2016).

[131] E. H. Brandt, Physical Review B **37**, 2349 (1988).

[132] E. H. Brandt, Physical Review B **68**, 054506 (2003).

[133] S. Medvedev, T. M. McQueen, I. A. Troyan, T. Palasyuk, M. I. Eremets, R. J. Cava, S. Naghavi, F. Casper, V. Ksenofontov, G. Wortmann, and C. Felser, Nature Materials **8**, 630 (2009).

[134] M. Burrard-Lucas, D. G. Free, S. J. Sedlmaier, J. D. Wright, S. J. Cassidy, Y. Hara, A. J. Corkett, T. Lancaster, P. J. Baker, S. J. Blundell, and S. J. Clarke, Nature Materials **12**, 15 (2013).

[135] J.-F. Ge, Z.-L. Liu, C. Liu, C.-L. Gao, D. Qian, Q.-K. Xue, Y. Liu, and J.-F. Jia, Nature Materials **14**, 285 (2015).

[136] V. I. Fesenko, V. N. Gorbunov, and V. P. Smilga, Physica C **176**, 551 (1991).

[137] Y. J. Uemura, G. M. Luke, B. J. Sternlieb, J. H. Brewer, J. F. Carolan, W. N. Hardy, R. Kadono, J. R. Kempton, R. F. Kiefl, S. R. Kreitzman, P. Mulhern, T. M. Riseman, D. L. Williams, B. X. Yang, S. Uchida, H. Takagi, J. Gopalakrishnan, A. W. Sleight, M. A. Subramanian, C. L. Chien, M. Z. Cieplak, G. Xiao, V. Y. Lee, B. W. Statt, C. E. Stronach, W. J. Kossler, and X. H. Yu, Physical Review Letters **62**, 2317 (1989).

[138] M. D. Watson, A. A. Haghighirad, L. C. Rhodes, M. Hoesch, and T. K. Kim, New Journal of Physics **19**, 103021 (2017).

[139] Y. S. Kushnirenko, A. V. Fedorov, E. Haubold, S. Thirupathaiah, T. Wolf, S. Aswartham, I. Morozov, T. K. Kim, B. Büchner, and S. V. Borisenko, Physical Review B **97**, 180501 (2018).

[140] M. Eschrig, Advances in Physics **55**, 47 (2006).

[141] T. Dahm, V. Hinkov, S. V. Borisenko, A. A. Kordyuk, V. B. Zabolotnyy, J. Fink, B. Büchner, D. J. Scalapino, W. Hanke, and B. Keimer, Nature Physics **5**, 217 (2009).

[142] F. K. K. Kirschner, D. T. Adroja, Z. C. Wang, F. Lang, M. Smidman, P. J. Baker, G. H. Cao, and S. J. Blundell, Physical Review B **97**, 060506 (2018).

[143] M. Smidman, F. K. K. Kirschner, D. T. Adroja, A. D. Hillier, F. Lang, Z. C. Wang, G. H. Cao, and S. J. Blundell, Physical Review B **97**, 060509 (2018).

[144] D. T. Adroja, F. K. K. Kirschner, F. Lang, M. Smidman, A. D. Hillier, Z.-C. Wang, G.-H. Cao, G. B. G. Stenning, and S. J. Blundell, *arXiv* 1802.07334 (2018).

[145] M. Hashimoto, I. M. Vishik, R.-H. He, T. P. Devereaux, and Z.-X. Shen, Nature Physics **10**, 483 (2014).

[146] K. Kuroki, S. Onari, R. Arita, H. Usui, Y. Tanaka, H. Kontani, and H. Aoki, Physical Review Letters **101**, 087004 (2008).

[147] I. I. Mazin, D. J. Singh, M. D. Johannes, and M. H. Du, Physical Review Letters **101**, 057003 (2008).

[148] Y. Nakai, K. Ishida, Y. Kamihara, M. Hirano, and H. Hosono, Journal of the Physical Society of Japan **77**, 073701 (2008).

[149] H. J. Grafe, D. Paar, G. Lang, N. J. Curro, G. Behr, J. Werner, J. Hamann-Borrero, C. Hess, N. Leps, R. Klingeler, and B. Büchner, Physical Review Letters **101**, 047003 (2008).

[150] D. V. Evtushinsky, D. S. Inosov, V. B. Zabolotnyy, A. Koitzsch, M. Knupfer, B. Buchner, M. S. Viazovska, G. L. Sun, V. Hinkov, A. V. Boris, C. T. Lin, B. Keimer, A. Varykhalov, A. A. Kordyuk, and S. V. Borisenko, Physical Review B **79**, 054517 (2008).

[151] R. Khasanov, D. V. Evtushinsky, A. Amato, H. H. Klauss, H. Luetkens, C. Niedermayer, B. Büchner, G. L. Sun, C. T. Lin, J. T. Park, D. S. Inosov, and V. Hinkov, Physical Review Letters **102**, 187005 (2009).

[152] H. Fukazawa, Y. Yamada, K. Kondo, T. Saito, Y. Kohori, K. Kuga, Y. Matsumoto, S. Nakatsuji, H. Kito, P. M. Shirage, K. Kihou, N. Takeshita, C. H. Lee, A. Iyo, and H. Eisaki, Journal of the Physical Society of Japan **78**, 083712 (2009).

[153] R. Thomale, C. Platt, W. Hanke, J. Hu, and B. A. Bernevig, Physical Review Letters **107**, 117001 (2011).

[154] J. K. Dong, S. Y. Zhou, T. Y. Guan, H. Zhang, Y. F. Dai, X. Qiu, X. F. Wang, Y. He, X. H. Chen, and S. Y. Li, Physical Review Letters **104**, 087005 (2010).

[155] K. Okazaki, Y. Ota, Y. Kotani, W. Malaeb, Y. Ishida, T. Shimojima, T. Kiss, S. Watanabe, C.-T. Chen, K. Kihou, C. H. Lee, A. Iyo, H. Eisaki, T. Saito, H. Fukazawa, Y. Kohori, K. Hashimoto, T. Shibauchi, Y. Matsuda, H. Ikeda, H. Miyahara, R. Arita, A. Chainani, and S. Shin, Science **337**, 1314 (2012).

[156] A. F. Wang, B. Y. Pan, X. G. Luo, F. Chen, Y. J. Yan, J. J. Ying, G. J. Ye, P. Cheng, X. C. Hong, S. Y. Li, and X. H. Chen, Physical Review B **87**, 214509 (2013).

[157] X. C. Hong, X. L. Li, B. Y. Pan, L. P. He, A. F. Wang, X. G. Luo, X. H. Chen, and S. Y. Li, Physical Review B **87**, 144502 (2013).

[158] Z. Zhang, A. F. Wang, X. C. Hong, J. Zhang, B. Y. Pan, J. Pan, Y. Xu, X. G. Luo, X. H. Chen, and S. Y. Li, Physical Review B **91**, 024502 (2015).

[159] Z. Shermadini, J. Kanter, C. Baines, M. Bendele, Z. Bukowski, R. Khasanov, H.-H. Klauss, H. Luetkens, H. Maeter, G. Pascua, B. Batlogg, and A. Amato, Physical Review B **82**, 144527 (2010).

[160] Z. Shermadini, H. Luetkens, A. Maisuradze, R. Khasanov, Z. Bukowski, H. H. Klauss, and A. Amato, Physical Review B **86**, 174516 (2012).

[161] P. J. Hirschfeld, M. M. Korshunov, and I. I. Mazin, Reports on Progress in Physics **74**, 124508 (2011).

[162] W. C. Lee, S. C. Zhang, and C. Wu, Physical Review Letters **102**, 217002 (2009).

[163] S. Maiti, M. M. Korshunov, T. A. Maier, P. J. Hirschfeld, and A. V. Chubukov, Physical Review Letters **107**, 147002 (2011).

[164] A. Iyo, K. Kawashima, T. Kinjo, T. Nishio, S. Ishida, H. Fujihisa, Y. Gotoh, K. Kihou, H. Eisaki, and Y. Yoshida, Journal of the American Chemical Society **138**, 3410 (2016).

[165] D. Mou, T. Kong, W. R. Meier, F. Lochner, L. L. Wang, Q. Lin, Y. Wu, S. L. Bud'Ko, I. Eremin, D. D. Johnson, P. C. Canfield, and A. Kaminski, Physical Review Letters **117**, 277001 (2016).

[166] K. Iida, M. Ishikado, Y. Nagai, H. Yoshida, A. D. Christianson, N. Murai, K. Kawashima, Y. Yoshida, H. Eisaki, and A. Iyo, Journal of the Physical Society of Japan **86**, 093703 (2017).

[167] P. K. Biswas, A. Iyo, Y. Yoshida, H. Eisaki, K. Kawashima, and A. D. Hillier, Physical Review B **95**, 140505 (2017).

[168] J. Cui, Q.-P. Ding, W. R. Meier, T. Kong, V. Borisov, Y. Lee, and S. L. Bud, Physical Review B **96**, 104512 (2017).

[169] K. Cho, A. Fente, S. Teknowijoyo, M. A. Tanatar, K. R. Joshi, N. M. Nusran, T. Kong, W. R. Meier, U. Kaluarachchi, I. Guillamón, H. Suderow, S. L. Bud'Ko, P. C. Canfield, and R. Prozorov, Physical Review B **95**, 100502 (2017).

[170] D. V. Suetin and I. R. Shein, Journal of Superconductivity and Novel Magnetism **31**, 1683 (2017).

[171] Z.-A. Ren, G.-C. Che, X.-L. Dong, J. Yang, W. Lu, W. Yi, X.-L. Shen, Z.-C. Li, L.-L. Sun, F. Zhou, and Z.-X. Zhao, EPL (Europhysics Letters) **83**, 17002 (2008).

[172] X.-C. Wang, J. Yu, B.-B. Ruan, B.-J. Pan, Q.-G. Mu, T. Liu, K. Zhao, G.-F. Chen, and Z.-A. Ren, Chinese Physics Letters **34**, 077401 (2017).

[173] J. K. Bao, J. Y. Liu, C. W. Ma, Z. H. Meng, Z. T. Tang, Y. L. Sun, H. F. Zhai, H. Jiang, H. Bai, C. M. Feng, Z. A. Xu, and G. H. Cao, Physical Review X **5**, 011013 (2015).

[174] Z. T. Tang, J. K. Bao, Y. Liu, Y. L. Sun, A. Ablimit, H. F. Zhai, H. Jiang, C. M. Feng, Z. A. Xu, and G. H. Cao, Physical Review B **91**, 020506 (2015).

[175] Z. C. Wang, C. Y. He, S. Q. Wu, Z. T. Tang, Y. Liu, A. Ablimit, C. M. Feng, and G. H. Cao, Journal of the American Chemical Society **138**, 7856 (2016).

[176] Z. Wang, C. He, Z. Tang, S. Wu, and G. Cao, Science China Materials **60**, 83 (2017).

[177] D. J. Scalapino, Reviews of Modern Physics **84**, 1383 (2012).

[178] H. Jiang, Y.-L. Sun, Z.-A. Xu, and G.-H. Cao, Chinese Physics B **22**, 087410 (2013).

[179] G. Wang, Z. Wang, and X. Shi, EPL (Europhysics Letters) **116**, 37003 (2016).

[180] J. H. Brewer, S. R. Kreitzman, D. R. Noakes, E. J. Ansaldo, D. R. Harshman, and R. Keitel, Physical Review B **33**, 7813 (1986).

[181] D. R. Harshman and M. Celio, Hyperfine Interactions **32**, 683 (1986).

[182] P. J. Baker, T. Lancaster, S. J. Blundell, F. L. Pratt, M. L. Brooks, and S. J. Kwon, Physical Review Letters **102**, 087002 (2009).

[183] H. Luetkens, H. H. Klauss, R. Khasanov, A. Amato, R. Klingeler, I. Hellmann, N. Leps, A. Kondrat, C. Hess, A. Köhler, G. Behr, J. Werner, and B. Büchner, Physical Review Letters **101**, 097009 (2008).

[184] S. Takeshita, R. Kadono, M. Hiraishi, M. Miyazaki, A. Koda, S. Matsuishi, and H. Hosono, Physical Review Letters **103**, 027002 (2009).

[185] G. Lamura, T. Shiroka, P. Bonfà, S. Sanna, R. De Renzi, M. Putti, N. D. Zhigadlo, S. Katrych, R. Khasanov, and J. Karpinski, Physical Review B **91**, 024513 (2015).

[186] R. Khasanov, K. Conder, E. Pomjakushina, A. Amato, C. Baines, Z. Bukowski, J. Karpinski, S. Katrych, H.-H. Klauss, H. Luetkens, A. Shengelaya, and N. D. Zhigadlo, Physical Review B **78**, 220510 (2008).

[187] D. F. Agterberg, M. Sigrist, and H. Tsunetsugu, Physical Review Letters **102**, 207004 (2009).

[188] Y. Kato, C. D. Batista, and I. Vekhter, Physical Review Letters **107**, 096401 (2011).

[189] E. Berg, E. Fradkin, and S. A. Kivelson, Physical Review B **79**, 064515 (2009).

[190] E. Fradkin, S. A. Kivelson, and J. M. Tranquada, Reviews of Modern Physics **87**, 457 (2015).

[191] G. M. Luke, T. Fudamoto, K. M. Kojima, M. I. Larkin, J. Merrin, B. Nachumi, Y. I. Uemura, Y. Maeno, Z. Q. Mao, Y. Mori, H. Nakamura, and M. Sigrist, Nature (London) **394**, 558 (1998).

[192] Y. Zhang, Z. R. Ye, Q. Q. Ge, F. Chen, J. Jiang, M. Xu, B. P. Xie, and D. L. Feng, Nature Physics **8**, 371 (2011).

[193] J. Nagamatsu, N. Nakagawa, T. Muranaka, Y. Zenitani, and J. Akimitsu, Nature (London) **410**, 63 (2001).

[194] B. T. Matthias, T. H. Geballe, K. Andres, E. Corenzwit, G. W. Hull, and J. P. Maita, Science **159**, 530 (1968).

[195] Y. B. Kuzma, *Crystal Chemistry of Borides* (Vysshaya Shkola, Lviv, 1983).

[196] A. P. Dudka, O. N. Khrykina, N. B. Bolotina, N. Y. Shitsevalova, V. B. Filipov, and N. E. Sluchanko, Journal of Alloys and Compounds **692**, 535 (2017).

[197] I. R. Shein and A. L. Ivanovskii, Physics of the Solid State **45**, 1429 (2003).

[198] B. Jäger, S. Paluch, O. J. Żogał, W. Wolf, P. Herzig, V. B. Filippov, N. Shitsevalova, and Y. Paderno, Journal of Physics: Condensed Matter **18**, 2525 (2006).

[199] J. Teyssier, A. Kuzmenko, D. van der Marel, F. Marsiglio, A. Liashchenko, N. Shitsevalova, and V. Filippov, Physical Review B **75**, 134503 (2007).

[200] H. Werheit, Y. Paderno, V. Filippov, V. Paderno, A. Pietraszko, M. Armbrüster, and U. Schwarz, Journal of Solid State Chemistry **179**, 2761 (2006).

[201] J. Teyssier, R. Lortz, A. Petrovic, D. van der Marel, V. Filippov, and N. Shitsevalova, Physical Review B **78**, 134504 (2008).

[202] R. Lortz, Y. Wang, S. Abe, C. Meingast, Y. B. Paderno, V. Filippov, and A. Junod, Physical Review B **72**, 024547 (2005).

[203] A. V. Rybina, K. S. Nemkovski, P. A. Alekseev, J.-M. Mignot, E. S. Clementyev, M. Johnson, L. Capogna, A. V. Dukhnenko, A. B. Lyashenko, and V. B. Filippov, Physical Review B **82**, 24302 (2010).

[204] N. Sluchanko, S. Gavrilkin, K. Mitsen, A. Kuznetsov, I. Sannikov, V. Glushkov, S. Demishev, A. Azarevich, A. Bogach, A. Lyashenko, A. Dukhnenko, V. Filipov, S. Gabani, K. Flachbart, J. Vanacken, G. Zhang, and V. Moshchalkov, Journal of Superconductivity and Novel Magnetism **26**, 1663 (2013).

[205] N. Sluchanko, A. Bogach, N. Bolotina, V. Glushkov, S. Demishev, A. Dudka, V. Krasnorussky, O. Khrykina, K. Krasikov, V. Mironov, V. B. Filipov, and N. Shitsevalova, Physical Review B **97**, 035150 (2018).

[206] K. Flachbart, S. Gabáni, K. Gloos, M. Meissner, M. Opel, Y. Paderno, V. Pavlík, P. Samuely, E. Schuberth, N. Shitsevalova, K. Siemensmeyer, and P. Szabó, Journal of Low Temperature Physics **1406** (2005).

[207] D. Daghero, R. S. Gonnelli, G. A. Ummarino, A. Calzolari, V. Dellarocca, V. A. Stepanov, V. B. Filippov, and Y. B. Paderno, Superconductor Science and Technology **17**, S250 (2004).

[208] M. I. Tsindlekht, G. I. Leviev, I. Asulin, A. Sharoni, O. Millo, I. Felner, Y. B. Paderno, V. B. Filippov, and M. A. Belogolovskii, Physical Review B **69**, 212508 (2004).

[209] V. A. Gasparov, N. S. Sidorov, and I. I. Zver'Kova, Physical Review B **73**, 094510 (2006).

[210] P. W. Anderson, Physical Review Letters **3**, 325 (1959).

[211] A. A. Abrikosov and L. P. Gorkov, Soviet Physics JETP **12**, 337 (1961).

[212] A. V. Balatsky, I. Vekhter, and J. X. Zhu, Reviews of Modern Physics **78**, 373 (2006).

[213] H. Alloul, J. Bobroff, M. Gabay, and P. J. Hirschfeld, Reviews of Modern Physics **81**, 45 (2009).

[214] N. E. Sluchanko, A. N. Azarevich, M. A. Anisimov, A. V. Bogach, S. Y. Gavrilkin, M. I. Gilmanov, V. V. Glushkov, S. V. Demishev, A. L. Khoroshilov, A. V. Dukhnenko, K. V. Mitsen, N. Y. Shitsevalova, V. B. Filippov, V. V. Voronov, and K. Flachbart, Physical Review B **93**, 085130 (2016).

[215] N. Sluchanko, A. Azarevich, A. Bogach, S. Gavrilkin, V. Glushkov, S. Demishev, K. Mitsen, N. Shitsevalova, V. Filippov, S. Gabani, and K. Flachbart, Acta Physica Polonica A **131**, 1036 (2017).

[216] N. Sluchanko, V. Glushkov, S. Demishev, A. Azarevich, M. Anisimov, A. Bogach, S. Gavrilkin, K. Mitsen, A. Kuznetsov, I. Sannikov, N. Shitsevalova, V. Filippov, M. Kondrin, and K. Flachbart, Physical Review B **96**, 144501 (2016).

[217] M. J. Graf, S. K. Yip, J. A. Sauls, and D. Rainer, Physical Review B **53**, 15147 (1995).

[218] R. Kubo and T. Toyabe, *Magnetic Resonance and Relaxation* (North Holland, 1967).

[219] D. M. Maric, P. F. Meier, S. Vogel, S. F. J. Cox, and E. A. Davis, Journal of Physics: Condensed Matter **3**, 9675 (1991).

[220] S. F. J. Cox, Zeitschrift fur Naturforschung A **47**, 371 (1992).

[221] R. E. Walstedt and L. R. Walker, Physical Review B **9**, 4857 (1974).

[222] G. M. Kalvius, D. R. Noakes, N. Marcano, R. Wäppling, F. Iga, and T. Takabatake, Physica B **326**, 398 (2003).